E-687

DECAY PROPERTIES OF THE CHARM BARYON Λ_c^+

A Dissertation

Submitted to the Graduate School

of the University of Notre Dame

in Partial Fulfillment of the Requirements

for the Degree of

Doctor of Philosophy

by

Eric James Mannel, A.B.

William D. Shephard

William D. Shephard, Director

Department of Physics

Notre Dame, Indiana

April, 1991

AAB1999

FERMILAB
LIBRARY

DECAY PROPERTIES OF THE

CHARM BARYON Λ_c^+

Abstract

by

Eric James Mannel, A.B.

Measurements of the relative branching ratios $BR(\Lambda_c^+ \rightarrow \Lambda\pi^+\pi^+\pi^-)/BR(\Lambda_c^+ \rightarrow pK^-\pi^+)$, $BR(\Lambda_c^+ \rightarrow p\overline{K^{*0}})/BR(\Lambda_c^+ \rightarrow pK^-\pi^+)$, and $BR(\Lambda_c^+ \rightarrow \Delta^{++}K^-)/BR(\Lambda_c^+ \rightarrow pK^-\pi^+)$ are described. Data for these measurements were obtained from the high energy photoproduction experiment E-687 which was performed at the Fermi National Accelerator Laboratory. Data from the 1987-1988 data run was analyzed. Samples of 57 ± 17 $\Lambda_c^+ \rightarrow \Lambda\pi^+\pi^+\pi^-$ and 142 ± 29 $\Lambda_c^+ \rightarrow pK^-\pi^+$ decays are observed. The decay channels $\Lambda_c^+ \rightarrow \Lambda\pi^+$ and $\Lambda_c^+ \rightarrow K^+K^-\pi^+$ were searched for; however, no statistically significant signals were observed in either decay channel. The relative branching ratio $BR(\Lambda_c^+ \rightarrow \Lambda\pi^+\pi^+\pi^-)/BR(\Lambda_c^+ \rightarrow pK^-\pi^+)$ was measured to be $0.55 \pm 0.16 \pm 0.15$. The $pK^-\pi^+$ sample was analyzed to determine contributions of the two 2-body resonance decays, $\Lambda_c^+ \rightarrow p\overline{K^{*0}}$ and $\Lambda_c^+ \rightarrow \Delta^{++}K^-$. The branching ratios relative to the $pK^-\pi^+$ final state were measured to be $0.20 \pm 0.12 \pm 0.10$ for the $p\overline{K^{*0}}$ mode, and $0.24 \pm 0.12 \pm 0.10$ for the $\Delta^{++}K^-$ mode. The ratio of particle to anti-particle was measured and determined to be consistent with unity for baryon energies greater than 60 GeV. These measurements are compared with other recent experimental results.

To my family,

Jim, Ruth, Michelle, and Stephanie

TABLE OF CONTENTS

LIST OF FIGURES v

LIST OF TABLES viii

ACKNOWLEDGEMENTS x

1 INTRODUCTION 1

1.1 The Standard Model 1

1.2 Charm Baryons and Weak Decays 4

1.3 Photoproduction 9

2 E-687 BEAM LINE AND SPECTROMETER 12

2.1 Wide Band Photon Beam Line 12

2.2 Spectrometer 16

2.2.1 Experimental Target 17

2.2.2 Beam Tagging 18

2.2.3 Charged Particle Tracking 20

2.2.4 Čerenkov 24

2.2.5 Calorimetry 25

2.2.6 Muon 28

2.2.7 Triggering 28

2.2.8 Data Acquisition 31

3 DATA RECONSTRUCTION AND REDUCTION 33

3.1 Track Reconstruction, Linking, and Momentum Determination 34

3.1.1 MICRORICO 34

3.1.2 TRACK 1 35

3.1.3 Linking and Momentum Determination 37

3.2 Vertexing 37

3.2.1 Global Vertexing 37

3.2.2 Candidate Driven Vertexing 38

3.3 Neutral Vee Finding 39

3.3.1 Microstrip Vees 39

3.3.2 M1 Vees 40

3.3.3 Reconstruction Vees 41

3.4 Kinks 43

3.5 Particle Identification 44

3.5.1 Čerenkov Identification 44
3.5.2 Muon Identification 45
3.5.3 Electromagnetic Calorimetry 46

3.6 Skimming 46
3.6.1 Λ Subskim 48
3.6.2 $\Lambda_c^+ \to pK^-\pi^+$ Subskim 49

4 DATA ANALYSIS 50

4.1 Analysis of the $pK^-\pi^+$ Sample 50
4.1.1 $pK^-\pi^+$ Analysis Cuts 50
4.1.2 Misidentification Studies 56

4.2 Analysis of Samples for Decay Modes Including a Λ 61
4.2.1 $\Lambda_c^+ \to \Lambda\pi^+\pi^+\pi^-$ Analysis 62
4.2.2 $\Lambda_c^+ \to \Lambda\pi^+$ Search 65
4.2.3 $\Lambda_c^+ \to \Lambda K^+K^-\pi^+$ Search 65

4.3 Efficiency Measurements 68
4.3.1 Monte Carlo Efficiency Determination 68
4.3.2 Corrections to the Monte Carlo Efficiencies 70
4.3.3 Λ Strip Efficiency 78

4.4 $\Lambda_c^+ \to \Lambda\pi^+\pi^+\pi^-$ to $\Lambda_c^+ \to pK^-\pi^+$ Branching Ratio Measurement 82

4.5 $\Lambda_c^+ \to p\overline{K^{*0}}$ to $\Lambda_c^+ \to pK^-\pi^+$ Branching Ratio Measurement 86

4.6 $\Lambda_c^+ \to \Delta^{++}K^-$ to $\Lambda_c^+ \to pK^-\pi^+$ Branching Ratio Measurement 88

4.7 Particle, Anti-Particle Asymmetry Studies 91

5 CONCLUSIONS 96

5.1 Branching Ratio Summary 96
5.1.1 Comparison with Other Experimental Results 97
5.1.2 Comparison with Theory 97

5.2 Other Results 98

5.3 Prospects for the Future 98

A MONTE CARLO 99

A.1 GENERIC 99

A.2 ROGUE 100

BIBLIOGRAPHY 103

LIST OF FIGURES

1.1 Baryon family predicted by the Standard Model 5
1.2 The Feynman diagrams for the weak decay of charm hadrons 7
1.3 Feynman diagram for Bethe-Heitler pair production 10
1.4 Feynman diagram for photon-gluon fusion 10
1.5 Theoretical prediction for the photon-gluon cross section with recent experimental results 11

2.1 Schematic of the Fermilab National Accelerator Laboratory 13
2.2 The Wide Band photon beam line 15
2.3 The Wide Band photon beam spectrum 16
2.4 The Beryllium targets 17
2.5 The RESH shower counter 19
2.6 The experimental target region 20
2.7 The E-687 spectrometer 22
2.8 The hadron calorimeter pad arrangement 27
2.9 H×V hodoscope and logic 30
2.10 Schematic of the E-687 DAQ 32

3.1 Invariant mass distributions for microstrip vee K^0_s and Λ candidates 41
3.2 Invariant mass distributions for M1 vee K^0_s and Λ candidates 42
3.3 Invariant mass distributions for reconstruction vee K^0_s and Λ candidates . . 43

4.1 Angular decay distributions of $pK^-\pi^+$ candidate tracks for Monte Carlo and data 52
4.2 Primary and secondary vertex distributions for $pK^-\pi^+$ candidates with $L/\sigma_L \geq 1.0$ 53
4.3 Primary and secondary vertex error distributions for $pK^-\pi^+$ candidates with $L/\sigma_L \geq 1.0$ 54

4.4 Vertex separation quantities for $pK^-\pi^+$ candidates with $L/\sigma_L \geq 1.0$ 55
4.5 $pK^-\pi^+$ mass distributions for several values of the L/σ_L cut 55
4.6 Proton misidentification mass distributions for $pK^-\pi^+$ candidates 57
4.7 Proton misidentification mass distributions for $pK^-\pi^+$ candidates in the mass range $2.260\ GeV/c^2 \leq M(pK^-\pi^+) \leq 2.310\ GeV/c^2$ 57
4.8 Mass distributions for the reflection of Monte Carlo $pK^-\pi^+$ events into the K^+K^- and $K^+K^-\pi^+$ mass distributions 58
4.9 Mass distributions for the reflection of Monte Carlo D^+ and D_s^+ events into the $pK^-\pi^+$ mass distribution 59
4.10 $pK^-\pi^+$ mass distributions for $L/\sigma_L \geq 3.0$ after misidentification mass cuts 60
4.11 Vertex separation quantities for $\Lambda\pi^+\pi^+\pi^-$ candidates 63
4.12 $\Lambda\pi^+\pi^+\pi^-$ mass distributions for several values of the L/σ_L cut 63
4.13 $\Lambda\pi^+\pi^+\pi^-$ mass distributions for candidates with $E(\Lambda_c^+) \geq 60\ GeV$ for several values of the L/σ_L cut 64
4.14 $\Lambda\pi$ mass distributions 66
4.15 $\Lambda\pi$ mass distributions for several values of the L/σ_L cut 66
4.16 $\Lambda\pi$ mass distributions for several values of the L/σ_L cut 67
4.17 $\Lambda KK\pi$ mass distributions 68
4.18 Efficiencies for successive cuts used in the $pK^-\pi^+$ analysis 71
4.19 Efficiencies for successive cuts used in the $\Lambda\pi^+\pi^+\pi^-$ analysis 72
4.20 Monte Carlo efficiency distributions for final $\Lambda\pi^+\pi^+\pi^-$ and $pK^-\pi^+$ analysis cuts 73
4.21 Λ distributions from data and Monte Carlo used to determine the proton Čerenkov efficiency 77
4.22 Λ distributions from data and Monte Carlo used to determine the Λ strip efficiency 79
4.23 Linking efficiency corrections for 3-chamber and 5-chamber tracks as a function of momentum 81
4.24 $\Lambda\pi^+\pi^+\pi^-$ and $pK^-\pi^+$ mass distributions used for branching ratio measurement 84
4.25 Efficiency corrected $\Lambda\pi^+\pi^+\pi^-$ and $pK^-\pi^+$ mass distributions used for the branching ratio measurements 85
4.26 $pK^-\pi^+$ sample used for the $p\overline{K^{*0}}$ branching ratio measurement 87
4.27 $\overline{K^{*0}}$ signals used for the $p\overline{K^{*0}}$ branching ratio measurement 89

4.28 $pK^-\pi^+$ sample used for the $\Delta^{++}K^-$ branching ratio measurement 90
4.29 $p\pi^+$ mass distributions used for the $\Delta^{++}K^-$ branching ratio measurement . 92
4.30 $p\pi^+$ mass distribution for Monte Carlo $\Lambda_c^+ \to pK^-\pi^+$ nonresonant, $\Lambda_c^+ \to p\overline{K^{*0}}$, and $\Lambda_c^+ \to \Delta^{++}K^-$ 93
4.31 $p\pi^+$ mass distributions for Monte Carlo $\Lambda_c^+ \to pK^-\pi^+$ nonresonant, $p\overline{K^{*0}}$, and $\Lambda_c^+ \to pK^-\pi^+$ nonresonant, $p\overline{K^{*0}}$, and $\Delta^{++}K^-$ 93
4.32 $\Lambda\pi^+\pi^+\pi^-$ and $pK^-\pi^+$ mass distributions shown separately for particles and anti-particles 95

LIST OF TABLES

1.1 QUARK AND LEPTON FAMILIES 2

2.1 SILICON MICROSTRIP DETECTOR PARAMETERS 21
2.2 ČERENKOV THRESHOLDS 24

3.1 KINK DECAY TOPOLOGIES 44
3.2 ČERENKOV PARTICLE IDENTIFICATION CODES 46
3.3 AVERAGE MUON EFFICIENCY FOR INNER MUON COUNTER 47

4.1 MEAN VERTEX ERRORS FOR PRIMARY AND SECONDARY VERTICES FOR $pK^-\pi^+$ CANDIDATES 56
4.2 FIT RESULTS FOR $pK^-\pi^+$ MASS DISTRIBUTIONS FOR DIFFERENT VALUES OF THE L/σ_L CUT 56
4.3 $pK^-\pi^+$ FIT RESULTS FOR DIFFERENT KAON MISIDENTIFICATION CUTS ($L/\sigma_L \geq 3.0$) 59
4.4 FIT RESULTS FOR $\Lambda\pi^+\pi^+\pi^-$ CANDIDATES WITH A Λ_c^+ ENERGY $\geq$ 60 GeV 65
4.5 EFFICIENCY DISTRIBUTION FIT RESULTS FOR FINAL $pK^-\pi^+$ AND $\Lambda\pi^+\pi^+\pi^-$ ANALYSIS CUTS 74
4.6 PION ČERENKOV IDENTIFICATION EFFICIENCIES FOR DATA AND MONTE CARLO 75
4.7 Λ YIELDS BY TRACK TYPE AND ČERENKOV IDENTIFICATION OF PROTON TRACK 76
4.8 PROTON ČERENKOV EFFICIENCIES FOR MONTE CARLO AND DATA 76
4.9 KAON ČERENKOV EFFICIENCIES FOR MONTE CARLO AND DATA 78
4.10 LAMBDA STRIP YIELDS FOR SSDVEE'S AND M1VEE'S 80
4.11 LAMBDA STRIP EFFICIENCIES FOR SSDVEE'S AND M1VEE'S 80
4.12 COEFFICIENTS FOR LINKING EFFICIENCY CORRECTIONS 81

4.13 FIT RESULTS OF Λ_c^+ MASS DISTRIBUTIONS USED FOR BRANCHING RATIO MEASUREMENT 83
4.14 FIT RESULTS OF EFFICIENCY CORRECTED Λ_c^+ MASS DISTRIBUTIONS USED FOR BRANCHING RATIO MEASUREMENT 83
4.15 $\Lambda\pi^+\pi^+\pi^-$ TO $pK^-\pi^+$ BRANCHING RATIOS FOR THE DIFFERENT $pK^-\pi^+$ ANALYSIS CUTS 86
4.16 FIT RESULTS FOR $p\overline{K^{*0}}$ BRANCHING RATIO ANALYSIS 87
4.17 FIT RESULTS FOR $\Delta^{++}K^-$ BRANCHING RATIO ANALYSIS 90
4.18 FIT RESULTS FOR PARTICLE AND ANTI-PARTICLE MASS DISTRIBUTIONS 94

5.1 MEASUREMENTS OF Λ_c^+ BRANCHING FRACTIONS RELATIVE TO THE $pK^-\pi^+$ DECAY MODE 97

ACKNOWLEDGEMENTS

Experimental high energy physics is a collaborative effort and this work is no different. Without the assistance of a large number of people, the work presented here would never have come to fruition.

I wish to thank my advisor Bill Shephard for all of his assistance and support during my tenure here at Notre Dame. His belief in my abilities helped my through those bad times.

I wish to thank all the members of the Notre Dame High Energy group for their assistance through the years. A special thanks to Randy Ruchti and Neal Cason for their insight and guidance. I also wish to thank Jim Bishop for tolerating all my complaints about the computer. Late night discussions are always useful in sorting problems in analysis, thanks to fellow graduate students Robert Garner and John Cunningham for all the help. I also wish to thank fellow graduate student and former roommate Ray Mountain for his friendship and help over the years.

The success of the E-687 experiment is due in part to the quality of the members of the collaboration. It has been a real pleasure to learn and work with such a talented group of people. I wish to especially thank the spokesman, Joel Butler, who continuously terrorized us with those 4:00 am phone calls while we were taking data. I wish to thank the man from Down Under, Peter Kasper, for his efforts in code management and adding spice to the conversation at the Users Center. John Cumalat and Jim Wiss were instrumental in the analysis of the data and for that I am grateful. Among the fine group of graduate students working on the experiment, I wish to thank Steve Culy, Karen Lingel, and Rik Yoshida for their continuous attention to the details. I also wish to thank the members of Lab 6 at Fermilab for their fine work in building the chamber system. I will always remember the first time I touched a wire plane and removed 13 wires. Finally I wish to thank Forest Davenport for his expertise and friendship.

The events of October 3, 1987 marked one of the low points in my career in high energy physics. If it were not for the outstanding efforts of the Fermilab staff we would never have risen out of the ashes.

Friendships are just as important to the completion of this work. I wish to thank Gregg and Kathi Sturrus, Jeff and Stephanie Warmke, Jay and Mary Beth Rose, Fred Hampel, Zeid Ayer, Matt Weidmann, Wanda Newby, Steve Schwartzbek, and Clyde Dawson for all their support over the years. South Bend would not have been the same without the Pit Bulls. I will always remember the hard fought games and the cold beers after.

A special thanks to very close and special friend, Tricia Nymberg, who has reminded me that there is more to life then just physics.

My first memories of experimental science come from 7th grade. I wish to thank my father who was also my teacher for that introduction. I also want to thank Ben Austin, my high school physics teacher, who made science so much fun.

Finally I wish to thank my family. It has been your love and support over the years that has made this possible.

I thank you and wish you the best in all of your efforts in the years to come.

CHAPTER 1

INTRODUCTION

Elementary particle or high energy physics is the study of the very small. As the energy of a particle is increased, its compton wavelength decreases allowing the physicist to probe smaller and smaller dimensions. As wavelengths approaching 1 Ångstrom (10^{-10} m) are reached, matter is seen as being comprised of atoms. At wavelengths of order 1 fermi (10^{-15} m), the atom is seen to be comprised of a nucleus, and a surrounding electron cloud. As wavelengths decrease further, the nucleus is resolved into nucleons which are in turn found to be composed of quarks. Currently electrons, which are one member of the lepton family, and quarks show no evidence any substructure and are viewed as truly elementary particles. The goal of high energy physics is to study these elementary particles and the forces that govern their interactions.

1.1 The Standard Model

The Standard Model has evolved over the past 60 years to its current form with 12 fundamental point-like particles and 4 forces which allow the particles to interact. The fundamental particles can be divided into two families which are further subdivided into three doublets; the quark family consisting of 6 members with fractional charge,

$$\begin{pmatrix} u \\ d \end{pmatrix} \begin{pmatrix} c \\ s \end{pmatrix} \begin{pmatrix} t \\ b \end{pmatrix}$$

and the lepton family consisting of 3 charged members and 3 neutral members,

$$\begin{pmatrix} e \\ \nu_e \end{pmatrix} \begin{pmatrix} \mu \\ \nu_\mu \end{pmatrix} \begin{pmatrix} \tau \\ \nu_\tau \end{pmatrix}.$$

The properties of each of these particles are shown in Table 1.1. Of the 6 quarks, only the top quark has not been experimentally observed, although a large body of indirect evidence

is supportive of its existence.

TABLE 1.1
QUARK AND LEPTON FAMILIES

Quarks	Mass (MeV/c^2)	Spin	Charge
up (u)	$\simeq 350.$	1/2	$+2/3e$
down (d)	$\simeq 350.$	1/2	$-1/3e$
charm (c)	$\simeq 1500.$	1/2	$+2/3e$
strange (s)	$\simeq 550.$	1/2	$-1/3e$
top (t)	$\simeq 140000.$	1/2	$+2/3e$
bottom (b)	$\simeq 4500.$	1/2	$-1/3e$
Leptons			
electron (e)	$\simeq 0.511$	1/2	$-1e$
ν_e	$\simeq 0.$	1/2	$0e$
muon (μ)	$\simeq 105.6$	1/2	$-1e$
ν_μ	$\simeq 0.$	1/2	$0e$
tau (τ)	$\simeq 1870.$	1/2	$-1e$
ν_τ	$\simeq 0.$	1/2	$0e$

The concept of quarks as the constituents of hadrons was first proposed by Gell-Mann [1] in 1964 to explain the hadron structure in terms of fundamental particles. Three quarks—up, down, and strange—each with fractional charge composed the initial model. The up and down quarks were grouped together as an isospin doublet, while the strange quark was a singlet. Using these three quarks it was possible to construct the known hadrons as combinations of quarks and/or antiquarks; mesons as bound states of a quark-antiquark pair, and baryons (antibaryons) as bound states of three quarks (three antiquarks). Quark-antiquark pairs are produced through the strong interaction, naturally accounting for the conservation of baryon number while imposing no restrictions on the number of mesons produced. The earliest known hadrons—neutrons, protons, and pions—could be constructed using just the up and down quarks. In the 1950's a new quantum number, strangeness, was introduced to account for the copious pair production of "strange" particles such as the K mesons, and the Λ^0 and Σ baryons which had a relatively long lifetime in context of the strong interaction. This quantum number was attributed to the strange quark which is conserved in both strong and electromagnetic interactions, and decays via the weak interaction. A series of

electron scattering experiments at SLAC in the 1960's provided experimental evidence for substructure within hadrons. These constituents have since been identified as quarks and gluons.

An initial problem with the quark model was the existence of the Δ^{++} baryon resonance. The +2 charge implies that it is composed of 3 identical up quarks. The spin of the Δ^{++} is measured to be $J = 3/2$, consistent with a combination of three spin 1/2 up quarks in a completely symmetric ground state. The Δ^{++} ground state is then completely symmetric which is forbidden by fermi statistics for fermions. In order to resolve this problem a new quantum number was assigned to quarks, color. Each quark has one of three possible colors, and each antiquark, anticolor. Hadrons are built from quarks such that they form color singlet states, i.e., they have zero net color. In this way the quarks comprising the Δ^{++} are unique and fermi statistics are not violated. Color is now interpreted to be the "charge" of the strong interaction [2].

In order to explain the absence of flavor-changing neutral currents, Glashow, Iliopoulos, and Maiani [3] introduced a fourth quark, charm, in 1970. The charm quark was added with the strange quark to form a second quark doublet. Experimental evidence for this new quark came in November of 1974 from two groups, one working at the SLAC e^+e^- collider SPEAR [4] and the second one at the Brookhaven AGS using a 28 GeV proton beam on a beryllium target [5]. Narrow resonances in the e^+e^- and $\mu^+\mu^-$ mass spectra at 3.1 GeV/c^2 were interpreted as the lowest lying $c\bar{c}$ state. Subsequent experimental work discovered excited $c\bar{c}$ states and states containing open charm.

In 1977, a similar narrow resonance was discovered in the mass range 9.5 - 10.5 GeV/c^2 in 400 GeV proton-nucleus collisions at FNAL [6, 7]. This resonance was attributed to a bound state of the heavy bottom quark. In order to accommodate this new heavy quark, the quark model was extend to include a third doublet consisting of the new bottom quark, and a yet to be discovered top quark.

Quarks and leptons interact with each other as a result of 4 fundamental forces. Listed in order of decreasing strength they are the strong force, the electromagnetic force, the weak force, and gravity. Gravity, being the weakest of the forces, is not currently included in the Standard Model. The remaining three forces are described in the Standard Model by gauge theories. Gauge theories are a special class of field theories that are invariant under local

phase transformations. A consequence of invariance under a local phase transformation is the conservation of physical quantities. This can be demonstrated by considering quantum electrodynamics (QED) which describes the electromagnetic interaction. The invariance of the electromagnetic field under a local phase transformation in QED leads to the conservation of charge [8]. A second important property of these field theories is that they are renormalizable. It is currently believed that for any theory to describe the fundamental forces successfully, it must be both renormalizable and gauge invariant.

The electromagnetic and weak forces are united in the Standard Model using the gauge theory known as the Weinberg-Salam [9] theory of electro-weak interactions. This model is represented by the group notation $SU(2) \times U(1)$. The charged and neutral weak interactions are described by the symmetry group $SU(2)$ which describes the gauge transformation of the field triplet W^i_μ. The symmetry group $U(1)$ describes the field transformation of the field singlet B_μ. As a result of spontaneous symmetry breaking the field triplet acquires mass, and its members appear as the massive vector bosons $W^\pm$ and Z^0, while the fourth boson remains massless and appears as the the photon. The massive vector bosons were discovered experimentally at the CERN e^+e^- collider in 1983 [10, 11].

The strong interaction between quarks is described by the gauge theory Quantum Chromodynamics (QCD) which is described in terms of the symmetry group $SU(3)$. The conserved charge of QCD is the three-color charge field, commonly labeled red(r), blue(b), and green(g), and the corresponding anti-charges. The propagators of the the strong interaction are the 8 massless, electrically neutral gauge bosons, the gluons. Since the gluon carries color, it can couple to other gluons, unlike the photon which can couple only to electrically charged particles. Leptons are colorless particles so they do not participate in strong interactions.

1.2 Charm Baryons and Weak Decays

The ground-state baryons that are predicted to exist within the Standard Model are shown in Fig. 1.1. These baryons are constructed from the 4 lightest quarks—up, down, charm, and strange—requiring that the total space, spin, and flavor wave function be completely symmetric. Charm baryons can decay via the weak interaction, the strong interaction, or

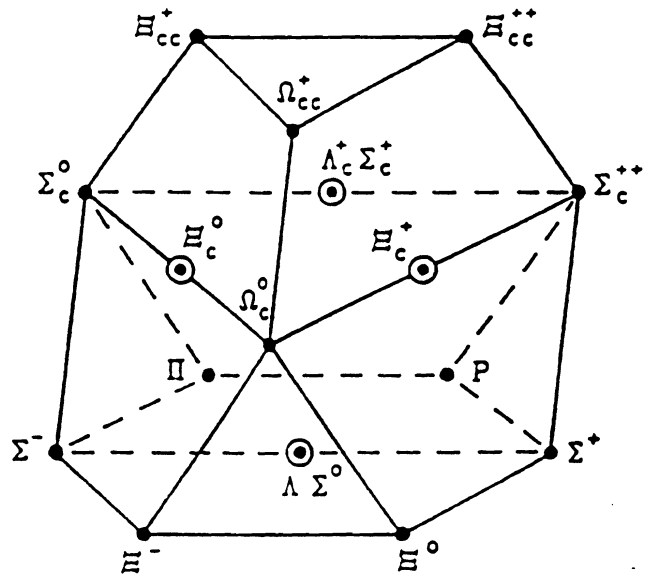

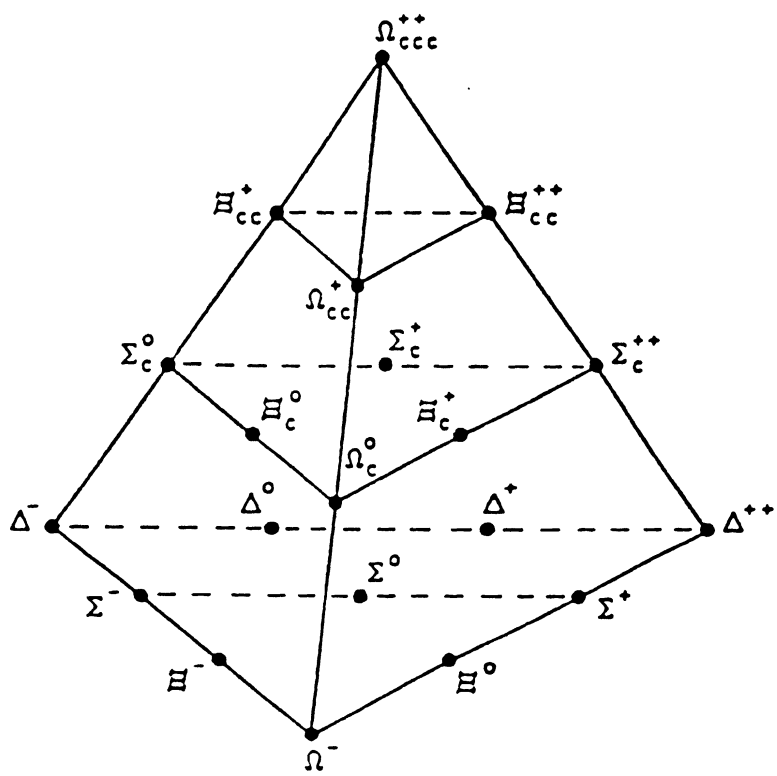

Figure 1.1: Baryon family predicted by the Standard Model: a) $J = 1/2^+$ octet, b) $J = 3/2^+$ decuplet.

the electromagnetic interaction. Since the charm quantum number is conserved in both the strong and electromagnetic interactions, charm baryons can only decay through these interactions provided that they are heavier than the lowest lying charm hadrons. The charm baryons Λ_c^+ and Ξ_c decay only via the flavor changing weak decay to noncharm final states. Both of these particles have lifetimes on the order of 2×10^{-13} seconds which is typical for weak decays. The Σ_c's are sufficiently massive, $M(\Sigma_c) \approx 2455\ MeV/c^2$, with respect to the Λ_c^+, $M(\Lambda_c^+) \approx 2285\ MeV/c^2$, that they decay predominately via the strong interaction to $\Lambda_c^+\pi$ with a lifetime typical of strong decays.

The theory of weak decays is based on a theoretical model proposed by Cabibbo [12] in 1963. Cabibbo proposed the existence of a weak quark eigenstate that is rotated with respect to the strong or mass quark eigenstate. This rotation or mixing is characterized by the Cabibbo angle, $\sin\theta_c \approx 0.23$. The model was later expanded to include the addition of the charm quark [3]. In the Cabibbo model of weak decays, the weak eigenstates are related to the mass eigenstates via the following relationship:

$$\begin{pmatrix} d' \\ s' \end{pmatrix} = \begin{pmatrix} \cos\theta_c & \sin\theta_c \\ -\sin\theta_c & \cos\theta_c \end{pmatrix} \begin{pmatrix} d \\ s \end{pmatrix}$$

In this scheme $u \rightarrow d$ and $c \rightarrow s$ decays are "Cabibbo favored" by a factor $\cos\theta_c$, while $u \rightarrow s$ and $c \rightarrow d$ decays are "Cabibbo suppressed" by a factor of $\sin\theta_c$.

In 1973 Kobayashi and Maskawa [13] expanded the model to include 6 quarks. While a complete discussion of the Kobayashi-Maskawa mixing scheme will not be presented here, it should be noted that the expanded mixing matrix allows for the presence of 3 mixing angles and a single phase factor. It is the presence of this phase factor that gives rise to CP violation in the Standard Model.

The lowest order processes for weak decays of charm hadrons are W-emission (the spectator model), W-exchange, and W-annihilation. The Feynman diagram for each of these processes is shown in Fig. 1.2. The W-emission diagram is similar to the weak decay of the muon, so the charm lifetime can be estimated from the muon lifetime by correcting for the difference in the masses:

$$\tau(c) = \tau(\mu) \times Br(c \rightarrow qe\nu) \times \left(\frac{m_\mu}{m_c}\right)^5 .$$

This predicts a lifetime for charm hadrons on the order of 10^{-12} seconds.

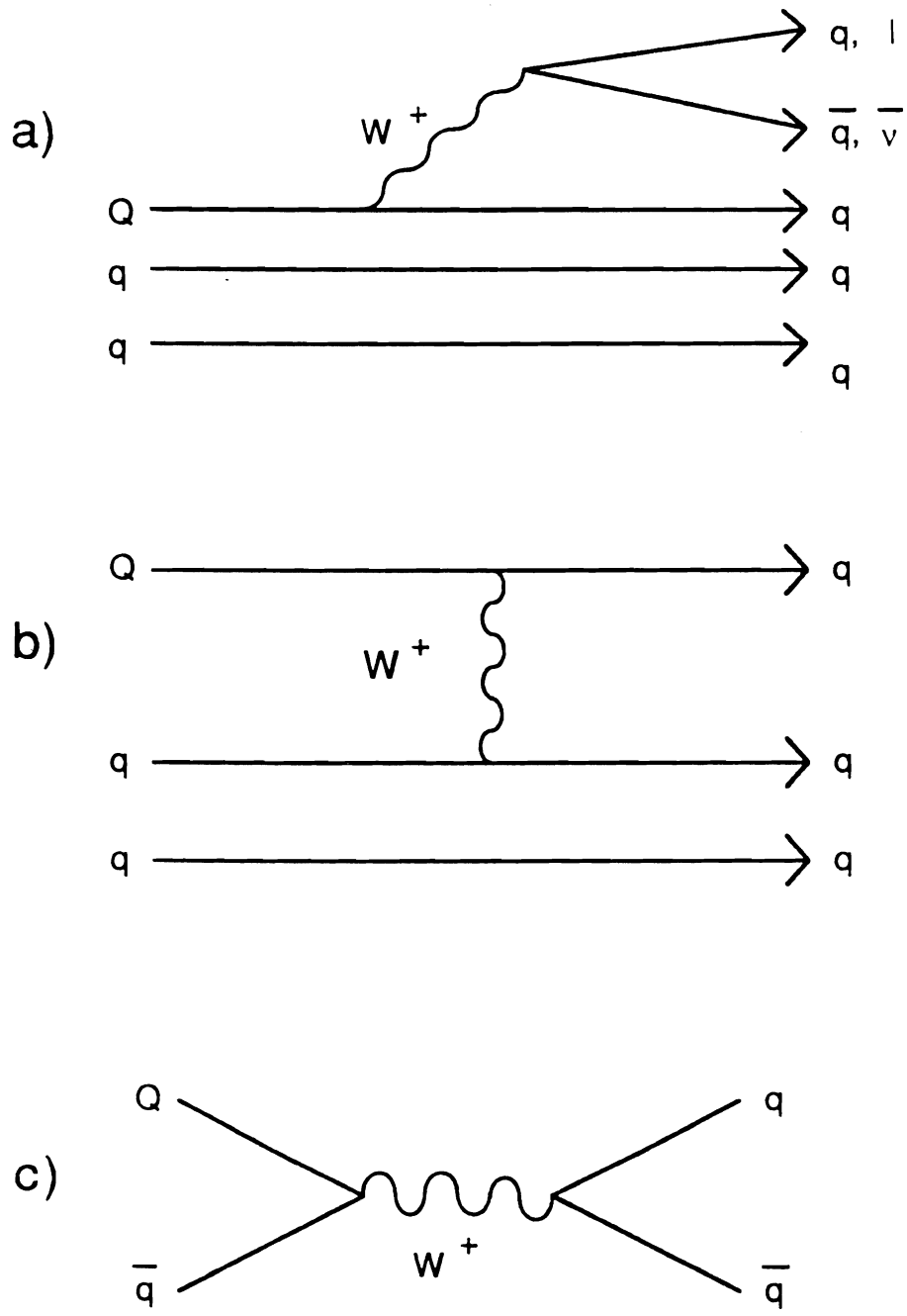

Figure 1.2: The Feynman diagrams for the weak decay of charm hadrons: a) W-emission, b) W-exchange, c) W-annihilation.

A significant aspect of the W-emission model is the prediction of approximately equal lifetimes for all charm hadrons. Experimental measurements however indicate that there are considerable differences in the charm hadron lifetimes, with the ratio of charm hadrons being:

$$\tau(D^+) : \tau(D^0) : \tau(D_s^+) : \tau(\Lambda_c^+) \approx 5 : 2 : 2 : 1$$

The difference in lifetimes for the different charm hadrons can be accounted for in part by including the additional weak decay diagrams shown in Fig. 1.2 and considering QCD effects. For Cabibbo favored decays, the W-annihilation diagram exists only for the D_s^+. The W-exchange diagram is possible for both the D^0, and Λ_c^+. For the decay of the spin 0 D^0, the W-exchange diagram is helicity suppressed in a manner similar to $\pi \rightarrow l\nu$ decay. This helicity suppression however, does not apply in the spin 1/2 Λ_c^+ decay. The longer D^+ lifetime may also be explained partially by interference effects [14]. The two $\bar{d}$ quarks in the D^+ decay are excluded from occupying the same region of phase space, leading to an increase of the D^+ lifetime. The relative contribution of each of these processes to the decay of charm hadrons is still unclear. Continued studies of the lifetimes and branching ratios for charm hadrons may shed new insight into the process of charm decay.

Early attempts were made to calculate the lifetimes of the charm hadrons using both the nonrelativistic quark model and MIT Bag Model [15, 16, 17, 18, 19, 20] with a variety of assumptions. The different models predicted Λ_c^+ lifetimes in the range 0.1 to 2 ps. The models also predicted a hierarchy for the charm baryon lifetimes with the Λ_c^+ and Ξ_c^- being the longest lived, and the Ξ_c^0 and Ω_c^+ having shorter lifetimes. Using the Non-Relativistic Quark Model, both Rückl [15], and Barger [16] concluded that W-exchange was the dominate process for the non-leptonic decay modes, and that W-emission and interference effects played only a small role in the Λ_c^+ decays.

MIT Bag Model calculations on the other hand required contributions in addition to the W-exchange process to account for the short lifetime of the Λ_c^+. Significant contributions from W-emission, or from enhancement of W-exchange due to soft gluon exchange were postulated to account for the short Λ_c^+ lifetime.

These early theoretical attempts were based on early measurements of charm lifetimes which indicated large differences for the different charm hadrons. Improved measurements of the lifetimes have since been made which show a smaller difference between the different

charm hadrons; however, no new theoretical predictions have been made based on these new measurements.

1.3 Photoproduction

At high energies the dominate process for photon interactions is the QED process of Bethe-Heitler pair production. The Feynman diagram is shown in Fig. 1.3. Since this is a QED process it is possible to calculate the cross section using standard perturbation theory. The leading model for the photoproduction of hadronic states is the QCD process of photon-gluon fusion (PGF) [21]. In this model the photon couples to the quark-antiquark pair, and then one of the quarks is scattered by a gluon from the target nucleon. The Feynman diagram for PGF is shown in Fig. 1.4. In order to conserve color, soft gluons (not shown) are radiated from the final states. The cross section for producing a charm-anticharm pair can be calculated by taking the cross section for the Bethe-Heitler process, substituting a factor of α_s for α_{em} at the quark-gluon vertex, and correcting for the quark charge and color factors:

$$\begin{aligned}\sigma(s') &= 4\pi\frac{16}{9}\frac{\alpha_s\alpha_{em}}{s'}\left\{\left(1+4\frac{m_c^2}{s'}-8\frac{m_c^4}{s'^2}\right)\right.\\ &\times\ln\left[\frac{s'}{m_c^2}\frac{1}{2}\left(1+\left(1-4\frac{m_c^2}{s'}\right)^{1/2}-2\frac{m_c^2}{s'}\right)\right]\\ &\left.-\left(1-4\frac{m_c^2}{s'}\right)^{1/2}\left(1+4\frac{m_c^2}{s'}\right)\right\}.\end{aligned}$$

where s' is the photon-gluon center of mass energy. In order to get the total cross section for heavy quark production, the elementary cross section needs to be integrated over the gluon momentum distribution, $G(x)$, for the target nucleon [22]. The total open charm photoproduction cross section is then given by

$$\sigma_{\gamma N\to c\bar{c}}(s) = \int_{4M_c^2}^{s} G(\frac{s'}{s})\sigma(s')\frac{ds'}{s}$$

where s is the center of mass energy for the photon-nucleon system.

Cross section values have recently been calculated using the photon-gluon fusion model of charm and beauty [23] including next-to-leading order QCD terms proportional to $\alpha_s^2\alpha_{em}$.

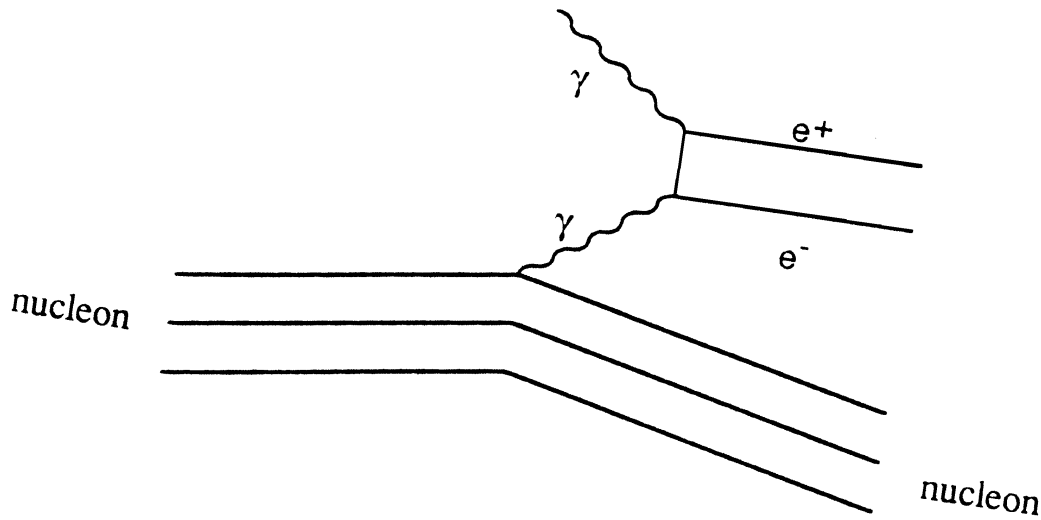

Figure 1.3: Feynman diagram for Bethe-Heitler pair production.

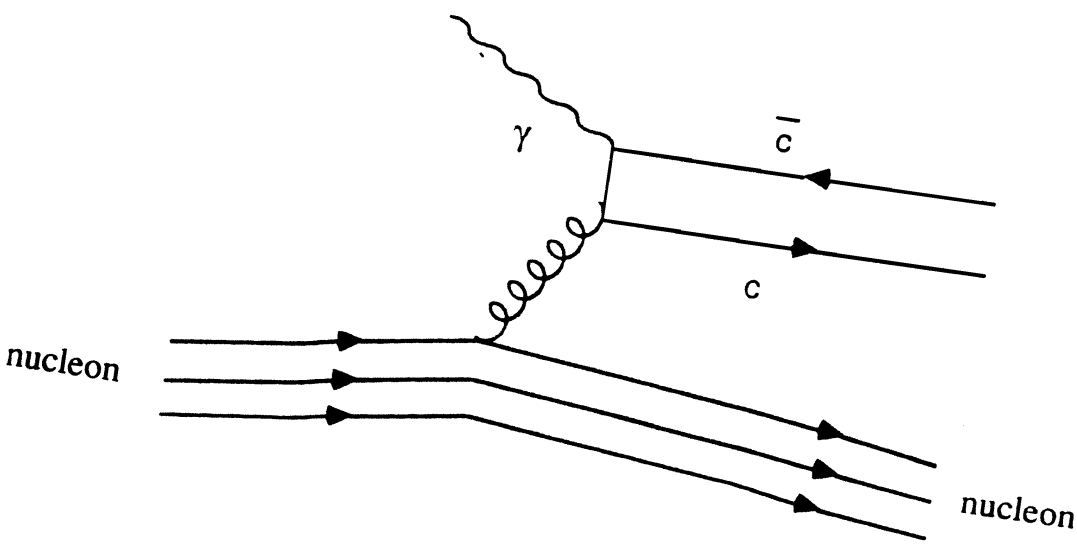

Figure 1.4: Feynman diagram for photon-gluon fusion.

The results for these calculations are shown in Fig. 1.5 along with results of experimental measurements for the photoproduction cross section. These calculations and the experimental measurements show a slowly rising cross-section as a function of energy.

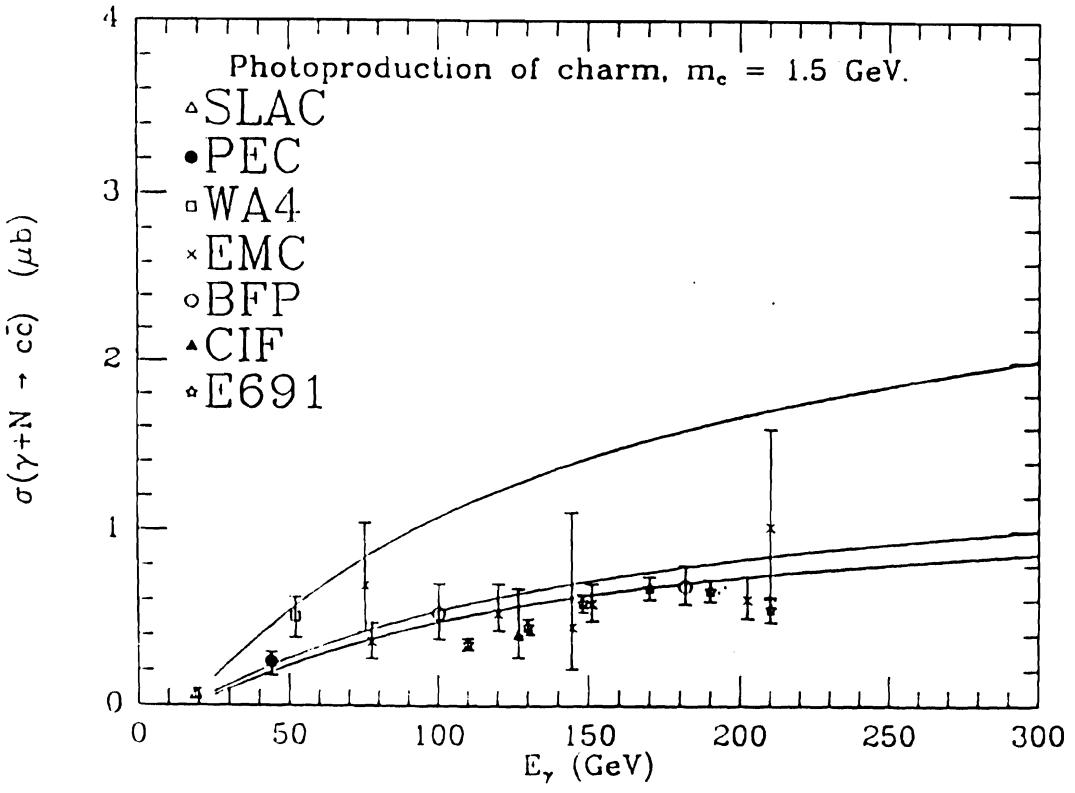

Figure 1.5: Theoretical prediction for the photon-gluon cross section with recent experimental results [23].

CHAPTER 2

E-687 BEAM LINE AND SPECTROMETER

Experiment E-687 was performed in the Wide Band Laboratory located in the Proton East beam line at Fermi National Accelerator Laboratory. The data used for this analysis were taken during the 1987-1988 fixed target run. Starting in June 1987, the run consisted of a detector checkout and calibration period, followed by a period of 250 GeV/c electron beam running. On October 3, 1987 a fire déstroyed or severely damaged several components of the E-687 spectrometer. On December 1, 1987 following two months of rebuilding and recalibrating the components of the spectrometer, data taking was resumed using a 350 GeV/c electron beam. A total of 60 million triggers was recorded on tape by February 15, 1988 when the 1987-1988 Fermilab Fixed Target program was terminated. Data reported in this dissertation came from the 350 GeV/c electron beam running period.

2.1 Wide Band Photon Beam Line

The experimental photon beam was derived from an 800 GeV/c proton beam. The Fermilab accelerator layout is shown in Fig. 2.1. The proton acceleration cycle begins with ionized hydrogen being accelerated to 750 keV/c by a Cockcroft-Walton accelerator. Next the proton beam is injected into a linear accelerator, the Linac, and accelerated to $\geq 1GeV/c$. The proton beam then enters the Booster ring, a small proton synchrotron accelerator which accelerates the beam to 8 GeV/c. Following the Booster is the Main Ring, a 1 kilometer radius proton synchrotron accelerator made of conventional iron electro-magnets. The beam is accelerated to to 150 GeV/c before being injected into the Tevatron. Physically located directly beneath the Main Ring, the Tevatron is a 1 kilometer radius ring of superconducting magnets where the proton beam is accelerated to a final energy of 800 GeV/c for fixed

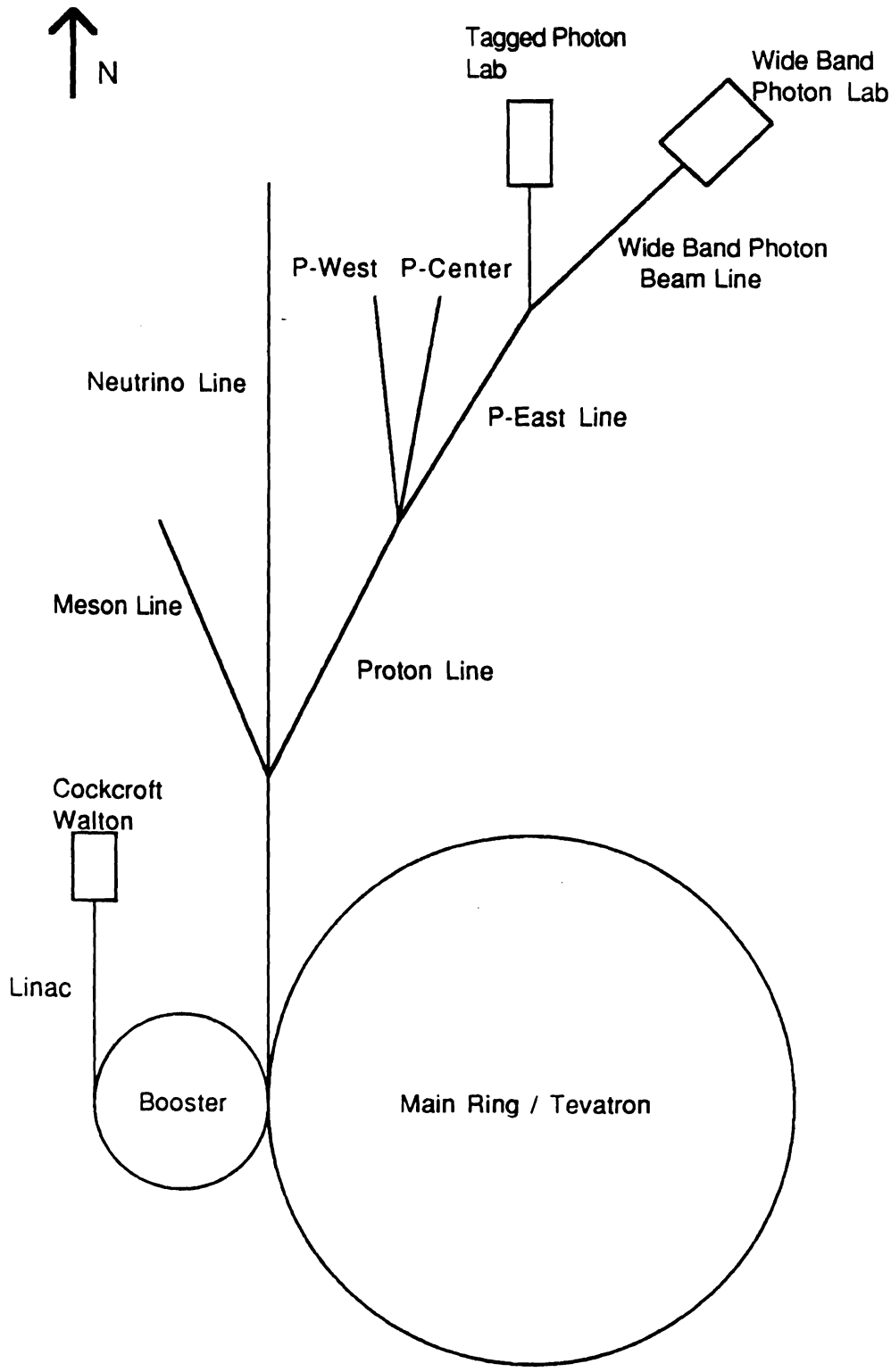

Figure 2.1: Schematic of the Fermilab National Accelerator Laboratory.

target running. The acceleration process required approximately 40 seconds and accelerated approximately 3×10^{13} protons per cycle during the 1987-1988 run.

After reaching a final energy of 800 GeV/c, the beam is extracted from the Tevatron for distribution to various experimental beam lines over a 20 second spill structure. Initially the beam is electrostatically split into three beams for each of the Fixed Target areas, Muon, Neutrino, and Proton. Following this split, the Proton Area beam is split by a septum into three beams for the P-West, P-Center, and P-East experimental areas. The P-East line provides proton beam for both the Tagged Photon Lab, and the Wide Band Photon Lab. Following the 3-way proton split, the P-East beam is split into 2 beams via a Lambertson magnet. One of the proton beams is then transported to the production target for the Wide Band Photon Beam.

The schematic layout of the Wide Band Photon Beam from the production target to the experimental target is shown in Fig. 2.2. The proton beam strikes an 18 in. long Beryllium target. The protons interacting in the target produce both charged and neutral particles. Following the target a series of dipole magnets sweep the charged particles into a dump leaving a neutral beam consisting of π^0, n, and K_L^0's, with the π^0's decaying immediately into two photons. Downstream of the sweeper magnets the neutrals impinge upon a lead converter of 0.5 radiation lengths converting photons into e^+e^- pairs. The electrons from this conversion process are then captured by a traditional beam transport system, while the remaining neutrals are absorbed by the neutral dump and the positrons are swept into a charged particle dump. The electron beam is bent around the neutral dump and transported to the PB6 enclosure where it strikes a radiator, consisting of 20% radiation lengths of lead, to produce a photon beam via the bremsstrahlung process. The electron/photon beam then passes through a series of sweeper magnets which deflect the electron beam into the Recoil Electron Shower Counter (RESH) while the photon beam continues on to the experimental target.

Photons produced in this manner have emerged from a chain of three interactions and a decay; hence, the beam is called a tertiary beam. This type of beam has the advantage of a very low neutral contamination as compared to other methods of producing high energy photon beams. The neutral hadronic contamination for the photon beam is estimated to be less then 1.3×10^{-5} per photon. A disadvantage to this type of beam is that the decay

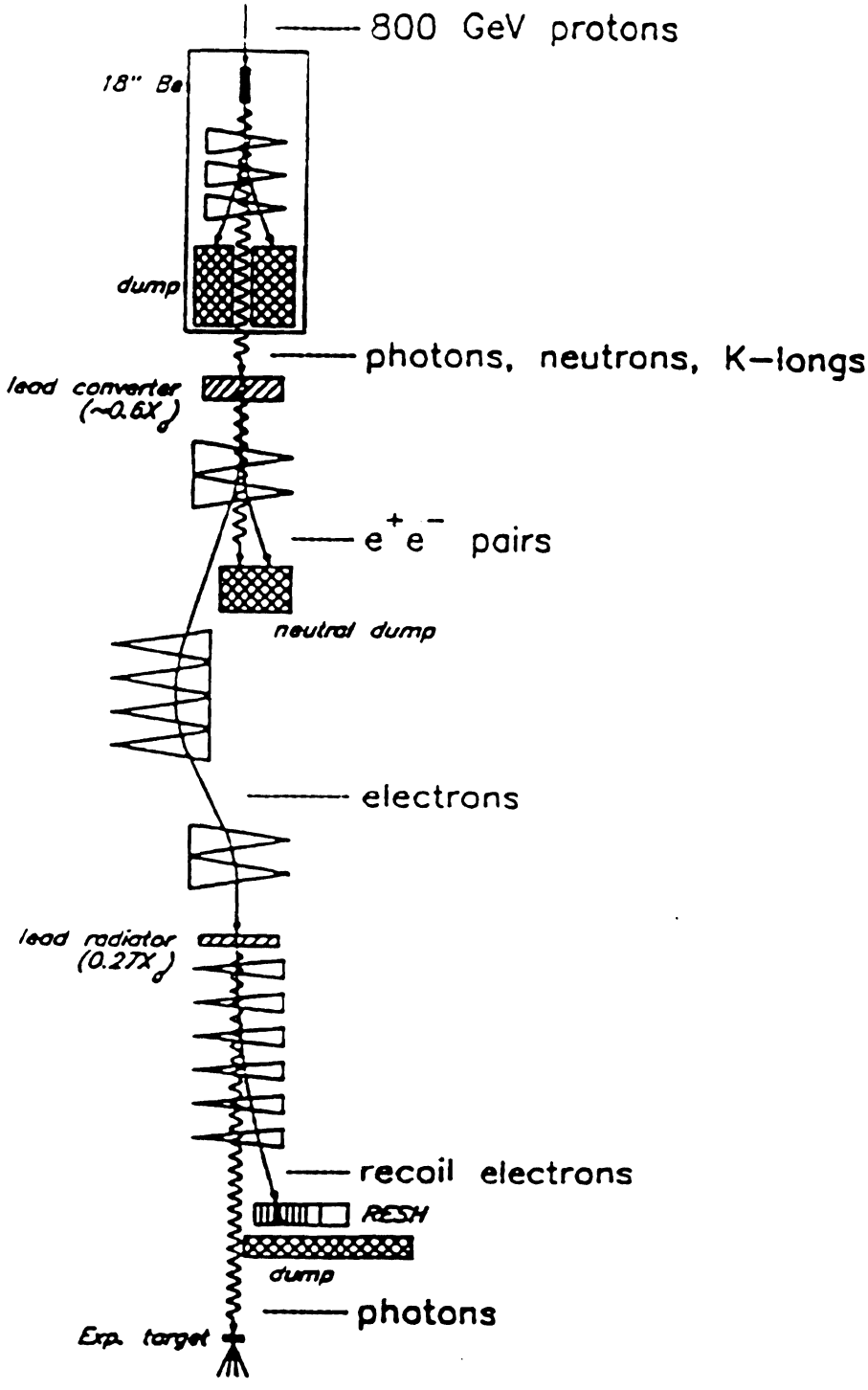

Figure 2.2: The Wide Band photon beam line.

process degrades the final energy of the photon beam. The photon beam spectrum is shown in Fig. 2.3.

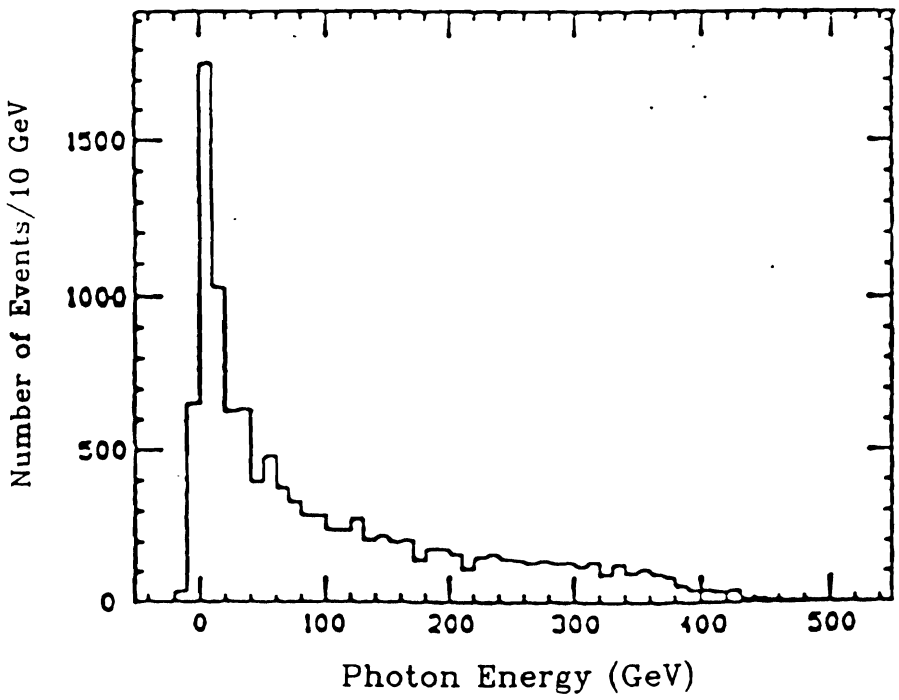

Figure 2.3: The Wide Band photon beam spectrum.

For the 1987-1988 data run, approximately 2×10^{12} primary protons per twenty second spill were incident on the primary production target resulting in approximately 2×10^{7} photons per spill incident on the experimental target. Complete details of the Wide Band Photon Beam can be found in references [24, 25].

2.2 Spectrometer

The E-687 spectrometer is a two magnet spectrometer featuring large acceptance, high resolution tracking, and good particle identification over a large range of momenta. This

combination of detectors allowed for the observation of a large number of charmed baryon and meson decay modes. Complete details of the E-687 spectrometer can be found in reference [25].

2.2.1 Experimental Target

For the 350 GeV/c electron running period, three different experimental targets were used. Two of the targets consisted of different configurations of Beryllium, and the third was a Silicon Wafer "Active" target.

The two Beryllium targets are shown in Fig. 2.4 and are designated 5-Be and 4-Be. The 5-Be and 4-Be targets consisted of five and four pieces of Beryllium respectively. The first one or two segments were square, measuring 2.54 cm on a side and 0.8128 cm thick in the beam direction. The segments were oriented at a 45 degree angle with respect to the vertical. The remaining three Beryllium segments were hexagonal shaped pieces 0.8128 cm thick in the beam direction. The shape was chosen to match the high resolution region of the Silicon Microstrip Detector. The Beryllium segments had gaps between them ranging from 75 to 200 microns. The target lengths were 11.5% and 9.2% of a radiation length for the 5-Be and 4-Be targets, respectively.

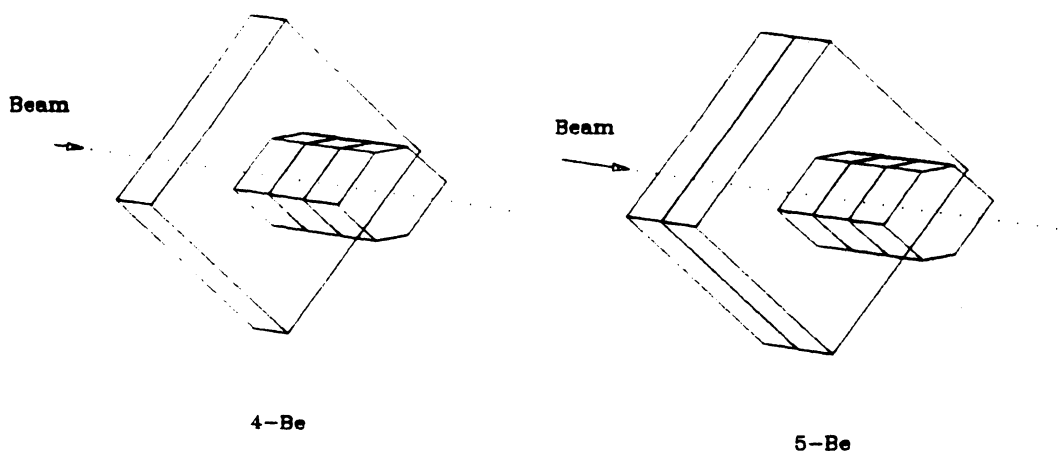

Figure 2.4: The Beryllium targets.

The third target was a Silicon Wafer "Active" target consisting of 50 planes of silicon

strips with an active area of 2 cm $\times$ 2 cm. The detector was assembled with the strips running in alternate crossed geometry to provide a 5 mm$\times$5 mm resolution in the transverse direction. To increase the interaction probability, the first 29 planes had 300 micron thick Beryllium layers between them. The resulting target length was approximately 14% of a radiation length and 4.7% of an interaction length.

Most of the recorded data was taken with the Beryllium targets; approximately 10% was taken with the Silicon Wafer Target. Data from all three targets are used in this analysis.

2.2.2 Beam Tagging

The energy of the interacting photon is given by the relationship:

$$E_\gamma = E_{e^-} - E_{recoil} - \sum E_{\gamma'}$$

where E_γ is the energy of the interacting photon, E_{e^-} is the energy of the incident electron, E_{recoil} is the recoil electron energy, and $\sum E_{\gamma'}$ is the energy of any additional photons in the event due to multiple bremsstrahlung. The incident electron energy was determined by the momentum acceptance of the beam line, which was set at 350 GeV/c with a spread of $\pm$15%. The recoil electron energy was measured by the Recoil Electron Shower Counter (RESH), while the energy of noninteracting photons and pairs was measured by the Beam Gamma Counter (BGM).

After passing through the lead radiator, the electron beam was deflected by a series of six dipole magnets into the the RESH counters. The energy of the recoil electron beam could then be determined from the final position of the the recoil electron or the energy deposited into the RESH. It was then possible to select events with a minimum photon energy based on the RESH response. Use of the RESH detector in the trigger will be discussed in the section on Second Level Triggering.

The RESH detector consisted of ten counters made up of twenty four planes of alternating 1/4 in. lead absorber and 1/4 in. scintillator for a total of 24 radiation lengths. Each counter was read out by a single phototube and the signals were digitized by a LeCroy 1885 Fastbus ADC. The positioning of the RESH shower counters with respect to the photon beam line is shown in Fig. 2.5. The first RESH counter was located approximately 6 in. from the nominal center of the photon beam, while the tenth counter extended to approxi-

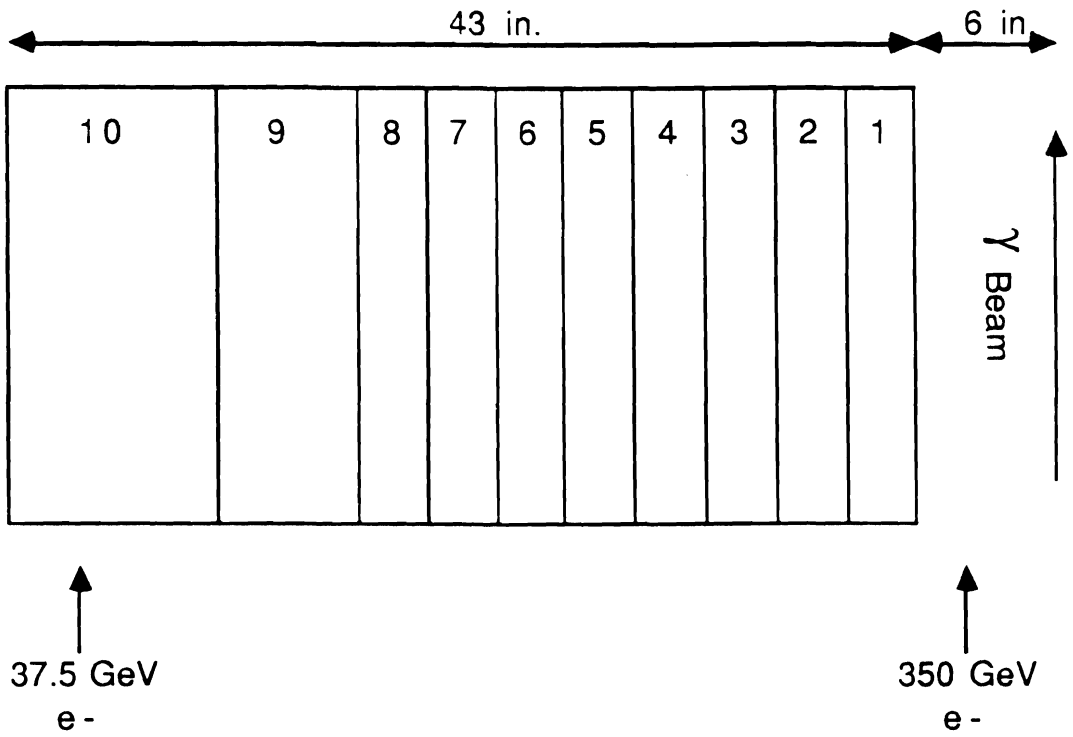

Figure 2.5: The RESH shower counter.

mately 43 in. from the photon beam center. This allowed for tagging photons from about 135 to 310 GeV/c. The upper limit for tagging photons was set by aperture limitations of the sweeper magnets.

The BGM counter served two functions. The first was to monitor the energy of the photon beam by detecting noninteracting photons. The second purpose was to measure the energy of photons from multiple bremsstrahlung and e^+e^- pairs from the target region that were refocused on the counter to determine the energy of the interacting photon. The BGM counter was located downstream of the Hadron Calorimeter (HC) covering the openings in the HC and the inner electromagnetic counters. Constructed of 48 layers of alternating 1/8 in. lead absorber and 1/8 in. lucite detector, the counter was a total of 25 radiations lengths long. Signals from the BGM were read out by a single phototube and digitized by a LeCroy 1885 Fastbus ADC.

2.2.3 Charged Particle Tracking

Two systems comprised the charged particle tracking for E-687. A Silicon Microstrip Detector (SMD) located directly downstream of the experimental target provided good track and vertex resolution for charged particles produced in the primary interaction and subsequent decays, and a Multiwire Proportional Chamber (MWPC) system was used to track charged particles downstream of each of the analysis magnets determining the sign of the charge and the momentum of charged particles.

Silicon Microstrip Detector

Tracking in the region immediately downstream of the experimental target was performed by the SMD. The position of the detector relative to the target is shown in Fig. 2.6.

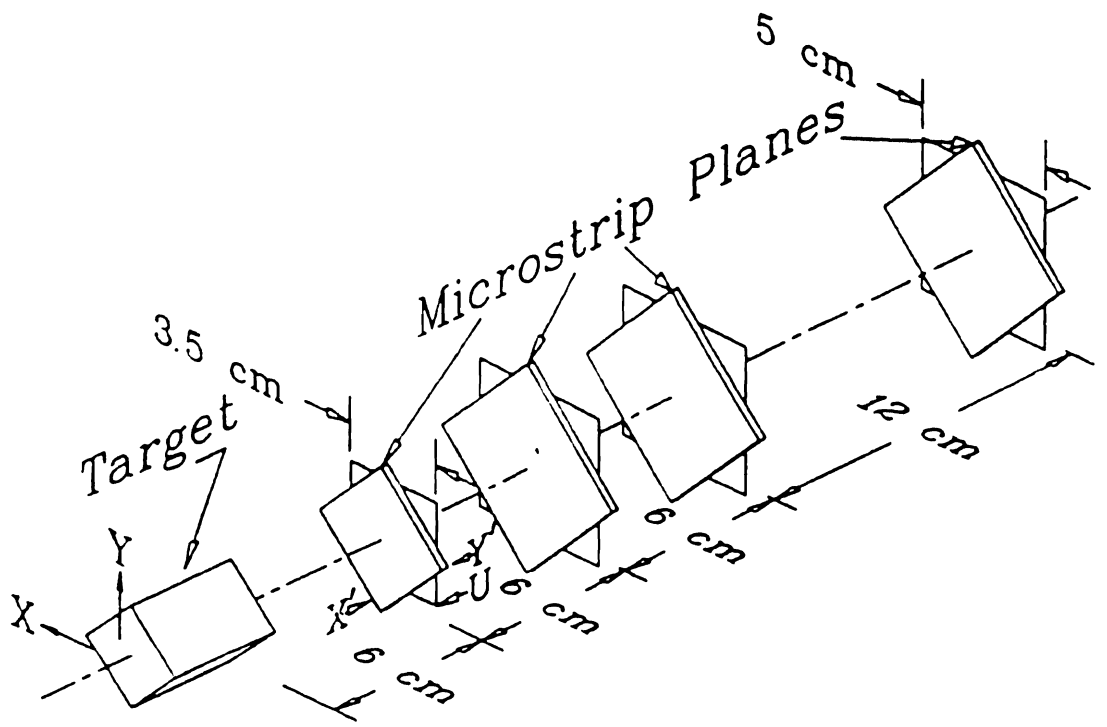

Figure 2.6: The experimental target region.

The detector consisted of 12 planes of silicon microstrips grouped in four stations of three planes. Each station consisted of three views; i, j, and k, oriented at -135°, -45°, and -90° with respect to the vertical. The central region of each plane had a resolution twice

that of the outer region. The first station also had a resolution twice that of the other three stations. The parameters of the four stations are given in Table 2.1.

TABLE 2.1
SILICON MICROSTRIP DETECTOR PARAMETERS

	Station I	Station II	Station III	Station IV
Active Area (cm^2)	2.5×3.5	5.0×5.0	5.0×5.0	5.0×5.0
High Res. Area (cm^2)	1.0×3.5	2.0×5.0	2.0×5.0	2.0×5.0
Strip Pitch (inner, outer)	$25\mu m$, $50\mu m$	$50\mu m$, $100\mu m$	$50\mu m$, $100\mu m$	$50\mu m$, $100\mu m$

Each strip of the SMD was read out by means of a preamplifier mounted on the side of the detector, a remote-end amplifier, and a charge integrating FLASH ADC. The overall efficiency for the system was measured to be greater than 99%, with an extrapolated transverse error to the center of the target of approximately 10 μm for infinite momentum tracks passing through the high resolution region of the microstrips. There was a total of approximately 8000 channels [25]

MWPC's

The MWPC system includes 5 chambers providing hit information in 4 views. The locations of the 5 chamber stations, labeled P0, P1, P2, P3 and P4 from upstream to downstream are shown in Fig. 2.7. Two types of chambers were employed: The smaller Type 1 chambers which were located immediately downstream of each of the analysis magnets, and the larger Type 2 chambers which were used at the three remaining chamber stations. As a result of the October 3, 1987 fire, the Type 2 chamber located at the P4 station was replaced by a smaller chamber with only three views.

The Type 1 chambers, labeled P0 and P3, had an active area of 30 in. $\times$ 45 in. Four sense planes measuring Y, V, U, and X views were contained in each chamber. The X and Y views measured the horizontal and vertical coordinates respectively, while U and V views were rotated by ± 11.6 degrees with respect to the horizontal. The sense planes had a 2 mm wire spacing providing angular resolutions for tracks coming from the target region of

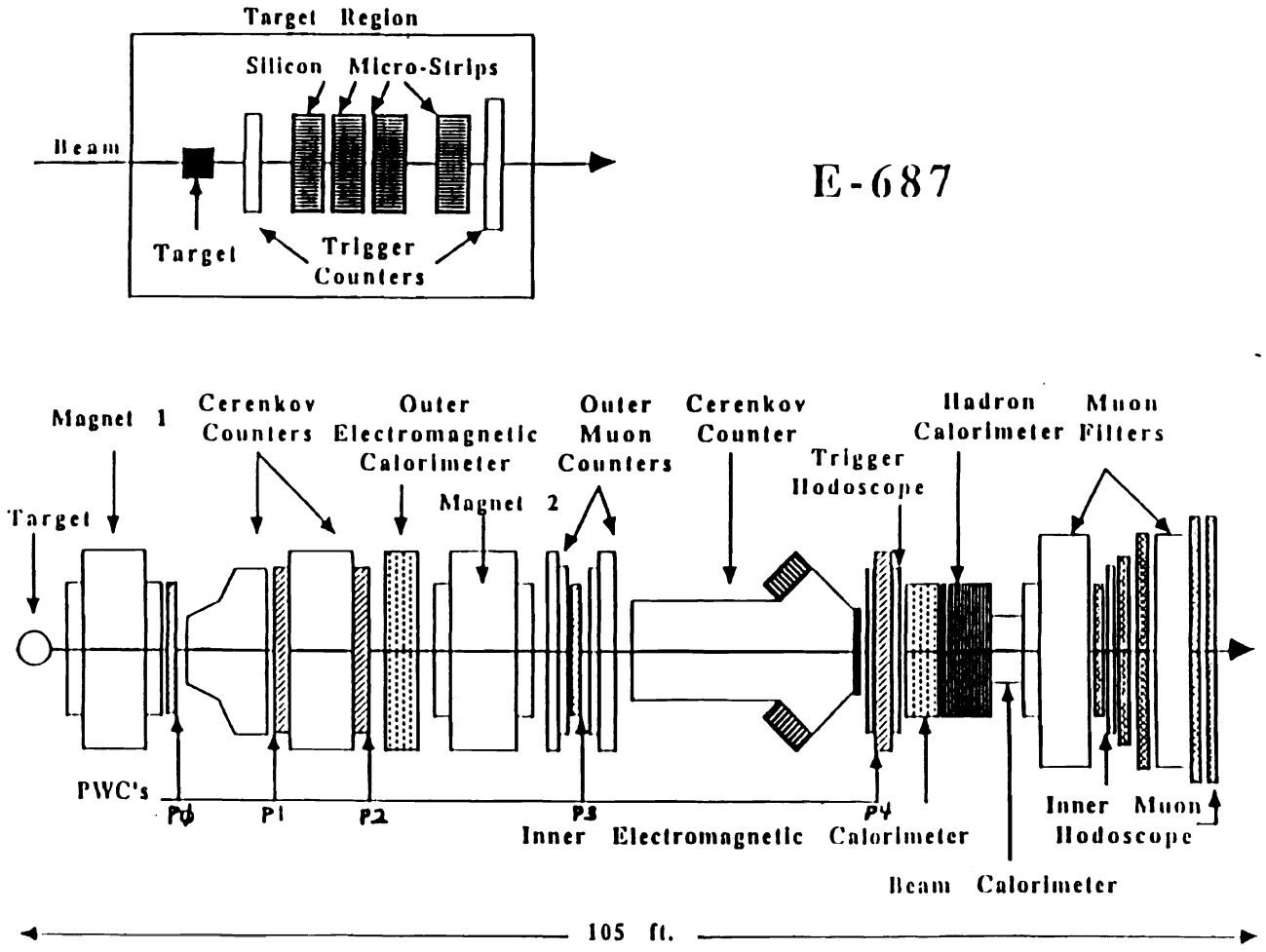

Figure 2.7: The E-687 spectrometer.

approximately 0.49 and 0.13 mrad in the X view for P0 and P3 respectively. The chambers were constructed with a 0.240 in. half-gap between the anodes and cathodes. To insure electrostatic stability, the X plane anode wires were glued to a support wire. Using a 65/35 mixture of Argon/Ethane with 1% Ethyl-Alcohol the chambers operated efficiently with an operating voltage of approximately 2.4kV.

The Type 2 chambers have an active area of 60 in. × 90 in. The orientation of the 4 views is identical to that of the Type 1 chambers. For these, the sense planes had a 3 mm wire spacing providing angular resolutions for tracks coming from the target in the X view of 0.46 and 0.34 mrad for P1 and P2, respectively. A mylar garland was strung between the X plane and the cathode planes to insure electrostatic stability. Operating with the same gas mixture and a 0.250 in. half-gap these two chambers operated efficiently with a 3.1kV operating voltage.

As a result of the fire, it was necessary to replace the original P4 chamber, which was of Type 2 design, with a chamber from a previous experiment, E-400. This replacement chamber, affectionately called Scab-P4, had a smaller aperture, 45 in. × 60 in., and only three views, X, U, and V. The X view had a 3 mm wire spacing, while the U and V views had a 2 mm wire spacing. The orientation of the rotated views, U and V, was ±11.6 degrees with respect to the horizontal. Support wires attached with RTV were placed on all three anode planes for electrostatic stability. The chamber ran on the same gas mixture and operated efficiently at approximately 3.2kV.

Each anode wire of the MWPC system was amplified, discriminated and read out into a LeCroy 4290 TDC system. The Type 1 chambers used 8 channel preamplifier cards with single ended MECL II outputs while the Type 2 chambers used 16 channel preamplifier cards with double sided MECL 10K outputs. The preamplifier cards were mounted on the sides of each of the chambers to the reduce signal loss. The signals were carried to the counting room via 250 to 350 ns Ansley cables where the signals were reshaped before being sent to LeCroy 4291 TDC modules. The 4291 TDC modules were modified for a 127 ns full scale operation and ran in common stop mode. This provided a 1 ns time resolution for the drift time of the hit. Following digitization, the hit information was read out via a dedicated crate controller, reformatted, and read into into a LeCroy Fastbus Memory. In addition, fast hit information from the 4291 TDC was used as part of the second level

trigger. The system had a total of approximately 13,000 channels.

2.2.4 Čerenkov

The E-687 Čerenkov system was comprised of three threshold counters labeled C1, C2, and C3 from upstream to downstream. The location of the three counters with respect to the rest of the spectrometer is shown in Fig. 2.7. Used together, these three counters provided charged particle identification for particles with momenta in the range 5 to 115 GeV/c. The thresholds for each of these counters are shown in Table 2.2.

TABLE 2.2
ČERENKOV THRESHOLDS

Counter	Momentum Threshold (GeV/c)		
	Pion	Kaon	Proton
C1	6.7	23.3	44.3
C2	4.4	16.2	30.9
C3	17.0	61.0	116.2

C1

Located between the MWPC's P0 and P1, this counter provided Čerenkov information for medium momentum tracks. The counter consisted of 90 cells, and used a Helium/Neon gas mixture. A combination of 2 in., 3 in., and 5 in. phototubes was used to read out the cells; the type of tube was determined by the location of the cell. In order to prevent helium poisoning of the phototubes, each phototube had a quartz window located in front of it. Dry nitrogen was flushed through the area between the window and phototube to remove the helium. The counter aperture matched the acceptance of the charged particle tracking.

C2

Using N_2O at atmospheric pressure, C2 provided information for the lowest momenta. Comprised of 110 cells, the counter was located in the region between the P1 and P2 MWPC's. The counter used two plane mirrors oriented at $\pm 45°$ degree angles with respect

to the beam direction. In order to reduce the amount of material in the region of the counter having having high particle density, there was a small vertical gap between the two mirror sections. The counter was read out with a combination of 2 in. phototubes for the inner region of the counter, and 5 in. phototubes for the outer region. Each of the phototubes was coated with a waveshifter to increase the photon detection efficiency.

C3

The highest momentum information was provided by the C3 counter. This counter was located downstream of the second analysis magnet between the P3 and P4 MWPC's. In order to get the high momentum threshold, helium at atmospheric pressure was used. The counter used 100 spherical focusing mirrors to direct the Čerenkov light into either 2 in. or 5 in. phototubes depending upon the location of the cell. To prevent helium poisoning of the phototubes, CaF_2 or quartz windows separated the phototubes from the helium. The region between the windows and PMT's was flushed with dry nitrogen.

All three counters were read out in the same fashion. Signals from the phototubes were read into both a latch system, and the LeCroy 1885 Fastbus ADC system for digitization.

2.2.5 Calorimetry

E-687 had both electromagnetic and hadronic calorimetry to measure the the energy of charged and neutral particles. In addition to the RESH and BGM counters which were described in the tagging section, E-687 had two electromagnetic and two hadron calorimeters.

Electromagnetic Calorimetry

Covering the outer region of the spectrometer was the Outer Electromagnetic (OE) calorimeter located immediately upstream of the second analysis magnet M2. OE had an acceptance of $28 \leq \theta_x \leq 128$ mrad in X and $49 \leq \theta_y \leq 114$ mrad in Y for neutral particles coming from the target region. The counter consisted of alternating layers of lead absorber and plastic scintillator detector. The detector segments were oriented in alternating x-y directions to determine the position of the shower. The OE had a central aperture measuring 51 cm $\times$ 88 cm to allow particles to enter the inner portion of the spectrometer. The scintil-

lator detectors were read out by photomultiplier tubes, and the signals digitized by LeCroy 1885 Fastbus ADC's.

The inner region of the spectrometer was covered by the Inner Electromagnetic (IE) counter. The original counter was destroyed by the fire of October 3, 1987. To provide emergency electromagnetic calorimetry for the inner region, the last two sections of the OE were dismantled and assembled in the location of the IE to provided γ, and e^- detection for the angular region of $2 \leq \theta_{x,y} \leq 26$ mrad. A central aperture of 10.2 cm $\times$ 10.2 cm in the IE allowed noninteracting photons and e^+e^- pairs from the target region to pass through and strike the BGM. This emergency fix degraded the performance of the OE by the loss of full containment of the showers and caused a mismatch in the angular acceptance of the two counters; however, reasonable γ and π^0 detection and electron-hadron separation were achieved.

Hadronic Calorimetry

Two systems were responsible for hadron calorimetry. The primary function of the hadron calorimetry was to reject e^+e^- pairs and enhance the selection of events with charm in the second level trigger. The first system is the Hadron Calorimeter (HC) which was located downstream of the IE, covering an angular region from 5 to 30 mrad. The center of the HC had a 6 in. diameter hole to allow the noninteracting photons, and e^+e^- pairs from the target region to pass through and strike the BGM counter. The HC consisted of 28 planes of 1.75 in. thick iron and 28 sense planes interleaved between the iron for a total of 8 interaction lengths. Each sense plane consisted of proportional tubes which were read out though capacitive pads. The pads were arranged in eight concentric circles which were subdivided into 24 azimuthal sections as shown in Fig. 2.8. The HC was subdivided into three sections along the beam direction. Pads in each section were ganged together longitudinally along the beam direction to provide a tower geometry. This readout arrangement allowed for generating both total energy and transverse energy information for triggering. For the 1987-1988 data run only the total energy was used in the trigger.

The outermost beam left section of HC was severely damaged as a result of the fire. This section was disabled for the 350 GeV electron beam running.

The second calorimeter was the Central Hadron Calorimeter, CHC, which covered the

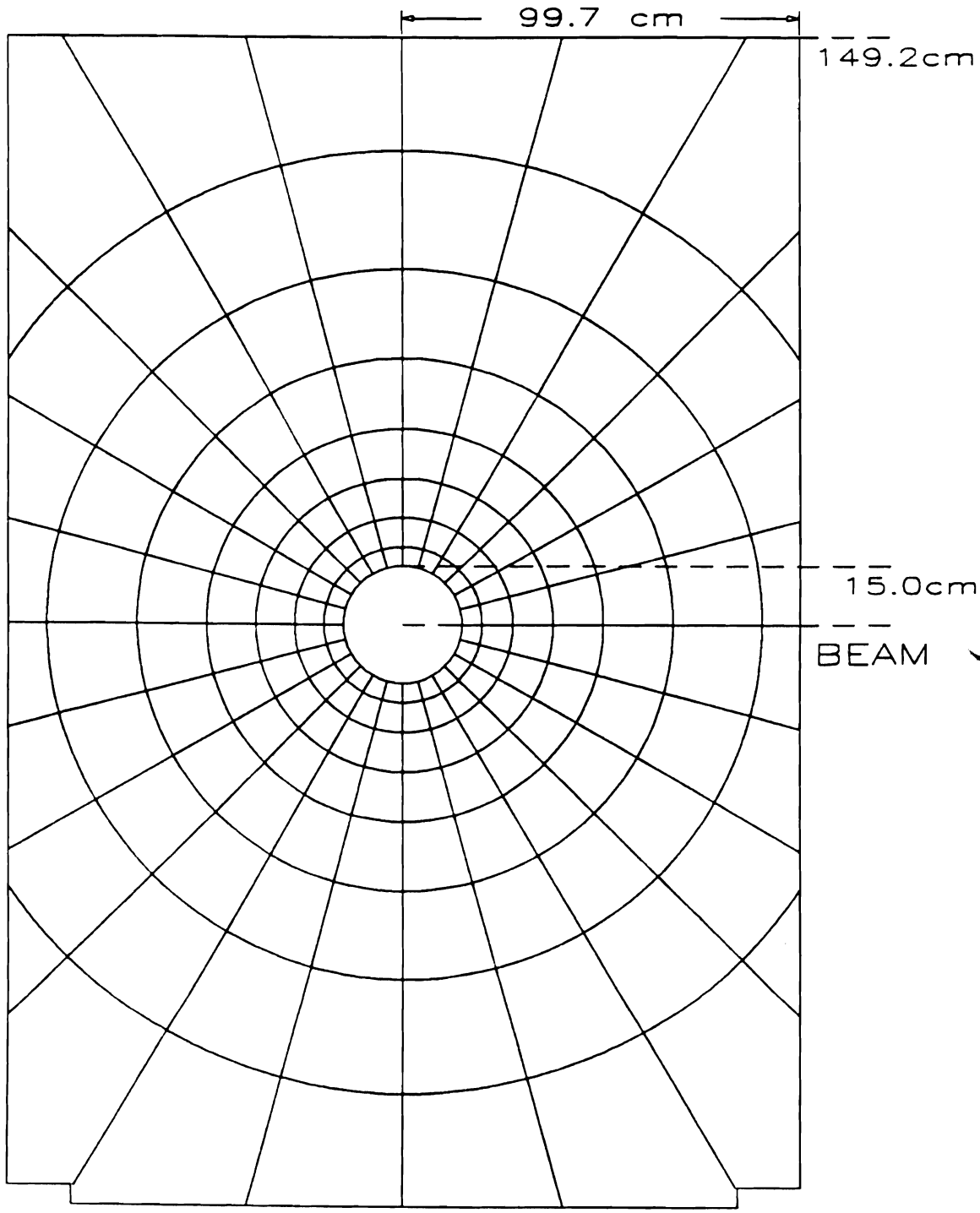

Figure 2.8: The hadron calorimeter pad arrangement.

central 5 mrad of the spectrometer. The CHC was located downstream of the BGM immediately before the muon filter. The counter consisted of 16 planes of depleted uranium 1.5 in. thick, sandwiched between two 3/32 in. thick pieces of iron interspersed with polystyrene scintillator detector. The counter was a total of 6.4 interaction lengths long. The first 12 layers of scintillator were read out by a single PMT, while the last 4 scintillator layers were read out by a second PMT. The energy signals were incorporated into the total energy trigger, and treated as a single tower for analysis purposes.

2.2.6 Muon

Muon detection was done by two systems. The first system was the Outer Muon (OM) counters located downstream of the the second analysis magnet, M2, using the steel yoke of the magnet as a filter; the second system was the Inner Muon (IM) counters located behind a steel and concrete muon filter at the downstream end of the spectrometer. Each system consisted of horizontal and vertical scintillator counters and proportional tubes. The OM counters had a central aperture that matched the aperture of M2. Signals from the scintillator counters were used to form the dimuon triggers.

2.2.7 Triggering

Triggering was done in a two step process. The first level, or Master Gate, selected events consistent with being hadronic in nature, with minimal biases. The second level was to select events that had a high probability of containing charm, while rejecting electromagnetic events passing the Master Gate.

First Level Trigger

The Master Gate was derived from seven sets of scintillator counters arranged to select hadronic photon interactions, and reject electromagnetic events. The first three counters were veto counters located upstream of the target region to reject events from charged particles in or near the beam or from interactions occurring upstream of the experimental target. The first counter, AM, is an array of 24 elements covering an area of dimensions 1.5 m $\times$ 2.5 m located approximately 8 meters upstream of the experimental target sur-

rounding the beam line. The A0 counter was located approximately 7 meters upstream of the target. This was a small scintillator counter located inside the beam line. The TM counters were located about 2.5 meters upstream of the target and consisted of two counters covering 45 cm $\times$ 61 cm area surrounding the beam line.

To select interactions with at least one charged particle, two small trigger counters, TR1 and TR2, were located downstream of the experimental target. TR1 was located immediately upstream of the SMD, while TR2 was located downstream of the SMD. The size of the counters was chosen to match the active area of the microstrip system. Thresholds on the discriminators for these two counters were set to be sensitive to single minimum ionizing particles.

To select possible hadronic interactions and reject electromagnetic events, two arrays of counters were used. The first was the OH counter hodoscope, an array of 24 scintillator counters located on the face of the OE to detect the wide angle charged particles in the event. The signals from these 24 counters were connected in a logical OR to form a single OH logic signal. The second array, called H$\times$V, was located between P4 and IE. The H$\times$V array consisted of two planes of scintillator counters, 24 placed horizontally and 12 vertically, divided into two sections with a 7.5 cm vertical gap centered on the beam line. The signals from the H$\times$V counters formed logic signals, $(\mathrm{H}\times\mathrm{V})_{1body}$ and $(\mathrm{H}\times\mathrm{V})_{2body}$ to indicate the presence of 1 and 2 charged particles outside of the central beam region. A schematic of the H$\times$V array and the logic for these logic signals is shown in Fig. 2.9. The Master Gate (MG) logic was then formed from the individual logic signals:

$$MG = (TR1 \cdot TR2) \cdot \{(H \times V)_{2body} + OH \cdot (H \times V)_{1body}\} \cdot \overline{(A0 + TM1 + TM2)}$$

Second Level Trigger

There were several second level trigger sets used during the 1987-1988 data run. The trigger sets were chosen based on specific physics goals and the final second level trigger was an OR of the individual trigger sets. The MG started the readout of the individual detector elements and started the formation of the second level trigger sets. The second level trigger decision was made within 1 μs after the MG. If the event did not satisfy any of the second level trigger sets, then the DAQ was reset and readied for the next MG.

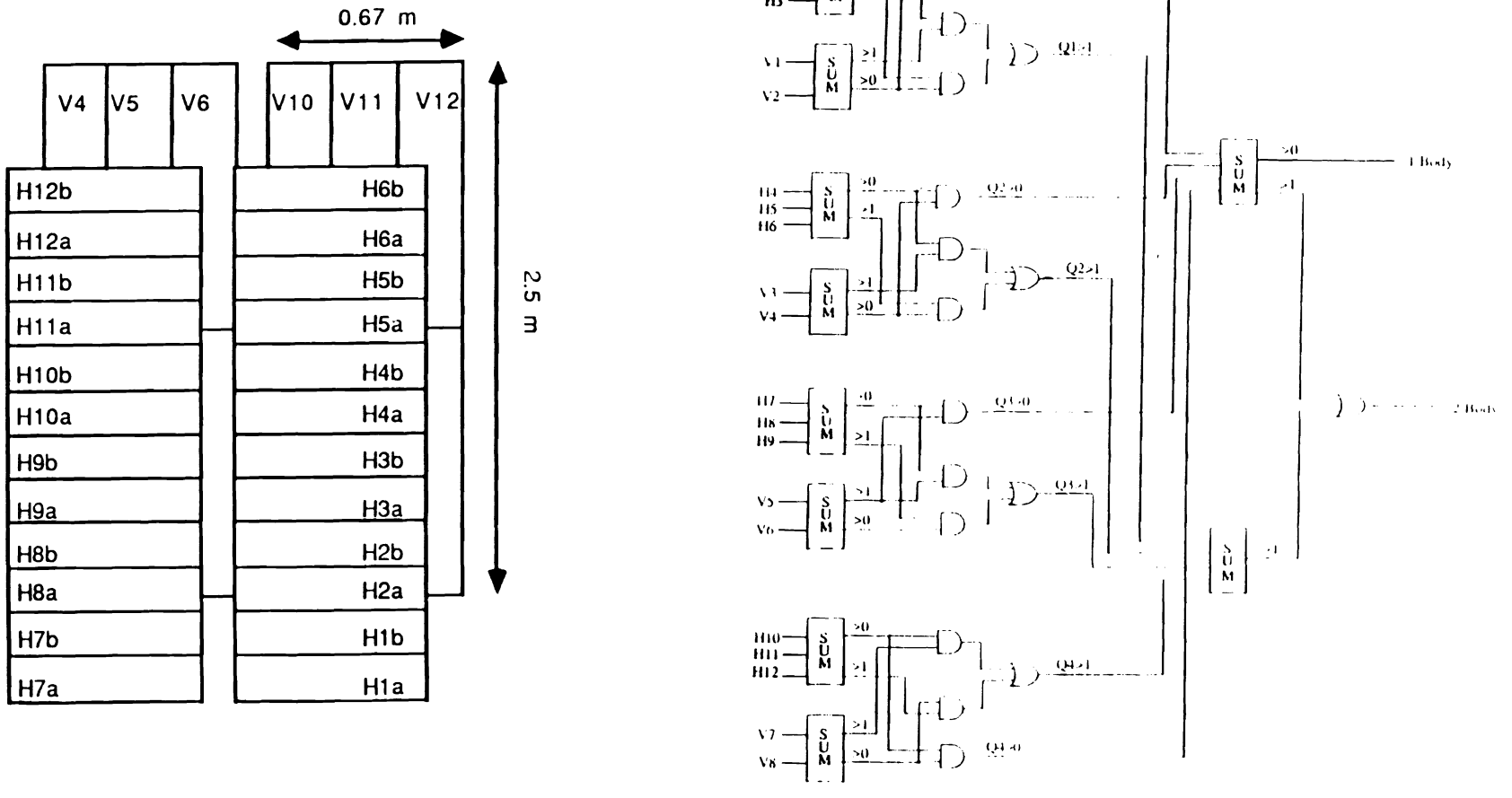

Figure 2.9: H×V hodoscope and logic.

The second level trigger sets were: Energy Trigger, Inner-Inner Muon, Inner-Outer Muon, Master Gate, and Pair. The Energy Trigger set was the dominate trigger set and accounted for approximately 80% of the total triggers. The energy trigger was formed from three buslines: EHADM, which indicated the presence of at least 35 GeV of energy in HC and CHC; RESHL, which signaled the presence of a photon with at least 135 GeV of energy; and 1_TRAC, which indicated the presence of at least one hit in the X view of P0 outside of the central pair region. The two muon trigger sets were designed for the study of J/Ψ production, while the Master Gate and Pair triggers were designed for normalization and efficiency studies. A typical spill resulted in approximately 1500 second level triggers which were subsequently written to magnetic tape.

2.2.8 Data Acquisition

At the beginning of each spill, the data acquisition cycle started, inhibits were removed, and the DAQ system was readied for accepting events. Approximately 300 ns after an interaction occurred in the experimental target the MG was generated. The MG initiated the digitization or latching of signals from the different detector elements, started the formation of the second level trigger, and generated a 1 μsec long veto which inhibited the formation of additional MG's. If a second level trigger was formed, then the readout of the ADC's, TDC's, and latches was initiated, and a busy signal was issued, blocking new master gates and second level triggers. If a second level trigger was not formed, then a fast clear was issued and the DAQ was reset for a new event.

For events satisfying the second level trigger, the signals were readout in parallel to four LeCroy 1892 Fastbus Multiple Record Buffer Memories and a University of Illinois Fastbus Memory Module. Once the signals were read into the Fastbus Memories, the busy signal was dropped and the electronics were readied for the next master gate. The fastbus memories were then read out to a PDP 11/45 which concatenated the event from the five memories, added run, spill, and event identifiers, and wrote the event to tape. In addition, at the end of each spill the PDP 11/45 read out the event scalers through parallel branch CAMAC and wrote the results to magnetic tape. A small fraction of the events was sent in parallel to a VAX 11/780 via a DR11W link for online monitoring. A schematic diagram of the E-687 data acquisition system is shown in Fig. 2.10.

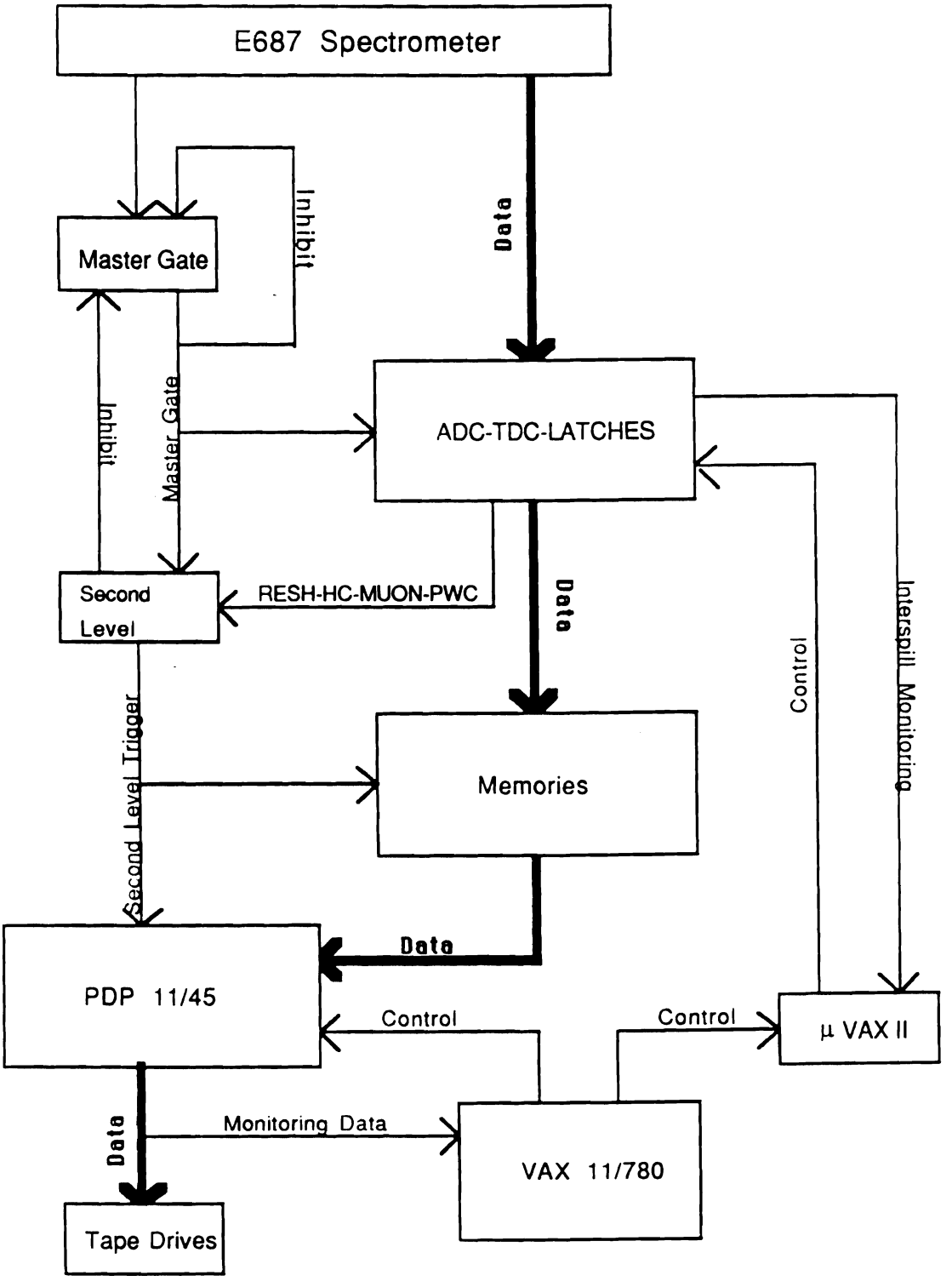

Figure 2.10: Schematic of the E-687 DAQ.

CHAPTER 3

DATA RECONSTRUCTION AND REDUCTION

The E-687 reconstruction program was contained in a single package called PASS 1. The goal of PASS 1 was to produce a reconstructed output tape which could be used to produce charm signals without significant additional analysis. In order to achieve this goal the PASS 1 package performed the following analyses: Microstrip track reconstruction, PWC track reconstruction, linking of microstrip and PWC tracks, vertexing, neutral vee finding, Čerenkov particle identification, muon identification, and calorimetry analysis including recoil electron shower analysis, beam gamma shower analysis, inner and outer electromagnetic calorimetry analysis, and hadron calorimetry analysis. The PASS 1 package was assembled and implemented on the Fermilab Advanced Computer Project (ACP) system in April of 1989. An average raw data tape containing 50 thousand events required 200 ACP node hours to be analyzed. Analysis of the postfire data sample was completed in October 1989. A total of 60 million events was reconstructed. Of these, 47 million events passed the minimal PASS 1 cut requirements.

Following the PASS 1 reconstruction, the data sample was subdivided into smaller data sets based on physics criteria. This was accomplished in two separate stages. The first, SKIM 1, provided diagnostics of PASS 1 results and a selection of charm meson and baryon events to tune up future analysis efforts. SKIM 1 ran in parallel with PASS 1 using the Fermilab AMDAHL and was completed in December of 1989. The second skim, SKIM 2, was a more detailed skim, implementing the results of studies using SKIM 1 events and correcting for undesirable PASS 1 "features". SKIM 2 was implemented on the Fermilab AMDAHL in February 1990, and completed in April 1990. A typical PASS 1 output tape with 20 thousand events required 45 minutes of AMDAHL CPU time while selecting 10

thousand events.

3.1 Track Reconstruction, Linking, and Momentum Determination

The tracking was done in two steps. Tracks were first reconstructed in the microstrip system, followed by track reconstruction in the MWPC system. After the tracking was completed, tracks from the two systems were linked together and the hits refitted to get the best momentum vector for each track.

3.1.1 MICRORICO

Reconstruction of microstrip tracks was done by the MICRORICO tracking package using a projection finding algorithm in the three views. Final arbitration of tracks was then performed after all possible space tracks were found in order to reduce biases based on track ordering [26].

The first step was the analysis of clusters of adjacent hits to reduce the combinatorics. Final hit positions were assigned based on the interpolation of the charge deposited in the strips. Next, track projection candidates were generated in each of the three views, requiring at least three hits per projection. Hit sharing was allowed except in the case of hits in the last three stations of a four station projection being used in a three station projection. Projection candidates were then combined to form space tracks. The track was kept if the global χ^2/DOF was less then 8.0. Tracks sharing projections were arbitrated based on the χ^2/DOF of the tracks. At this point hits not used in any tracks were formed into triplets for the purpose of identifying wide angle or highly multiple Coulomb scattered track segments.

Due to the conservative arbitration, this algorithm often generated clusters of space tracks. Final arbitration was performed to reduce these clusters of tracks to a single space track. This arbitration was based on the number of shared hits and the χ^2/DOF of the tracks.

The efficiency of this algorithm has been studied in Monte Carlo and determined to be greater then 95% for tracks with a momentum greater then 4 GeV/c [27]. The resolution for tracks extrapolated to the center of the target and passing through the high resolution

region of the microstrip system was determined to be:

$$\sigma_x = 11\mu m\sqrt{1 + \left(\frac{17.5GeV/c}{P}\right)^2} \tag{3.1}$$

$$\sigma_y = 7.7\mu m\sqrt{1 + \left(\frac{25.0GeV/c}{P}\right)^2} \tag{3.2}$$

where the second term in the square root represents the effects of multiple Coulomb scattering [28].

3.1.2 TRACK 1

The MWPC track reconstruction package, TRACK 1, used a projection matching algorithm to form tracks using hits in the MWPC system. The first four MWPC chambers provided hit information in four views, X, Y, U, and V, and the last chamber, P4, provided hit information in three views, X, U, and V. X and Y are the horizontal and vertical directions respectively, while U and V are rotated $\pm 11.6°$ with respect to the horizontal.

In order to reduce the combinatorics, track information from the MICRORICO package was used to seed the X (non-bend-view) projection finding in the MWPC system. MICRORICO tracks were projected into P0 and X hits predicted. If a matching hit was found, the projection was extended to P4 and an X hit searched for. If a hit was found in P4, then P1, P2 and P3 were searched for matching hits in the X view. If five hits were found, the projection was fitted with a straight line using a least squares fit to generate the slope and intercept of the track projection. After all of the MICRORICO tracks were projected into the spectrometer, the unused hits in P0X and P4X were used as seeds for finding unlinked projections. If hits were found in all five chambers then the hits were fitted using a least squares fit to determine the slope and intercept for the projection.

After all non-bend-view projections were found, the bend-view projections were searched for. For a given bend view, hits in P0 were matched with hits in P2, and a P1 hit was predicted. If a hit was found, the track was extended to the approximate bend-center of M2. This pseudo hit was then connected to hits in P4 and a hit in P3 was predicted. If a hit was found in P3, then the five hits producing the projection were fitted to obtain the slope, intercept and bend-angle in M2 for the projection.

Once all of the projections were found, the projections were matched to form space

tracks. The four projections are related by the relationships:

$$U = X \sin\theta + Y \cos\theta, \tag{3.3}$$

$$V = -X \sin\theta + Y \cos\theta, \tag{3.4}$$

and,

$$\delta U' = \delta V' = \delta Y' \cos\theta. \tag{3.5}$$

where θ is the magnitude of the angle of rotation between the U or V planes and the horizontal. X, Y, U, and V are the intercepts of the projection at the M2 bend-center for the track segment between the two analysis a magnets. $\delta U', \delta V'$, and $\delta Y'$ represent the change in the slope due to the M2 magnetic field. Since the analysis magnets bend in the Y direction, tracks were allowed to share the X projection; however, the U, V, and Y projections for each track had to be unique. Tracks consisting of four projections were the first to be constructed, followed by three projection and two projection tracks. Hits were then searched for in the missing projections. The final step was to refit the track using all of the hits assigned to the track and taking into account the magnetic corrections to get the final set of track parameters to describe the track.

Once all five-chamber tracks were found, unused hits in P0, P1, and P2 were used to form three-chamber projections. These projections were matched using the above relationships to form three-chamber tracks, or stubs. The stubs were refitted with magnetic corrections to get the best set of slopes and intercepts.

After stubs were formed, the remaining hits in P0 and P1 are formed into triplets and quadruplets in an attempt to recover low momentum tracks. MICRORICO tracks were extended through M1 and matches in the X projections were searched for in P0 and P1. If they were found the track was refitted to determine the slopes and intercepts. In a similar manner stubs were extended to P3 and P4 to look for matching triplets. If found, the track was refitted to get a new set of slopes, intercepts, and bend angle.

After all possible extensions were done, remaining unused triplets in P0 and P1 were connected to form pseudo-stubs. In order to eliminate spurious combinations, these tracks were required to point back to the target, and not point into P2.

3.1.3 Linking and Momentum Determination

Linking of Microstrip and MWPC tracks was done using the following procedure. First, microstrip and MWPC tracks were projected to the bend-center of M1, and the two segments were required to match in X and Y intercepts and X slope. Matching tracks were then refitted with a least squares fit using both microstrip and MWPC hits. Links were arbitrated based on the global χ^2/DOF of the fit. In the case of five-chamber tracks the bend-angle in each of the magnets was required to be consistent. The asymptotic efficiency is found to be 97.0% and 91.4% for five-chamber and three-chamber tracks respectively [29].

The momentum of a particle is determined by the bend-angle in M2 for five-chamber tracks and in M1 for three-chamber tracks. For linked three-chamber tracks the bend-angle is determined by the microstrip track parameters in the upstream region, and the MWPC track parameters in the region downstream of M1. For unlinked three-chamber tracks, the momentum was determined assuming the three-chamber track originated at the center of the target. The momentum resolution was calculated to be

$$\frac{\sigma}{P} = 1.4\% \left(\frac{P}{100\ GeV/c}\right) \sqrt{1 + \left(\frac{23\ GeV/c}{P}\right)^2} \tag{3.6}$$

for five chamber tracks, and

$$\frac{\sigma}{P} = 3.4\% \left(\frac{P}{100\ GeV/c}\right) \sqrt{1 + \left(\frac{17\ GeV/c}{P}\right)^2} \tag{3.7}$$

for three-chamber tracks. The second term in the square root represents the effects of multiple scattering [30].

3.2 Vertexing

Vertexing was accomplished via two independent algorithms. The first, a global-vertex algorithm, attempted to reconstructed the vertex topology using only the microstrip track information and was done as part of PASS 1. A second candidate-driven vertexing algorithm was implemented at the skim level and in subsequent analyses.

3.2.1 Global Vertexing

The global-vertex algorithm proceeded as follows. All microstrip tracks were first considered as part of a common vertex, and the tracks were refitted with the added constraint that

they originate at this common vertex. The track with the largest χ^2 contribution was then removed from the vertex and a refit of the remaining tracks was performed. This process continued until the χ^2 became smaller than a predefined value. Unused tracks were then used to find additional vertices using the same procedure. Each time a new vertex was found, unused tracks for that vertex were added back in to recover erroneously disregarded tracks, or tracks assigned to a different vertex. This approach insured that the vertex finding is insensitive to track ordering [31].

3.2.2 Candidate Driven Vertexing

A powerful approach to vertexing is the candidate-driven algorithm, DVERT. This algorithm determines the location of the candidate decay vertex, the production vertex, the decay length, and the errors associated with these quantities. Since this approach assumes a specific decay process, it was implemented at the skim and final analysis levels.

The first step in the candidate-driven algorithm was to determine the the covariance matrix for all microstrip tracks. The covariance matrix took the form:

$$< \delta t_\alpha \delta t_\beta >= H^{-1}_{\alpha\beta} \left(1 + \frac{P^2_\alpha}{p^2}\right) \tag{3.8}$$

where P_α is the 4×4 resolution covariance matrix which includes contributions for multiple Coulomb scattering in the target and spectrometer and resolution effects for different regions of the microstrip detector [32].

Next, a set of linked tracks consistent with the desired final state was chosen. In the case of vees, the momentum vector of the vee was treated as a "pseudo-track" with the associated errors dependent on the vee type: Vees found in the microstrip detector were assigned an error based on the errors for the two microstrip tracks forming the vee, while vees reconstructed downstream of the microstrip system were assigned large errors to minimize their impact on the vertex fit. The vertex for these tracks was then determined, and the candidate-state momentum vector generated. The candidate-state momentum vector then formed the seed for the primary vertex finding. Each microstrip track that was not part of the charm candidate and not linked to two MWPC tracks, was eligible for inclusion in the primary vertex. These tracks were then combined with the candidate-state vector. If the confidence level for the vertex was greater than 2%, the track candidate was kept. From this

subset of tracks, all two-track combinations with the candidate-state vector were made. The vertex with the best confidence level greater than 2% was then kept and candidate microstrip tracks were then added to the vertex as long as the confidence level remained greater then 2%. If no two-track combination satisfied the confidence-level cut, then the best single-track vertex was kept. If the primary vertex contained more then one microstrip track, the state vector was removed and the vertex refitted to remove correlations between the primary and secondary vertices. The final step was to fit the decay-in-flight distance, L, using an impact parameter fit and determine the error, σ_L, in this distance. The quantity L/σ_L was then an unbiased measurement of the significance of separation for the two vertices.

3.3 Neutral Vee Finding

Events containing strange particles, are a good place to start searching for charm events. In addition to charged kaons, there are also the neutral vees – K_s^0's and Λ's. These particles have a relatively long lifetime compared to charm particles, typically several tenths of a nanosecond, and decay predominately into two charged particles with the vertex well separated from the primary vertex and secondary charm vertices.

The E-687 spectrometer had approximately nine meters of decay length in which K_s^0's and Λ's could be detected and reconstructed. This region started at the target and continued to the third MWPC station, P2. The topology of the decays lent itself to subdividing the neutral vees into three categories based on the types of tracks included for the decav particles. The first group included microstrip vees, where the vee decayed in the region upstream of the fourth stack of microstrip planes. Decays occurring in the region upstream of the first MWPC station, P0, made up the second group of vees, M1 vees. Reconstruction vees comprised the third category. These were decays occurring in the region downstream of the the first MWPC station, P0, and upstream of the third MWPC station, P2.

3.3.1 Microstrip Vees

The Microstrip vees were further subdivided into two groups. The first, SSDVEES, consisted of decays in which both of the daughter tracks left sufficient hits in the microstrip system to form standard microstrip tracks linked to MWPC tracks. The following algorithm was

employed to identify these decays: All two track combinations of opposite signed linked tracks were fitted to form a vertex. This vertex was then required to be at least 20σ downstream of the primary vertex, and the neutral vee track was required to point back to within 1 mm of the primary vertex in the transverse plane.

The second group of microstrip vees, MICVEES, consisted of vees decaying in the 18 cm region downstream of the first stack and upstream of the last stack of microstrip planes. To identify these vees, unlinked MWPC tracks were pointed back into the the fourth stack of microstrip planes and a triplet of unused microstrip hits was searched for. If one was found, the upstream track parameters were recalculated using the additional information; the track was then extrapolated into the third stack, a triplet was searched for, and the track was refitted using all hits. In cases where more then one triplet or pair of triplets was found for a given MWPC track,the triplets with the best χ^2 for the global fit were chosen. Next, all opposite sign combinations of candidate tracks were tested for distance of closest approach. If a candidate track was part of more then one combination, then only the combination with the minimum distance of closest approach, DCA, was kept. Finally a loose cut on the $\pi^+\pi^-$ and $p\pi^-$ invariant masses was made to select possible K^0_s's and Λ's. Distributions of the $\pi^+\pi^+$ and $p\pi^-$ invariant masses for the microstrip vees are shown in Fig. 3.1.

3.3.2 M1 Vees

The second category of vees consisted of unlinked pairs of opposite-sign MWPC tracks. This category was further subdivided into three types of vees based on the types of tracks used: Track-Track vees composed of two five-chamber tracks, Track-Stub vees composed of a five-chamber and a three-chamber track, and Stub-Stub vees consisting of two three-chamber tracks. The basic algorithm for each of these categories was the same with minor modifications for the types of tracks used. The first step was to intersect the tracks in the X view to determine an approximate Z position for the decay vertex. Next, the Y position of the decay vertex was determined by tracing each of the tracks through the magnetic field. This procedure was then iterated until the decay vertex fit converged or a maximum number of iterations was completed. The Stub-Stub vees had the additional constraint that the vee momentum vector point back to the primary vertex and the transverse momentum

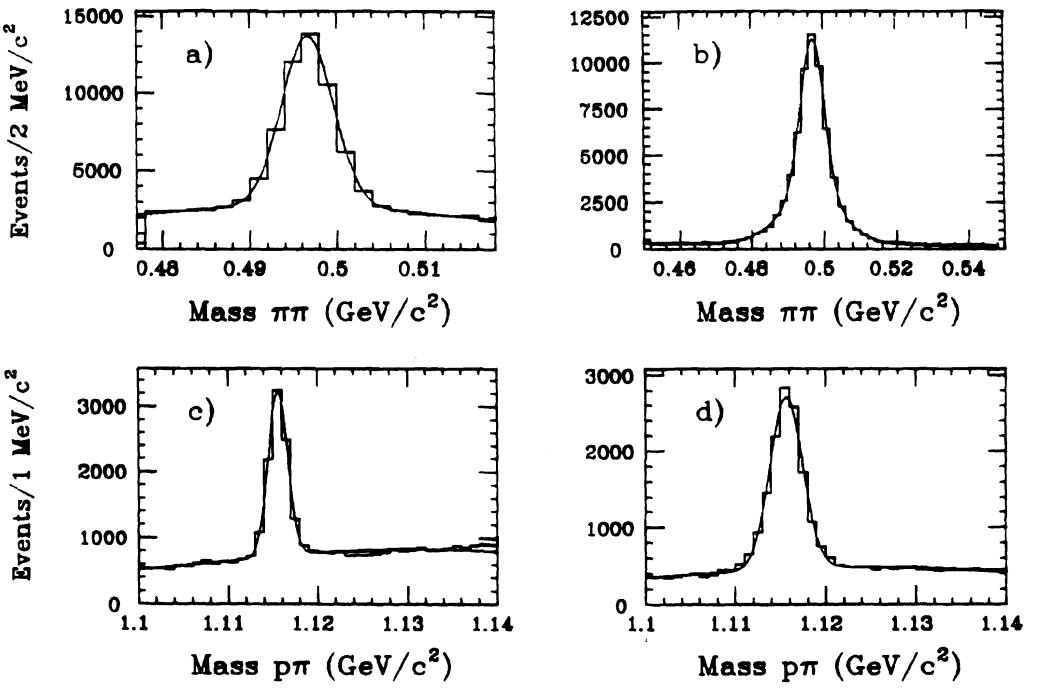

Figure 3.1: Invariant mass distributions for microstrip vee K^0_s and Λ candidates: a) SSDVEE K^0_s, b) MICVEE K^0_s,c) SSDVEE Λ, and d) MICVEE Λ. Λ candidates have additional skim requirement cuts described in Sec. 3.6.1.

be balanced about this direction. The two tracks were then refitted simultaneously with the constraints that the tracks originate from a common vertex and point back to the primary vertex. If the fit was successful, the vee momentum vector and the $\pi^+\pi^-$ and $p\pi^-$ invariant masses were determined from the results of the fit; otherwise the track parameters resulting from the trace were used [33]. The $\pi^+\pi^-$ and $p\pi^-$ invariant mass distributions are shown in Fig. 3.2.

3.3.3 Reconstruction Vees

The highest momentum vees decay in the region downstream of the first chamber station, P0. Since there were no hits in the P0 chamber from the daughter tracks of these vees, tracks from the charged daughters were not found by the TRACK 1 tracking package. In order to find these vees, a special track reconstruction algorithm was employed. Searches were first made for tracks from decays in the region between P0 and P1, and then for tracks from decays in the region between P1 and P2. The algorithm for each of these

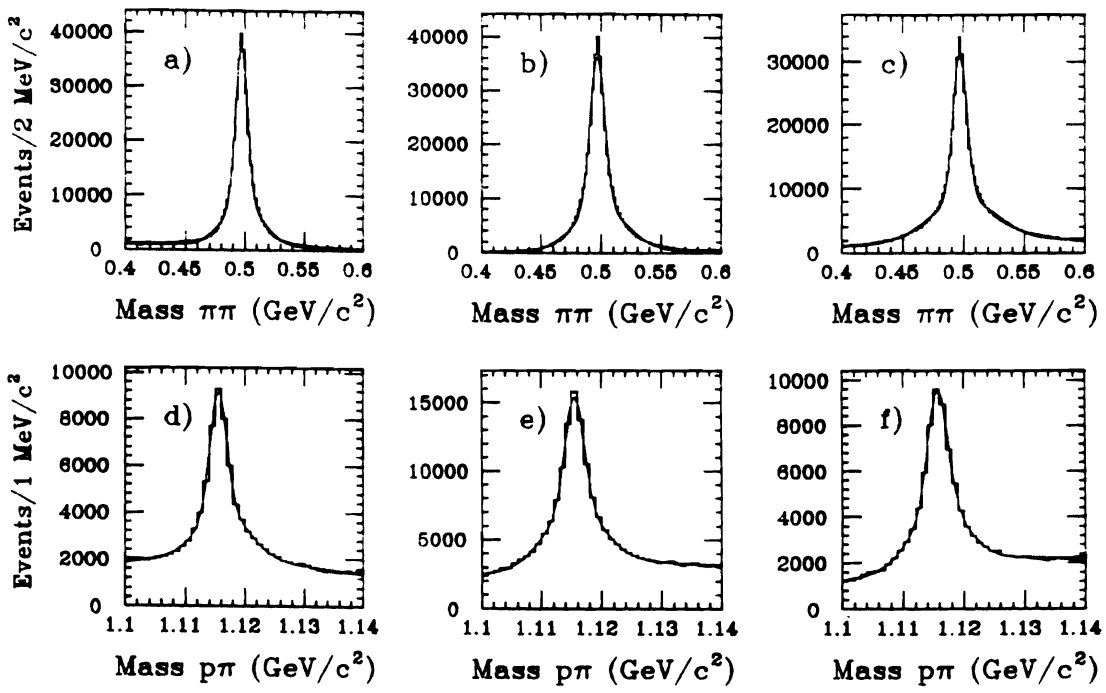

Figure 3.2: Invariant mass distributions for M1 vee K_s^0 and Λ candidates: a) Track-Track K_s^0, b) Track-Stub K_s^0, c) Stub-StubK_s^0, d) Track-Track Λ, e) Track-Stub Λ, and f) Stub-StubΛ. Λ candidates have additional skim requirement cuts described in Sec. 3.6.1.

topologies was the same. The first step was to form projections in the X view from unused hits and hits that were part of low quality tracks. Projections were required to have at least one hit in either P1 or P2 and one hit in either P3 or P4. Next, the projections were matched to hits in the U, V, and Y views to form tracks. Pairs of tracks were then matched with the requirement that they be of opposite sign and intersect in the appropriate region. The pairs of tracks were then refitted with the constraint that the tracks form a common vertex taking into account magnetic corrections. For cases where there were hits only in P2 and P3, there were the additional constraints that the vee momentum vector point back to the primary vertex and the transverse momentum balance about this direction. Vee candidates were then arbitrated to insure that no X-projection was used in more then one vee candidate [34]. The $\pi^+\pi^-$ and $p\pi^-$ invariant mass distributions for reconstruction vees are shown in Fig. 3.3.

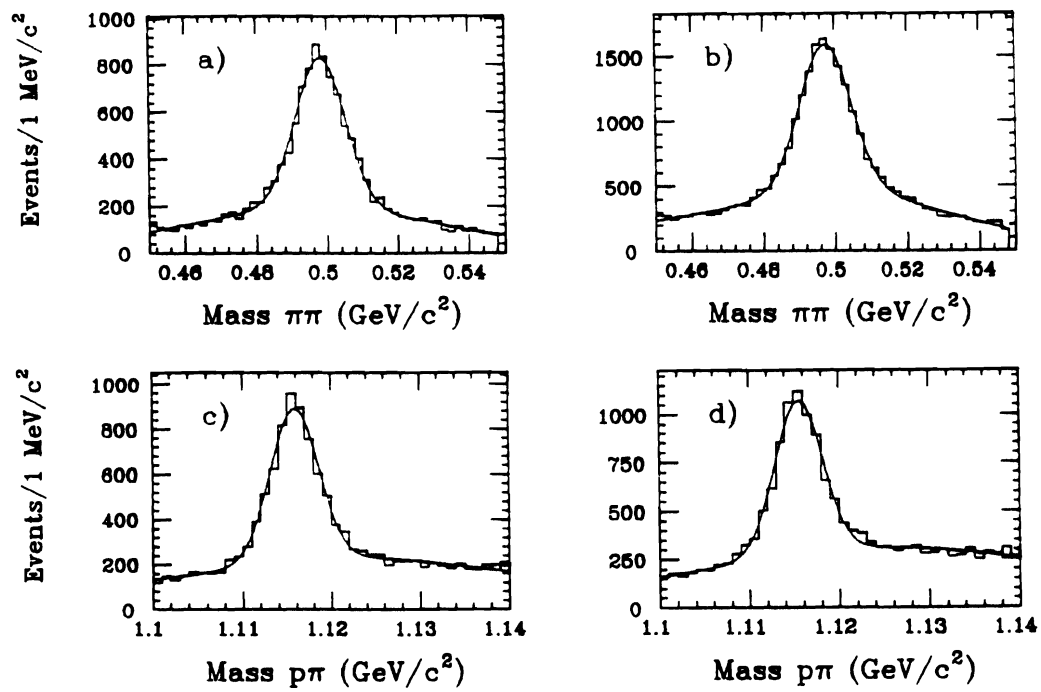

Figure 3.3: Invariant mass distributions for reconstruction vee K^0_s and Λ candidates: a)Reconstruction K^0_s's b) 2 Chamber K^0_s's, c) Reconstruction Λ's, and d) 2 Chamber Λ's. Λ candidates have additional skim requirement cuts described in Sec. 3.6.1.

3.4 Kinks

The term Kink refers to the topology where a charged particle traverses the microstrip system and then decays into a charged particle and a neutral particle. The particles that can be reconstructed from this topology are shown in Table 3.1. The decay region considered for these decays extended from the downstream end of the microstrip system to the first chamber, P0. Unlinked microstrip tracks that pointed into the aperture of M1 and unlinked MWPC tracks not part of a vee candidate were intersected in the X view. Next, the momenta of the parent and charged daughter track were determined using each of the decay hypotheses in listed in Table 3.1. The daughter and parent particle were required to have the same charge and the daughter momentum had to be less than the parent momentum. The X and Z positions of the decay were initially determined by intersecting the microstrip and MWPC tracks in the X projection. For the case of a five-chamber track the momentum of the daughter track was determined from the bend angle in M2 and the Y position of

TABLE 3.1
KINK DECAY TOPOLOGIES

Particle	Decay Modes
π^-	$\mu^-\nu$
K^-	$\mu^-\nu, \pi^-\pi^0$
Σ^+	$p\pi^0, n\pi^+$
Σ^-	$n\pi^-$
Ξ^-	$\pi^-\Lambda^0$
Ω^-	$K^-\Lambda^0$

the decay was determined from the trace of the daughter track. If the decay occurred in the M1 field region, the parent momentum was uniquely determined. If the decay is upstream of the M1 field region, there is a two-fold ambiguity in the parent momentum. If the daughter track was a three-chamber track, then the decay was required to occur in the region upstream of M1. The X and Z coordinates of the decay were then determined from the intersection of the microstrip and MWPC tracks in the X view. The Y coordinate was determined from the microstrip track at this Z location, and the momentum of the daughter track was determined by tracing the track to the decay vertex. Again there is a two-fold ambiguity in the parent momentum.

3.5 Particle Identification

Identification of charged particles was done by several components of the E-687 spectrometer. The Čerenkov system identified charged particles as electrons, pions, kaons, and protons. Muons were identified by both the the Muon system and the HC; electromagnetic particles, electrons and photons, were identified by the electromagnetic calorimetry.

3.5.1 Čerenkov Identification

The first step in the Čerenkov analysis was to determine which cells in each of the counters were "on". A cell was considered "on" if the pulse height exceeded a threshold, typically several pico-coulombs above pedestal. Next the tracks were projected into each of the three counters to determine the relevant cells for each of the tracks. The cells considered were

the one struck by the track and each of the adjacent cells. For each of these cells the light yield, in terms of the number of photoelectrons, was calculated. This yield was based on the results of calibration, momentum of the track, geometric overlap of the Čerenkov cone with the cell, and the hypothesis that the particle was either an electron or pion. If the light yield in any of these cells exceeded the anticipated yield for that cell, then the track was flagged "on" for the counter under consideration. If a second track contributed a significant amount of light to the cell, then the counter was flagged "confused" for the track. If the total light yield in all of the associated cells for a given track was less than half the predicted yield then the counter was flagged "off" for the track. If the counter was neither "off" nor "on" for a track then the counter was called "confused" [35].

Once the response of each counter for a track is determined, a 4-bit particle ID word for each counter is generated based on the counter response and particle momentum. The logical AND of these three ID words is then taken to form the final particle identification, ISTATP, for each track. The possible Čerenkov ID's and momentum ranges are shown in Table 3.2. The nature of the algorithm is such that it favors identifying a track as "light" instead of "heavy".

3.5.2 Muon Identification

Muons were identified using both the Muon system and the Hadron Calorimeter. As a result of the fire, the OM electronics was severely damaged and the efficiency for muon detection in the OM counters was low. The basic algorithm was to project tracks into the muon system and look for corresponding hits, taking into account multiple scattering. For the inner muon system, five of seven planes (3 planes of scintillator, and 4 planes of proptubes) were required to identify the track as a muon candidate. The efficiency for detecting muons in the IM counters was determined from special runs of muons and the results are shown in Table 3.3 [25].

The HC was used to provide additional muon identification. Charged particle tracks were extrapolated to the HC and the hit pattern and pulse height for towers along the projected track were analyzed for being consistent with a muon. The efficiency for detecting muons was determined to be 84% for muons traversing the HC [36] by looking at a sample of $J/\psi \rightarrow \mu^+\mu^-$ events.

TABLE 3.2
ČERENKOV PARTICLE IDENTIFICATION CODES

ISTATP	Identification	Momentum Range (GeV/c)
0	Inconsistent	> 0.0
1	e definite	0.0-17.4
2	π definite	4.5-17.4
3	e,π ambiguous	4.5-61.7
4	K definite	16.0-44.5
6	π,K ambiguous	16.0-17.4
7	e,π, K ambiguous	16.0-44.5, 61.7-117.4
8	p definite	16.0-44.5, 61.7-117.4
12	K,p ambiguous	4.5-61.7
14	π,K,p ambiguous	0.0-17.4
15	confused	> 0.0
4,6,12	K consistent	4.5-61.7
4,6,7,12	K consistent	4.5-117.4
8,12	p consistent	4.5-117.4

3.5.3 Electromagnetic Calorimetry

The Inner and Outer Electromagnetic Calorimeters provided additional identification of electrons. The analysis projected charged particle tracks into the calorimeters and the shower was then reconstructed. The ratio of the observed energy to momentum as determined by the tracking system was required to be greater then 0.8. The efficiency for identifying electrons in the OE was estimated to be greater then 90% [37, 38].

3.6 Skimming

In order to reduce the data set to a workable size, two skims were used. The two skims followed the same basic algorithm. A series of subskims tested each event to see if the requirements of the subskim were met. If the event passed the subskim requirements, a flag was set. The subskims were grouped into different streams, four for SKIM 1 and five for SKIM 2. If an event was selected by any of the subskims for a stream, the event was written out to a file for that stream. In this arrangement a single event could be selected for more then one stream if the appropriate criteria were met. All interspill information was written

TABLE 3.3
AVERAGE MUON EFFICIENCY FOR INNER MUON COUNTER

Detector	Efficiency (%)
IM1V	99.76
IM1H	99.86
IM2H	99.82
IM1X	85.76
IM1Y	85.08
IM2X	81.40
IM2Y	82.55

out to all of the streams.

In addition to the subskimming in SKIM 2, it was found necessary to correct for certain "features" of PASS 1. The reanalysis included Vees, Kinks, muon, and IE analysis. These analyses were completed prior to the testing of the event by the subskim routines.

For SKIM 2 the following subskims were implemented:

- Stream 1
  - Global Vertex Skim.
  - Double Charm Skim.
- Stream 2
  - Charm Meson Skim using the constrained-vertex algorithm with all linked tracks in secondary vertex.
  - Charm Meson Skim using constrained-vertex algorithm allowing for unlinked tracks in secondary vertex.
- Stream 3
  - Semileptonic decays of charm mesons.
  - Semileptonic decays of charm mesons using recovery routine for unlinked tracks.
  - Charm meson to K(nπ).

- Dimuon events.

- Stream 4

  - $\Lambda_c^+ \rightarrow pK^-\pi^+$ using constrained vertex algorithm.
  - Events containing Λ's placing Čerenkov cuts on the proton track.
  - Events containing Kinks.
  - $\Lambda_c \rightarrow$ all charged final states using constrained-vertex algorithm.

- Stream 5

  - e^+e^- pair skim for cross section normalization.
  - Diffractive event skim.

For the analysis reported in this dissertation, events passing the Λ, and $\Lambda_c^+ \rightarrow pK^-\pi^+$ subskims were used.

3.6.1 Λ Subskim

The selection of Λ events was based on the category of the vee and Čerenkov identification of the tracks composing the vee. The first requirement was that the $p\pi^-$ invariant mass of the vee be in the range of 1.10 GeV/c^2 to 1.16 GeV/c^2. No additional cuts were placed on either the Reconstruction Vees, or MICVEES. The following cuts were placed on selected categories of M1 vees:

- For Track-Track vees, the DCA of the two tracks at the vee vertex was required to be less then 5.0 mm.
- For Track-Track vees, the slow track of vees failing the fit was required not to be electron definite, ISTATP=1, or inconsistent, ISTATP=0.
- For Stub-Stub vees, the slow track of vees failing the refit was required not to be electron definite, ISTATP=1, or inconsistent, ISTATP=0.

The Čerenkov analysis was rerun on the tracks comprising the vee candidate using the track momenta from the vee fit. The following Čerenkov cuts were then placed on the fast track of the M1 and SSD vees.

- If $P_{fast} < 20$ GeV/c, ISTATP$_{fast}$=8,12,14.
- If 20 GeV/c $\leq P_{fast} \leq 110$ GeV/c, ISTATP$_{fast}$=8,12.
- If 110 GeV/c $\leq P_{fast}$, ISTATP$_{fast}$=8,12,14,15.

If a vee candidate in the event passed the above requirements, the event was selected by the subskim to be written out to the appropriate stream. A total of 930 thousand events was selected by this subskim as containing a Λ candidate.

3.6.2 $\Lambda_c^+ \rightarrow pK^-\pi^+$ Subskim

Events were chosen for the $\Lambda_c^+ \rightarrow pK^-\pi^+$ subskim if the following criteria were met for three charged tracks in the event:

- One track proton consistent, ISTATP=8,12.
- One track kaon consistent, ISTATP=4,12,7 (P > 60.0 GeV/c).
- One track pion consistent, ISTATP=2,3,7,13,14,15
- Proton and Kaon tracks must have opposite sign charges
- Proton and Pion tracks must have the same sign charge.
- The candidate-driven vertex algorithm returned primary and secondary vertices using the three selected tracks, with the secondary vertex downstream of the primary vertex and a significance of detachment, $L/\sigma_L > 1.0$.
- The invariant mass of the $pK^-\pi^+$ combination was in the range 1.8 to 2.8 GeV/c^2.

This set of requirements selected approximately 1.2 million events for additional analysis.

CHAPTER 4

DATA ANALYSIS

4.1 Analysis of the $pK^-\pi^+$ Sample

The $pK^-\pi^+$ decay mode is the strongest Λ_c^+ signal seen by E-687. The three charged tracks allow for good decay vertex determination, and the presence of two heavy decay products, a proton and a kaon, provides an additional tool in reducing the combinatoric background. The yield in the $pK^-\pi^+$ decay mode may then be used to determine the relative strength of the $\Lambda\pi^+\pi^+\pi^-$ signal. Of special interest are the contributions of two 2-body resonances, $\Delta^{++}K^-$ and $p\overline{K^{*0}}$, which are observed in the $pK^-\pi^+$ final state. Both of these decay topologies occur through both the W-exchange and W-emission process.

4.1.1 $pK^-\pi^+$ Analysis Cuts

Analysis of the $pK^-\pi^+$ decay mode started with the event selection criteria of the $pK^-\pi^+$ subskim described in section 3.6.2. Several additional requirements were added to extract the signal used for the different branching ratio analyses. The selection criteria can be divided into two categories: track selection and vertexing. The track selection cuts were designed to select high quality tracks consistent with origination from a $\Lambda_c^+ \rightarrow pK^-\pi^+$ decay. Tracks from pair conversion, which have very small angles with respect to the beam direction, were rejected by requiring the slopes of the track, x' and y', to be greater than 0.1mrad at the target. The track selection criteria employed in addition to the $pK^-\pi^+$ skim requirements were:

- $\chi^2/\mathrm{DOF} \leq 3.0$ for each candidate track.
- x' and $y' \geq 0.1$ mrad at the target for each of the candidate tracks.

- Only one track allowed to be K/p ambiguous: ISTATP=12.

Combinations of three tracks passing the track selection criteria were then analyzed using the constrained vertex algorithm, DVERT, to determine the position of the primary and secondary vertices, the separation between the vertices, and the errors associated with each quantity. The primary vertex was required to contain at least two charged tracks in addition to the Λ_c^+ candidate to insure a well defined primary vertex independent of the Λ_c^+ candidate. The fit of the secondary vertex was required to have a confidence level greater than 0.01. This requirement rejected candidates that formed a poor vertex, or failed the vertex fit all together. In order to reject candidate combinations where one of the tracks in the secondary vertex was consistent with originating at the primary vertex, each of the tracks in the secondary vertex was required to have a distance of closest approach, DCA, to the secondary vertex, less than its DCA to the primary vertex. The DCA for the primary and secondary vertices was measured in the transverse plane.

To remove high mass, low momentum combinatoric background, a cut on the angles, θ, of the tracks in the Λ_c^+ center of mass frame relative to the Λ_c^+ momentum vector in the laboratory was made. For a spin 1/2 particle, the angular distribution of the decay particles is flat in $\cos\theta$. The angular distributions for the tracks before the angular cut was applied are shown in Fig. 4.1 for both Monte Carlo and data. For $L/\sigma_L \geq 3.0$, the combined cuts, $\cos\theta_p > -0.9$, and $\cos\theta_K < -0.9$, rejected approximately 27% of the $pK^-\pi^+$ candidates in data, while retaining approximately 92% of the $\Lambda_c^+ \rightarrow pK^-\pi^+$ signal based on Monte Carlo studies.

To summarize, the following vertexing requirements were placed on the candidate:

- DVERT ran successfully, and found a primary vertex in the target region.
- There were at least two charged tracks forming the primary vertex in addition to the Λ_c^+ candidate.
- The confidence level of the secondary vertex fit was ≥ 0.01.

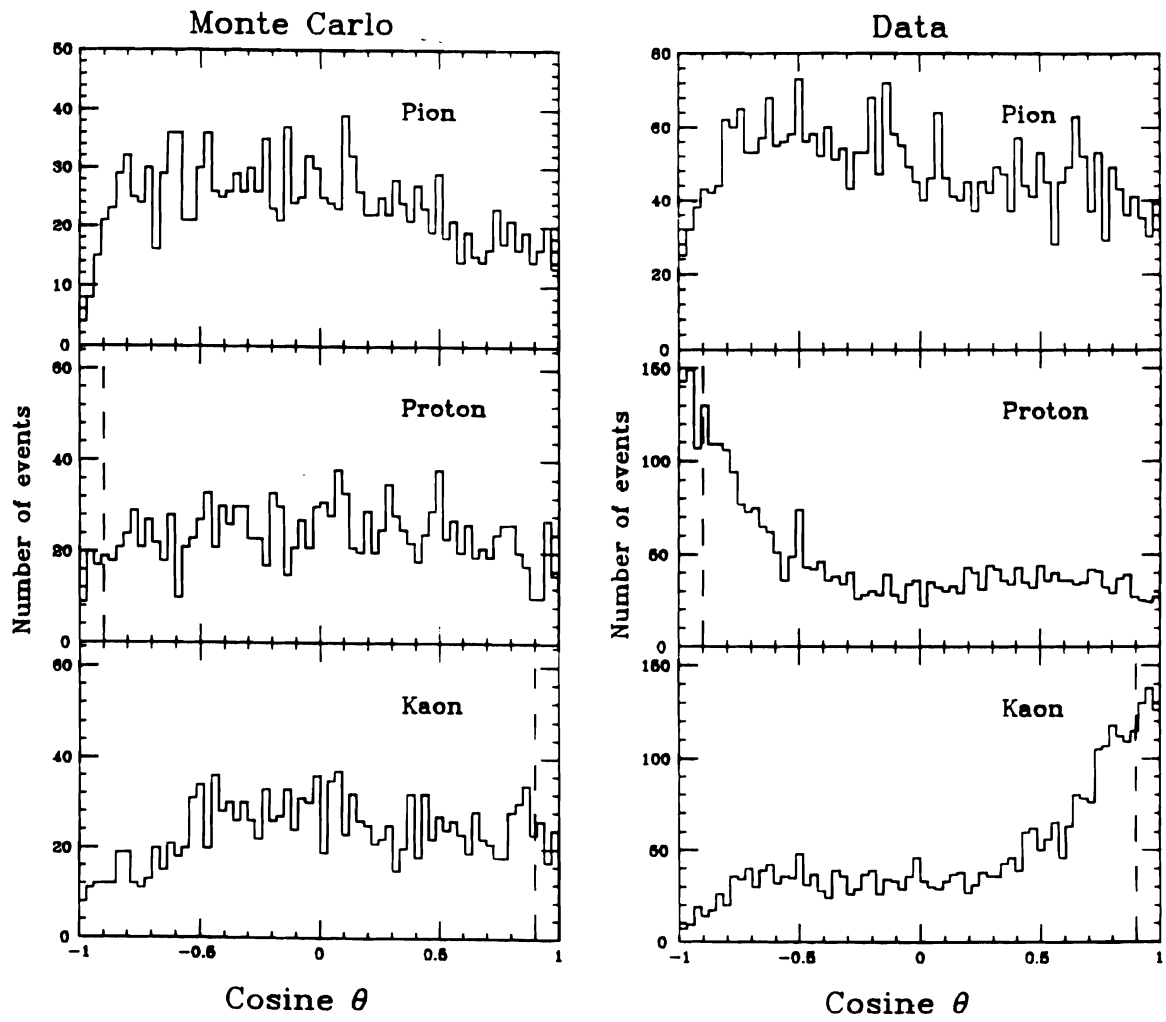

Figure 4.1: Angular decay distributions of $pK^-\pi^+$ candidate tracks for Monte Carlo and data. The dashed lines indicate the where the cuts were applied for the proton and kaon candidates.

- Each of the track candidates had a distance of closest approach, DCA, to the secondary vertex less than its DCA to the primary vertex as measured in the transverse plane.

- The cosine of the angle, θ, between the track in the Λ_c^+ center of mass frame, and the Λ_c^+ momentum vector in the laboratory was required to be greater than -0.9 for the proton, and less than 0.9 for the kaon.

A powerful tool in isolating charm decays is the observation of a secondary decay vertex well separated from the primary production vertex and pointing back to the primary vertex. For the original $pK^-\pi^+$ sample with $L/\sigma_L \geq 1.0$, the vertex distributions for the primary and secondary vertices are shown in Fig. 4.2. Mean vertex resolutions can be estimated from

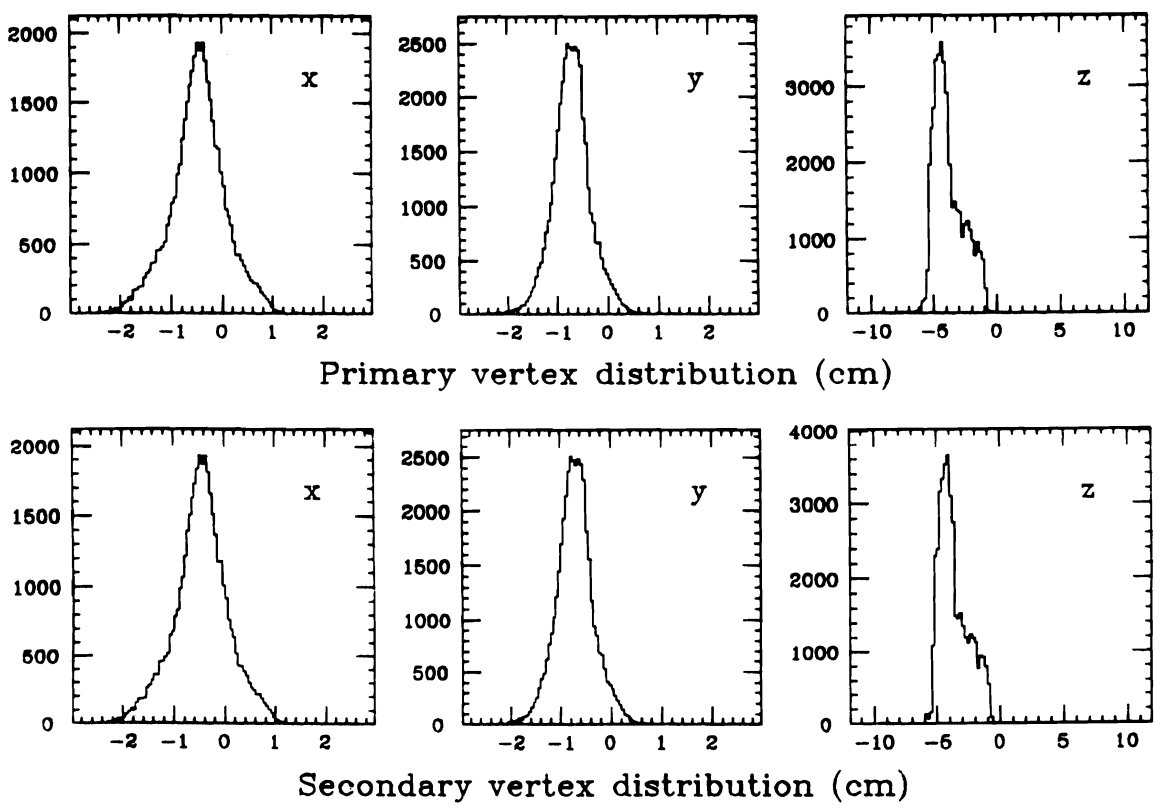

Figure 4.2: Primary and secondary vertex distributions for $pK^-\pi^+$ candidates with $L/\sigma_L \geq 1.0$.

the means of the vertex error distributions shown in Fig. 4.3 and are given in Table 4.1. The vertex errors used in the analysis are determined on a candidate by candidate basis

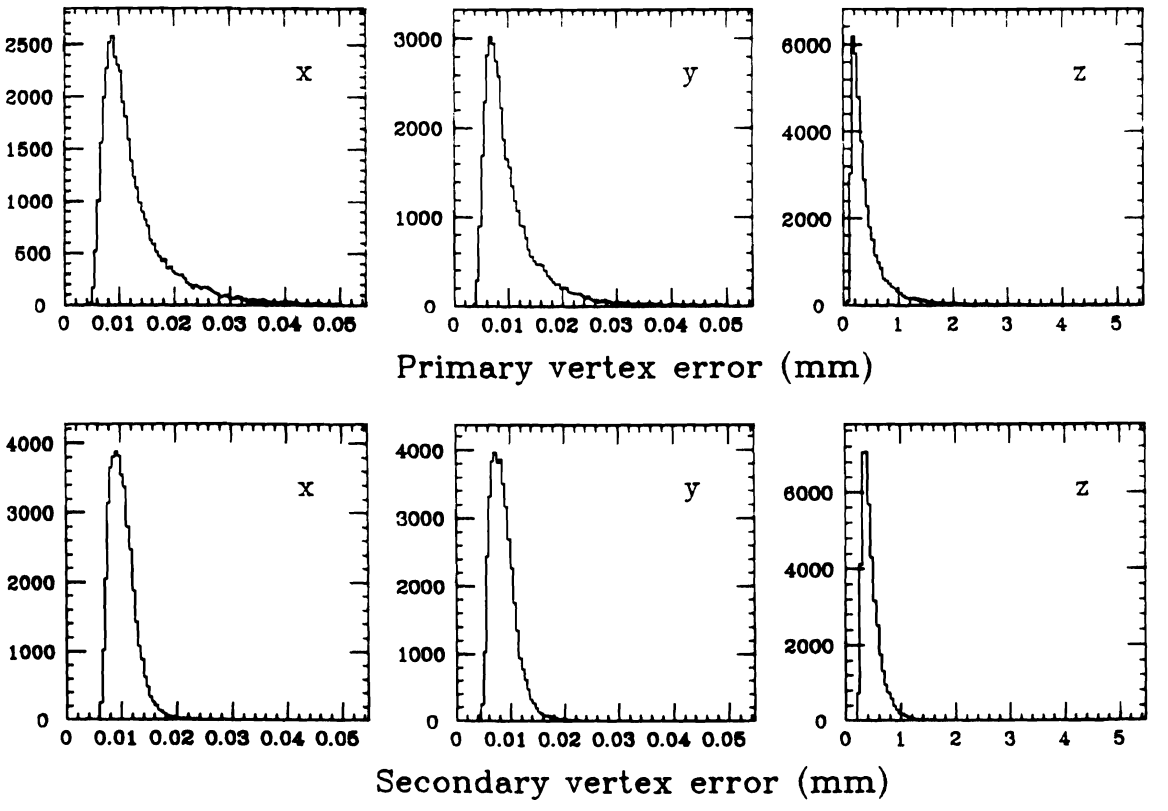

Figure 4.3: Primary and secondary vertex error distributions for $pK^-\pi^+$ candidates with $L/\sigma_L \geq 1.0$.

and include corrections for multiple Coulomb scattering. For the $pK^-\pi^+$ candidates with $L/\sigma_L \geq 1.0$, distributions of the vertex separation, L, error in separation, σ_L, and the significance of detachment, L/σ_L, are shown in Fig. 4.4. The vertex separation distance and errors were determined on a candidate by candidate basis.

The $pK^-\pi^+$ mass distributions for candidates in the final sample are shown in Fig. 4.5 for several values of the L/σ_L cut. The distributions were fit with a Gaussian signal and linear background. The signals were integrated over a mass range of $\pm 3\sigma$ of the nominal Λ_c^+ mass, 2.285 GeV/c^2 to determine the yield . The results for the fits are shown in Table 4.2.

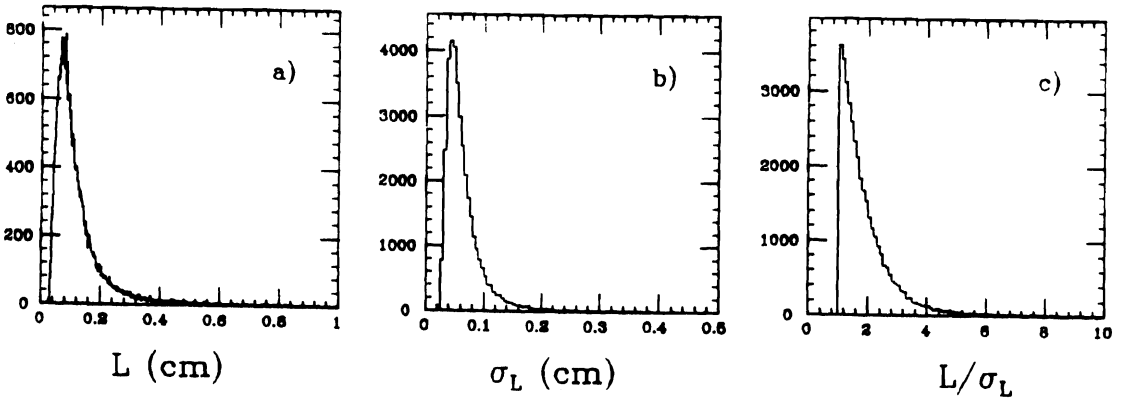

Figure 4.4: Vertex separation quantities for $pK^-\pi^+$ candidates with $L/\sigma_L \geq 1.0$: a) Vertex Separation distance, b) error in separation, and c) significance of detachment.

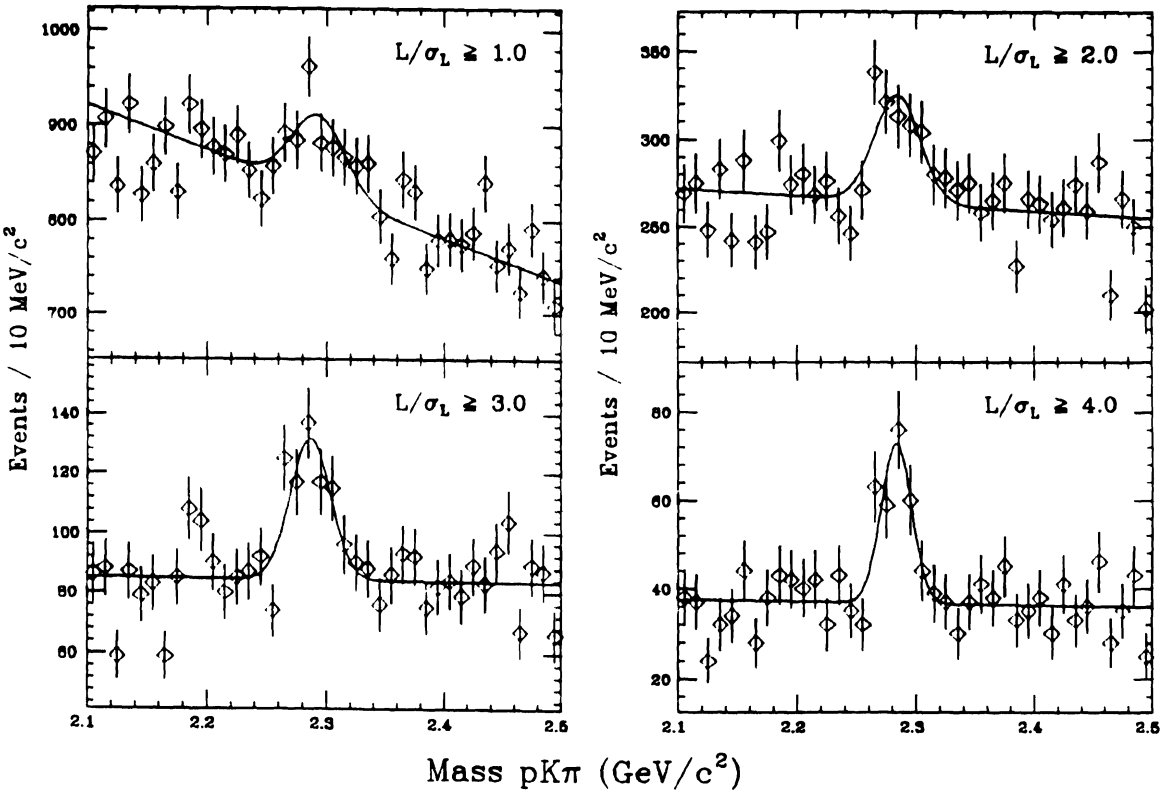

Figure 4.5: $pK^-\pi^+$ mass distributions for several values of the L/σ_L cut.

TABLE 4.1
MEAN VERTEX ERRORS FOR PRIMARY AND SECONDARY VERTICES FOR $pK^-\pi^+$ CANDIDATES

Vertex	x	y	z
Primary	$14.0\mu m$	$11.7\mu m$	$536.9\mu m$
Secondary	$10.4\mu m$	$8.7\mu m$	$426.1\mu m$

TABLE 4.2
FIT RESULTS FOR $pK^-\pi^+$ MASS DISTRIBUTIONS FOR DIFFERENT VALUES OF THE L/σ_L CUT

L/σ_L	Mass (MeV/c^2)	Sigma (MeV/c^2)	Yield	S/N	C.L.
≥ 1.0	2293 ± 6	22 ± 4	447 ± 84	0.14	0.27
≥ 2.0	2284 ± 4	19 ± 3	291 ± 46	0.10	0.33
≥ 3.0	2287 ± 3	16 ± 3	198 ± 39	0.20	0.54
≥ 4.0	2283 ± 3	12 ± 2	114 ± 22	0.26	0.65

4.1.2 Misidentification Studies

A study was made for possible misidentification of kaons as protons in the $pK^-\pi^+$ sample. The proton candidate was reassigned the kaon mass and the K^+K^- and $K^+K^-\pi^+$ invariant masses were calculated. The resulting K^+K^- mass distribution for all $pK^-\pi^+$ combinations with an $L/\sigma_L \geq 3.0$ is shown in Fig. 4.6 a). A clear ϕ peak is seen in the mass spectrum. The $K^+K^-\pi^+$ mass distributions for all $pK^-\pi^+$ candidates with an $L/\sigma_L \geq 7.0$ and $L/\sigma_L \geq 9.0$ are shown Fig. 4.6 b) and c) respectively. There is evidence for enhancements at both the D^+ and D_s^+ mass in both $K^+K^-\pi^+$ mass distributions. The K^+K^- and $K^+K^-\pi^+$ mass distributions for $pK^-\pi^+$ candidates in the mass range 2.260 $GeV/c^2 \leq M(pK\pi) \leq$ 2.320 GeV/c^2 are shown in Fig. 4.7. Evidence for ϕ, D^+, and D_s^+ peaks is still seen.

A sample of 100,000 $pK^-\pi^+$ Monte Carlo events was used to study the reflection of the true $pK^-\pi^+$ events into the K^+K^- and $K^+K^-\pi^+$ mass spectrum. The proton was reassigned the kaon mass and the K^+K^- and $K^+K^-\pi^+$ invariant masses were calculated. The resulting mass distributions are shown in Fig. 4.8. The mass plots show a smooth

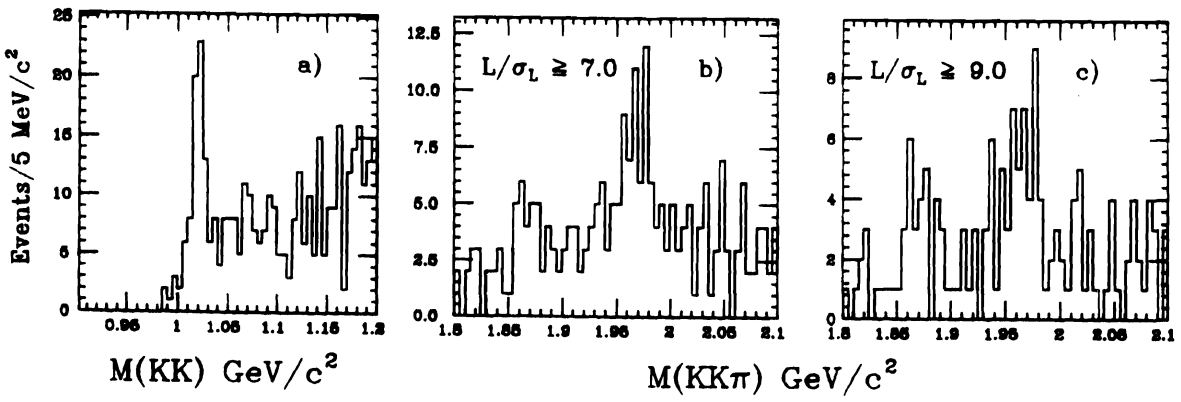

Figure 4.6: Proton misidentification mass distributions for all $pK^-\pi^+$ candidates: a) K^+K^- mass distribution for candidates with $L/\sigma_L \geq 3.0$, b) $K^+K^-\pi^+$ mass distributions for candidates with $L/\sigma_L \geq 7.0$, and c) $K^+K^-\pi^+$ mass distributions for candidates with $L/\sigma_L \geq 9.0$.

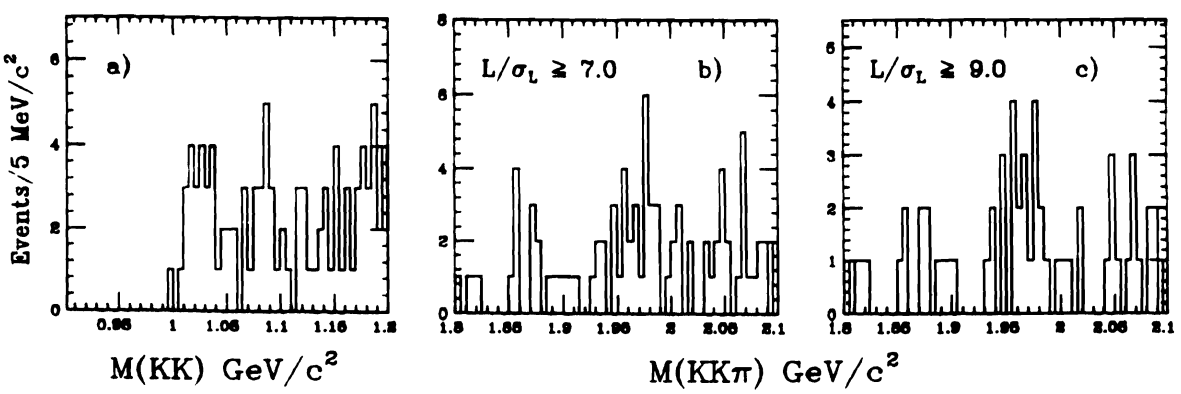

Figure 4.7: Proton misidentification mass distributions for $pK^-\pi^+$ candidates in the mass range 2.260 $GeV/c^2 \leq M(pK^-\pi^+) \leq 2.310$ GeV/c^2: a) K^+K^- mass distribution for candidates with $L/\sigma_L \geq 3.0$, b) $K^+K^-\pi^+$ mass distributions for candidates with $L/\sigma_L \geq 7.0$., and c) $K^+K^-\pi^+$ mass distributions for candidates with $L/\sigma_L \geq 9.0$.

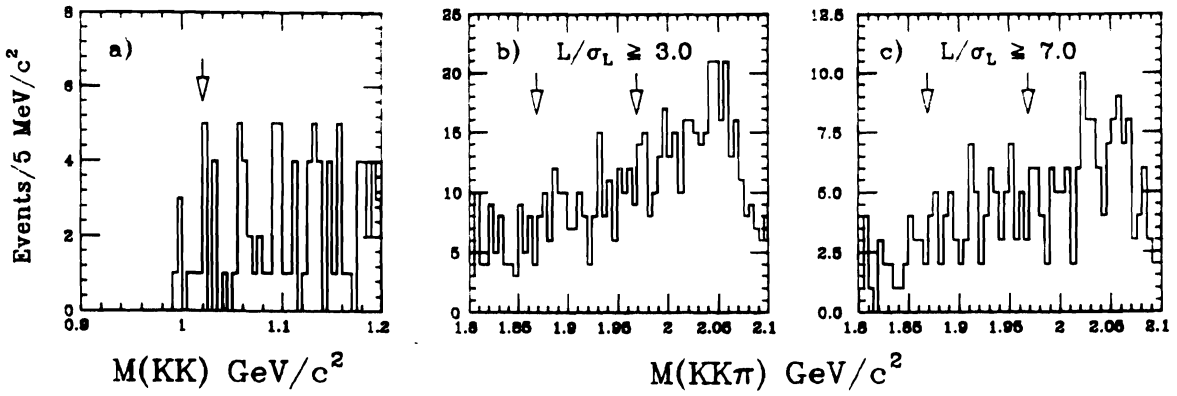

Figure 4.8: Mass distributions for the reflection of Monte Carlo $pK^-\pi^+$ events into the K^+K^- and $K^+K^-\pi^+$ mass distributions: a) K^+K^- mass distribution, arrow indicates ϕ mass, 1.04 GeV/c^2, b) $K^+K^-\pi^+$ mass distribution for $L/\sigma_L \geq 3.0$, and c) $K^+K^-\pi^+$ mass distribution for $L/\sigma_L \geq 7.0$. Arrows indicate the D^+ mass, 1.869 GeV/c^2, and the D_s^+ mass, 1.969 Gev/c^2 for b) and c).

distribution of masses with no evidence for ϕ, D^+, or D_s^+ enhancements.

A sample of 15,000 D^+ and D_s^+ Monte Carlo events decaying to the $K^+K^-\pi^+$ non-resonant final state was used to study the reflection of the D^+ and D_s^+ into the $pK^-\pi^+$ mass spectrum. The kaon with the same sign as the pion was reassigned proton mass and the $pK^-\pi^+$ invariant mass was calculated. The resulting mass distributions for D^+, and D_s^+ decays with an $L/\sigma_L \geq 7.0$ are shown in Fig. 4.9. For neither $D^+ \rightarrow K^+K^-\pi^+$ nor $D_s^+ \rightarrow K^+K^-\pi^+$ nonresonant decays is there evidence of an enhancement in the $pK^-\pi^+$ mass spectrum in the Λ_c^+ mass region.

Based on this study, the effects on the $pK^-\pi^+$ data sample of three additional cuts designed to remove background resulting from the misassignment of a kaon as a proton were analyzed. The proton candidate was assigned the kaon mass and the following cuts were applied:

- K^+K^- mass greater than the ϕ mass, $M(KK) > 1.04\ GeV/c^2$.
- $K^+K^-\pi^+$ mass outside the D^+ mass region,
  $1.855\ GeV/c^2 \leq M(KK\pi) \leq 1.885\ GeV/c^2$.
- $K^+K^-\pi^+$ mass outside the D_s^+ mass region,
  $1.950\ GeV/c^2 \leq M(KK\pi) \leq 1.985\ GeV/c^2$,

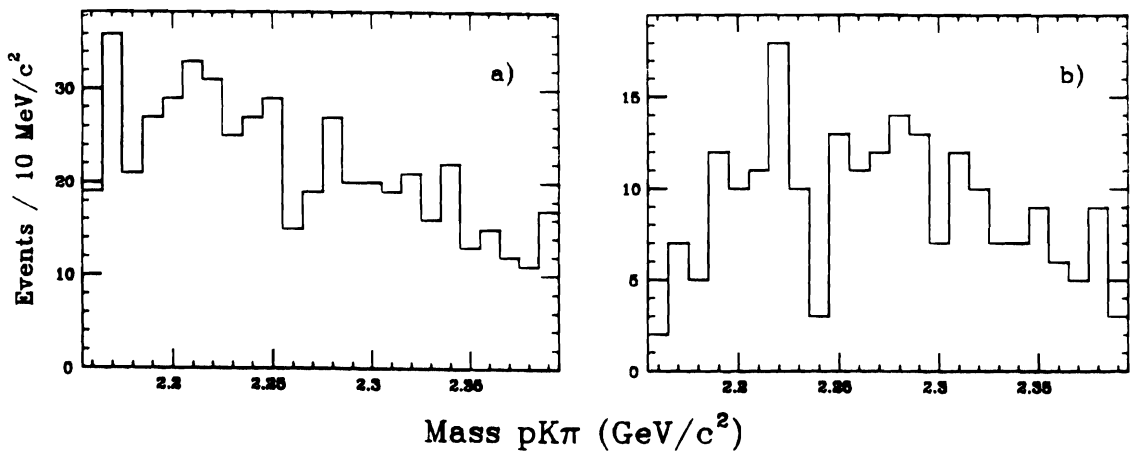

Figure 4.9: Mass distributions for the reflection of Monte Carlo D^+ and D_s^+ events into the $pK^-\pi^+$ mass distribution. The kaon with the same sign as the pion is assigned proton mass.

The $pK^-\pi^+$ mass distributions for $L/\sigma_L \geq 3.0$ with the mass cuts applied separately and then together are shown in Fig. 4.10. The results of fitting the distributions with a Gaussian signal and linear background are given in Table 4.3. From Monte Carlo studies it was estimated that the D^+ mass cut would reject $(6 \pm 1)\%$ and the D_s^+ mass cut would reject $(11 \pm 1)\%$ of the true $\Lambda_c^+ \rightarrow pK^-\pi^+$ signal for this L/σ_L cut. Based on the yields from fits to data, the D^+ and D_s^+ mass cuts reduced the Λ_c^+ signal by $(11 \pm 3)\%$, and $(16 \pm 5)\%$ respectively. The ϕ mass cut was estimated to reject less than 1% of the true $pK^-\pi^+$ signal; $(3 \pm 2)\%$ of the signal was rejected based on the fit to data.

TABLE 4.3
$pK^-\pi^+$ FIT RESULTS FOR DIFFERENT KAON MISIDENTIFICATION CUTS ($L/\sigma_L \geq 3.0$)

Cut	Mass (MeV/c^2)	Sigma (MeV/c^2)	Yield	S/N	C.L.
≥ 3.0	2287 ± 3	16 ± 3	198 ± 39	0.20	0.54
ϕ	2288 ± 4	17 ± 3	195 ± 40	0.24	0.53
D^+	2286 ± 3	17 ± 3	185 ± 39	0.23	0.38
D_s^+	2288 ± 4	18 ± 4	175 ± 37	0.23	0.48
ϕ, D^+, D_s^+	2288 ± 3	18 ± 4	165 ± 38	0.20	0.34

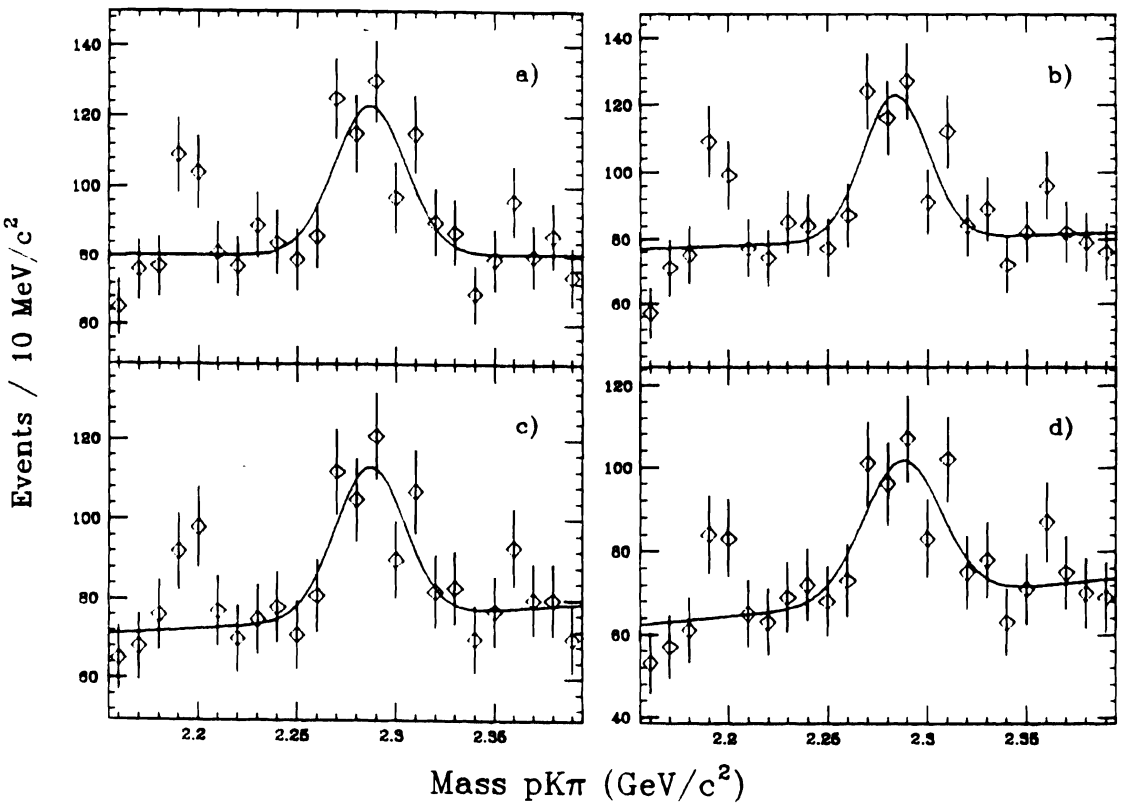

Figure 4.10: $pK^-\pi^+$ mass distributions for $L/\sigma_L \geq 3.0$ after misidentification mass cuts: a) Cut on ϕ mass, $M(KK) > 1.04\ GeV/c^2$, b) Cut on D^+ mass, $1.855 \leq M(KK\pi) \leq 1.885$, c) Cut on D_s^+ mass, $1.950 \leq M(KK\pi) \leq 1.985$, and d) Simultaneous cuts on ϕ, D^+, and D_s^+ masses.

4.2 Analysis of Samples for Decay Modes Including a Λ

Isolating the decay modes of the Λ_c^+ including a Λ provides a greater challenge. For the two-body final state, $\Lambda\pi^+$, the secondary decay vertex is poorly defined since it includes only one charged track. While the decay vertex is better defined for the $\Lambda\pi^+\pi^+\pi^-$ case, the presence of three pions in the final state increases the combinatoric background. The sample of events passing the Λ strip described in Sec. 3.6.1 was searched for specific decay mode candidates. The modes considered were: $\Lambda_c^+ \rightarrow \Lambda\pi^+$, $\Lambda_c^+ \rightarrow \Lambda\pi^+\pi^+\pi^-$, and $\Lambda_c^+ \rightarrow \Lambda K^+K^-\pi^+$. The following selection criteria were used to select events with decay candidates consistent with one of the selected decay modes:

- The event passed the Λ strip described in Sec. 3.6.1.
- The Λ candidate invariant mass was in the range $1.105\ GeV/c^2 \leq M(p\pi^-) \leq 1.125\ GeV/c^2$.
- The Λ candidate had the largest momentum of the candidate particles.
- $\chi^2/\mathrm{DOF} \leq 3.0$ for each of the candidate tracks.
- Each of the PWC candidate tracks was linked to an SSD track.
- The track candidates were not part of the vee candidate.
- The candidate pion tracks were pion consistent; ISTATP=2,3,7,14,15.
- The candidate kaon tracks were kaon consistent; ISTATP=4,12,7($P > 60$ GeV/c).
- The total charge for $\Lambda\pi^+$ and $\Lambda\pi^+\pi^+\pi^-$ combinations was $+1$ for candidates with a Λ and -1 for candidates with a $\overline{\Lambda}$. Total charges ± 1 were retained for the $\Lambda KK\pi$ combinations.
- The invariant mass of the candidate was in the range 2.15 GeV/c^2 to 2.55 GeV/c^2.

This set of selection criteria was used to reduce the data sample for the final analyses of the Λ decay modes. Approximately 209,000 events had at least one combination satisfying the selection requirements.

4.2.1 $\Lambda_c^+ \rightarrow \Lambda\pi^+\pi^+\pi^-$ Analysis

The analysis of the $\Lambda_c^+ \rightarrow \Lambda\pi^+\pi^+\pi^-$ decay mode was based on the constrained vertex algorithm, DVERT, described in section 3.2.2. In addition to the selection requirements described in section 4.2 the following requirements were placed on each of the candidates.

- x' and $y' \geq 0.1$ mrad at the target for each of the candidate tracks.
- The DVERT algorithm ran successfully and a primary vertex was found in the target region.
- There were at least two tracks in the primary vertex in addition to the Λ_c^+ candidate.
- At least two of the pion candidate tracks were pion definite or pion/electron ambiguous, ISTATP=2,3.
- At least two of the pion track candidates had DCAs to the secondary vertex less than their DCAs to the primary vertex as measured in the transverse plane.

This set of selection requirements was chosen to select candidates that were consistent with being a $\Lambda_c^+ \rightarrow \Lambda\pi^+\pi^+\pi^-$ decay and forming a secondary vertex downstream of the primary vertex. In forming the secondary vertex, the Λ candidate was used in finding the vertex position if it was a microstrip region vee. For non-microstrip vees, the secondary vertex location was determined by the three pion tracks, and the Λ contributed only to the magnitude and direction of the candidate-state momentum vector used as a seed for the primary vertex finding. The distributions of the vertex separation, error in the separation, and significance of detachment for all $\Lambda\pi^+\pi^+\pi^-$ candidates are shown in Fig. 4.11. The $\Lambda\pi^+\pi^+\pi^-$ mass distributions for resulting candidates are shown in Fig. 4.12 for several values of the L/σ_L cut. No clear evidence for a Λ_c^+ peak exists in any of the distributions at this stage of the analysis. A minimum energy cut was next applied to the Λ_c^+ candidate, requiring that the Λ_c^+ energy be greater than 60 GeV. A Λ_c^+ signal could than be seen. The resulting mass distributions for several values of the L/σ_L cut are shown in Fig. 4.13. The distributions were fit with a Gaussian signal and linear background; the results are given in Table 4.4.

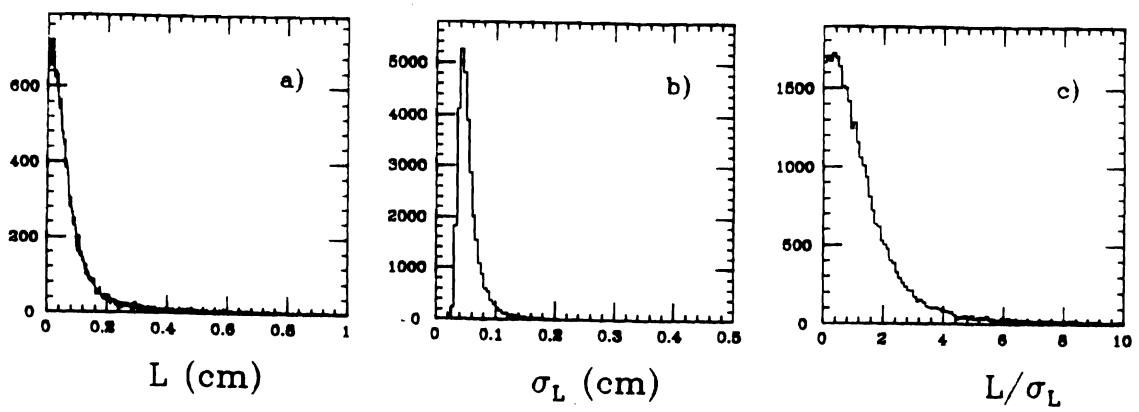

Figure 4.11: Vertex separation quantities for $\Lambda\pi^+\pi^+\pi^-$ candidates: a) separation distance, b) error in separation, and c) significance of detachment.

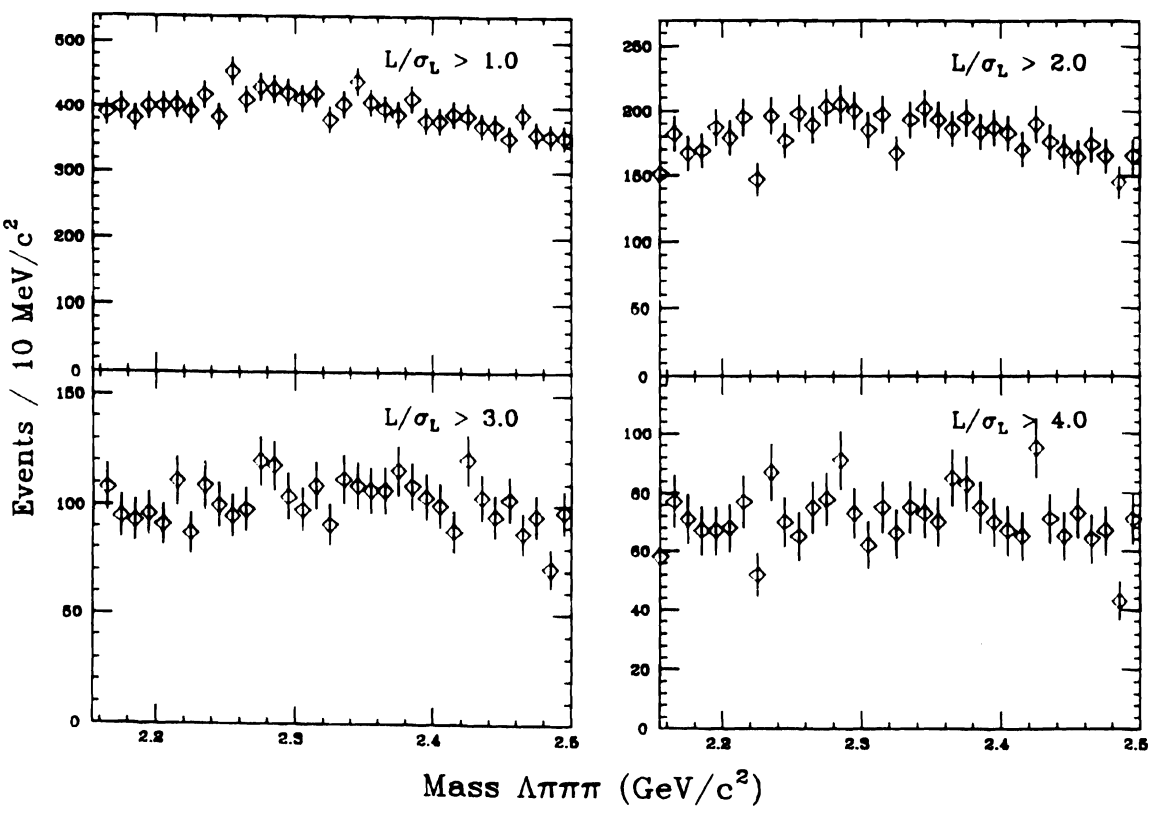

Figure 4.12: $\Lambda\pi^+\pi^+\pi^-$ mass distributions for several values of the L/σ_L cut.

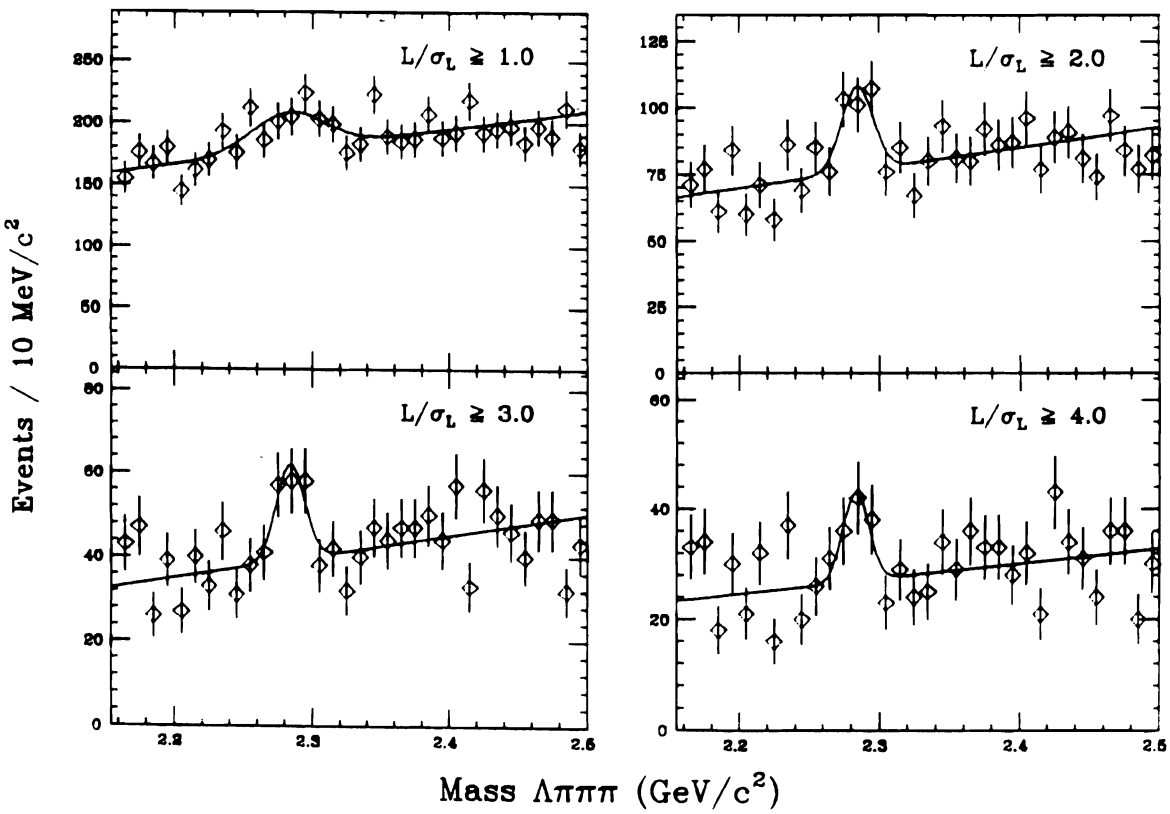

Figure 4.13: $\Lambda\pi^+\pi^+\pi^-$ mass distributions for candidates with $E(\Lambda_c^+) \geq 60\ GeV$ for several values of the L/σ_L cut.

TABLE 4.4
FIT RESULTS FOR $\Lambda\pi^+\pi^+\pi^-$ CANDIDATES WITH A Λ_c^+ ENERGY $\geq 60\ GeV$

L/σ_L	Mass (MeV/c^2)	Sigma (MeV/c^2)	Yield	S/N	C.L.
≥ 1.0	2283 ± 7	27 ± 6	149 ± 40	0.14	0.50
≥ 2.0	2285 ± 3	11 ± 3	87 ± 20	0.19	0.43
≥ 3.0	2284 ± 4	10 ± 3	58 ± 18	0.25	0.16
≥ 4.0	2284 ± 4	9 ± 3	37 ± 12	0.23	0.06

4.2.2 $\Lambda_c^+ \rightarrow \Lambda\pi^+$ Search

A search was made for $\Lambda_c^+ \rightarrow \Lambda\pi^+$ decays using the full Λ sample. The $\Lambda\pi^+$ mass distributions for all combinations and for combinations with the pion identified as pion definite or pion/electron ambiguous, ISTATP=2,3, are shown in Fig. 4.14. The primary and secondary vertices were located using the DVERT algorithm and a detached vertex was searched for. This decay mode provides a more difficult challenge in forming a secondary vertex. Candidates consisting of Λ's from the microstrip region, SSDVEEs and MICVEEs, have two well defined tracks in the secondary vertex, the Λ candidate and the pion track. However the microstrip region vees constitute only about 10% of the total Λ candidates. For other categories of vees, there is only one well defined pion track, plus the poorly defined Λ candidate. The resulting mass distributions for all Λ candidates and for several values of the L/σ_L cut are shown in Fig. 4.15. Additional cuts requiring that the $\Lambda\pi^+$ candidate energy be greater than 60 GeV, and that the pion candidate be pion definite or pion/electron ambiguous, ISTAP=2,3, were also applied. The resulting mass distributions for several values of the L/σ_L cut are shown in Fig. 4.16. There is no strong evidence for a signal in any of the mass distributions.

4.2.3 $\Lambda_c^+ \rightarrow \Lambda K^+K^-\pi^+$ Search

A search was made for the decay $\Lambda_c^+ \rightarrow \Lambda K^+K^-\pi^+$. The reduced phase space, $Q \approx 45\ MeV$, will suppress the decay rate with respect to the $\Lambda\pi^+\pi^+\pi^-$ decay mode. Evidence of a signal for the $\Lambda K^+K^-\pi^+$ decay mode would be provided by the presence of an excess of events at the Λ_c^+ mass in the right-sign, $\Lambda K^+K^-\pi^+$, mass distribution as compared to

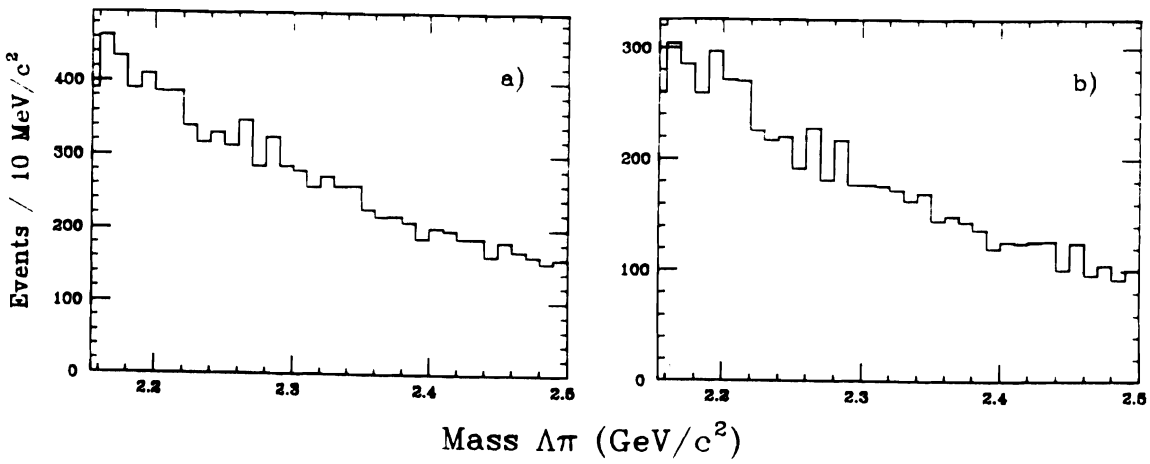

Figure 4.14: $\Lambda\pi$ mass distributions: a) Pion track π consistent, and b) Pion track π definite or e/π ambiguous.

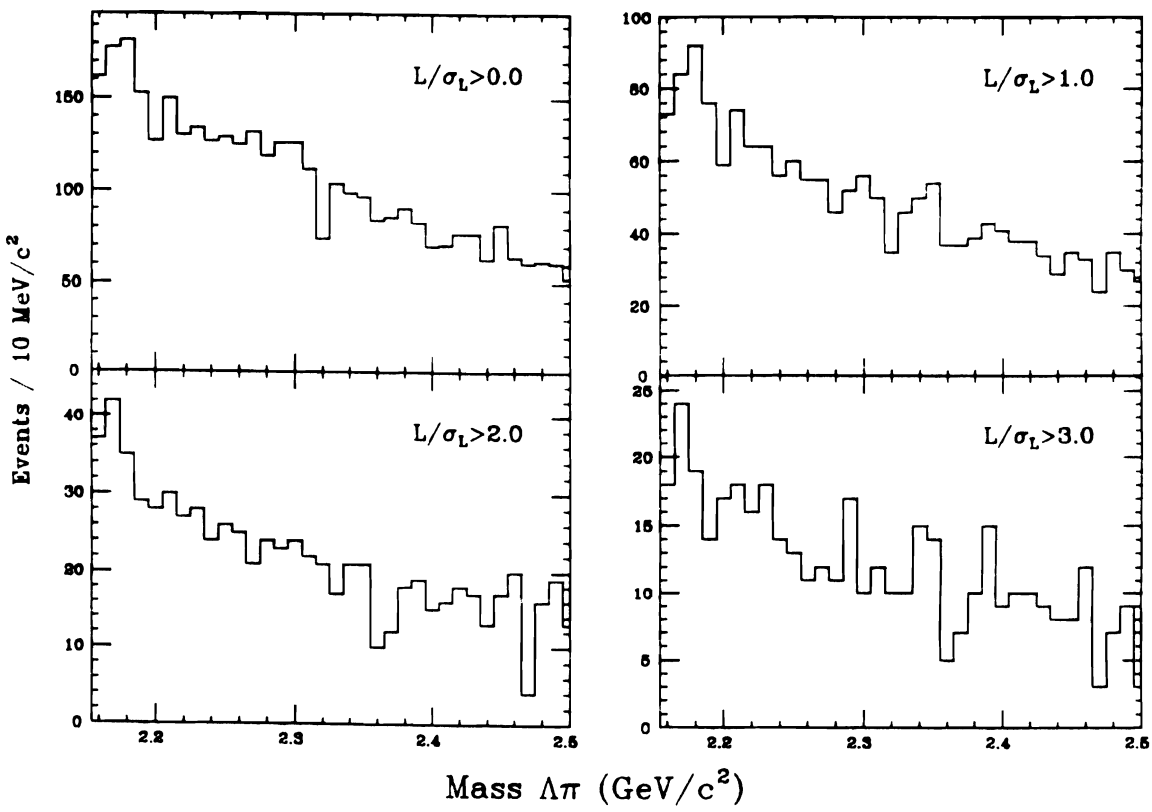

Figure 4.15: $\Lambda\pi$ mass distributions for several values of the L/σ_L cut.

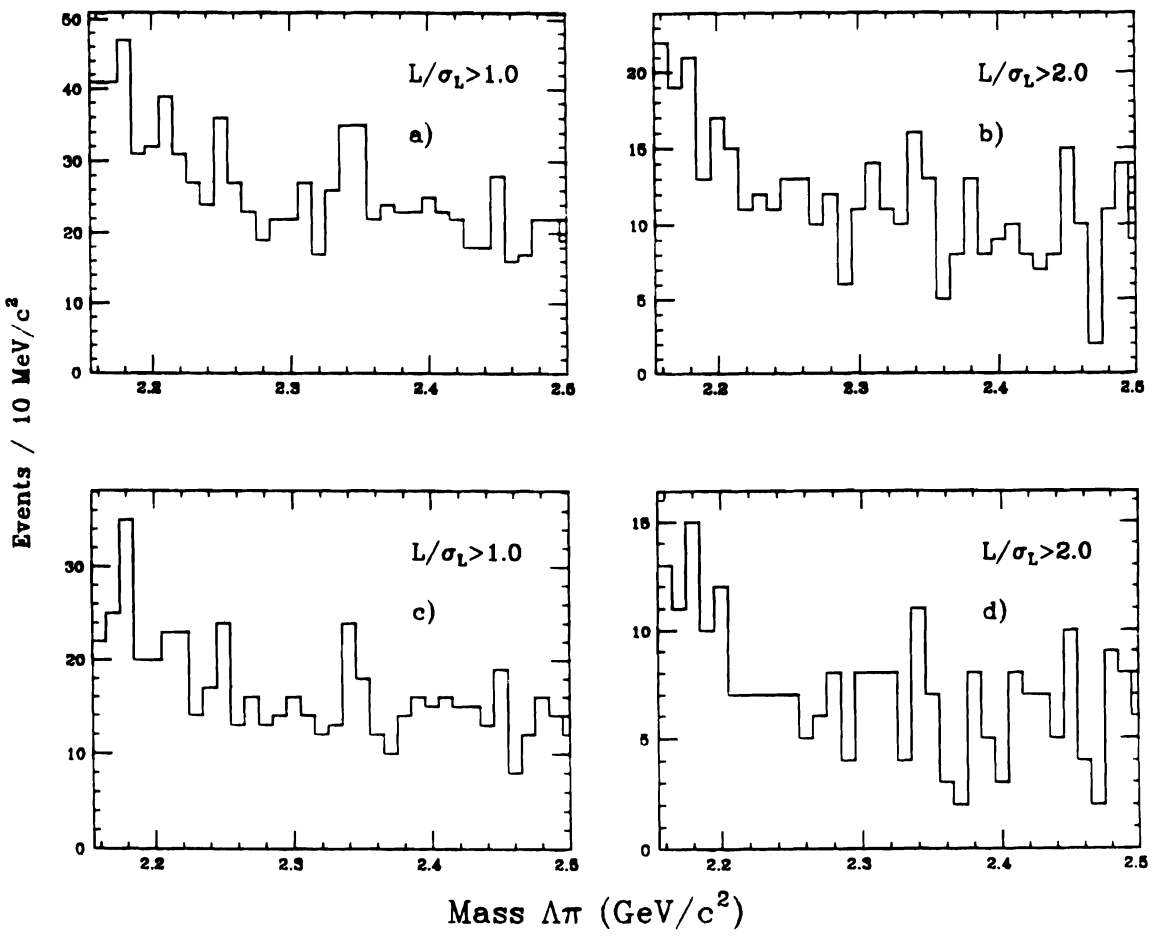

Figure 4.16: $\Lambda\pi$ mass distributions for several values of the L/σ_L cut: a) $E(\Lambda\pi^+) \geq 60\ GeV, L/\sigma_L \geq 2.0$, b) $E(\Lambda\pi^+) \geq 60\ GeV, L/\sigma_L \geq 1.0$, c) Pion track π definite or e/π ambiguous, $L/\sigma_L \geq 2.0$, and d) Pion track π definite or e/π ambiguous, $L/\sigma_L \geq 1.0$.

the wrong-sign, $\Lambda K^+K^-\pi^-$, mass distribution. The mass distributions for the right-sign and wrong-sign combinations are shown in Fig. 4.17. There are very few events below 2.3 GeV/c^2. There is no evidence for a significant excess of right-sign combinations relative to wrong-sign combinations.

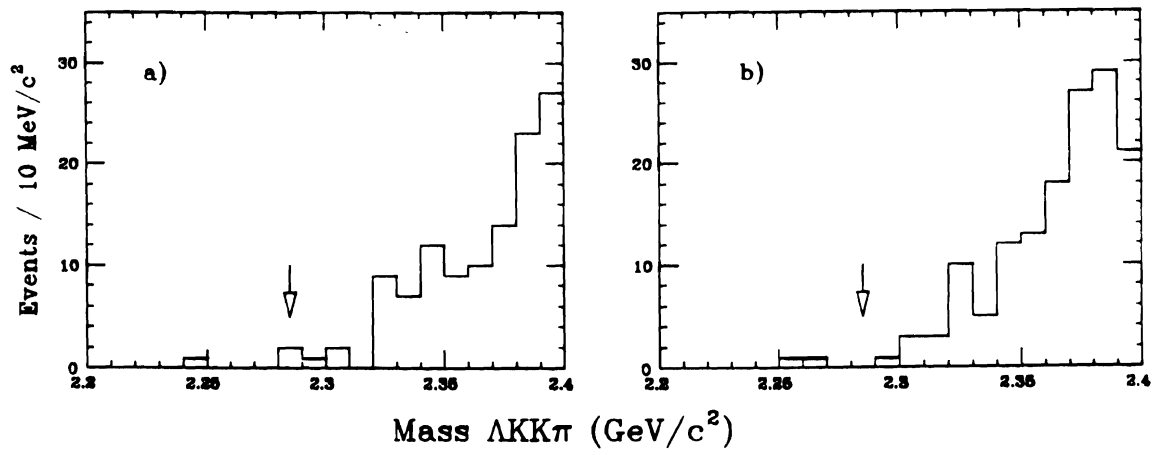

Figure 4.17: $\Lambda KK\pi$ mass distributions: a) Right-sign candidates, and b) Wrong-sign candidates. Arrows indicate the nominal Λ_c^+ mass of 2.285 GeV/c^2.

4.3 Efficiency Measurements

In order to determine relative branching ratios, the geometrical acceptances, detection efficiencies, reconstruction efficiencies and analysis cut efficiencies for the various decay modes must be determined. This was done with Monte Carlo events generated by the E-687 ROGUE Monte Carlo package. A brief description of the ROGUE Monte Carlo package can be found in Appendix A.

4.3.1 Monte Carlo Efficiency Determination

The Monte Carlo efficiency determination for the $pK^-\pi^+$, and $\Lambda\pi^+\pi^+\pi^-$ decay modes was based on two samples of ROGUE Monte Carlo events. The events were generated using the mixed run configuration to simulate the changes in spectrometer efficiencies and target configurations during the run. For the $pK^-\pi^+$ efficiency study, a sample of 100,000

$\gamma p \rightarrow \Lambda_c^+ \; \bar{c}\; meson + C.C,\; \Lambda_c^+ \rightarrow pK^-\pi^+$ events was generated. In this sample, 23% of the $pK^-\pi^+$ decays were via the $\Lambda_c^+ \rightarrow p\overline{K^{*0}},\; \overline{K^{*0}} \rightarrow K^-\pi^+$ channel. Another sample of 170,000 $\gamma p \rightarrow \Lambda_c^+ \; \bar{c}\; meson + C.C,\; \Lambda_c^+ \rightarrow \Lambda\pi^+\pi^+\pi^-,\; \Lambda \rightarrow p\pi^-$ events was used to measure the efficiency for the $\Lambda\pi^+\pi^+\pi^-$ final state. The efficiency for observing each mode with the selected analysis cuts was measured as a function of the generated Λ_c^+ energy.

The procedure for determining the efficiency was identical for both the $pK\pi^+$ and $\Lambda\pi^+\pi^+\pi^-$ modes. The Monte Carlo samples were first reconstructed using the full PASS 1 reconstruction program. The reconstructed Monte Carlo samples were then analyzed using the same analysis routines used to analyze each of the decay modes. The efficiency was measured as a function of the energy of the generated Λ_c^+ candidate in 5 GeV energy bins. The efficiency of successive cuts was defined as the number of events passing a cut divided by the number of events before the cut. The order in which the cuts were applied is:

- The Master Gate was satisfied.
- The Second Level Energy Trigger was satisfied.
- The Λ was reconstructed and identified as a Vee by the Vee analysis package (Λ mode only).
- The Λ passed the Λ strip requirements including the mass constraint on the Λ candidate (Λ mode only).
- Track selection requirements, including geometrical acceptance, track reconstruction, and Čerenkov identification were satisfied.
- Only one track was K/p ambiguous ($pK^-\pi^+$ mode only).
- Invariant mass of the reconstructed tracks was in the mass range $2.150\ GeV/c^2 \leq M(\Lambda_c^+) \leq 2.550\ GeV/c^2$.
- DVERT ran successfully with a primary vertex found in the target region.
- The primary vertex consisted of at least two tracks in addition to the Λ_c^+ candidate.
- The secondary vertex was downstream of the primary vertex.

- The secondary vertex fit confidence level was ≥ 0.01 ($pK^-\pi^+$ mode only).
- The cosine of the angle, θ, between the proton track in the Λ_c^+ center of mass frame, and the Λ_c^+ momentum vector in the laboratory was greater than -0.9 ($pK^-\pi^+$ mode only).
- The cosine of the angle, θ, between the kaon track in the Λ_c^+ center of mass frame, and the Λ_c^+ momentum vector in the laboratory was less than 0.9 ($pK^-\pi^+$ mode only).
- The DCA of each decay track to the secondary vertex was less than its DCA to the primary vertex as measured in the transverse plane.
- $L/\sigma_L \geq 3.0$
- ϕ mass cut ($pK^-\pi^+$ mode only).
- D^+ and D_s^+ mass cuts ($pK^-\pi^+$ mode only).

The efficiencies were determined in 5 GeV energy bins for candidates generated in the energy range 0 to 300 GeV. The efficiencies for successive cuts applied in order are shown in Figs. 4.18 and 4.19 for the $pK^-\pi^+$ and $\Lambda\pi^+\pi^+\pi^-$ decay modes respectively. The final efficiency distributions from Monte Carlo studies for geometrical acceptances, triggering, and the full set of analysis cuts for the $pK^-\pi^+$ and $\Lambda\pi^+\pi^+\pi^-$ modes are shown in Fig. 4.20. For the $pK^-\pi^+$ mode, the efficiency functions including cuts on the ϕ mass cut, and the combined ϕ, D^+, and D_s^+ mass cuts are included. Parametrizations for the efficiencies were determined by fitting the efficiency distributions over the range 60 GeV to 150 GeV. The functional forms were chosen empirically to provide a good description of the efficiency distributions. The functional forms chosen were $A + B/x^3$ for the $pK^-\pi^+$ mode, and $A + Bx + Cx^3$ for the $\Lambda\pi^+\pi^+\pi^-$ mode, where x is the energy of the Λ_c^+ candidate. The results of the fits and the values for the parameters are given in Table 4.5.

4.3.2 Corrections to the Monte Carlo Efficiencies

The efficiency determination discussed in the last section assumes that the ROGUE Monte Carlo correctly simulates the physical properties of production and decay, and all aspects

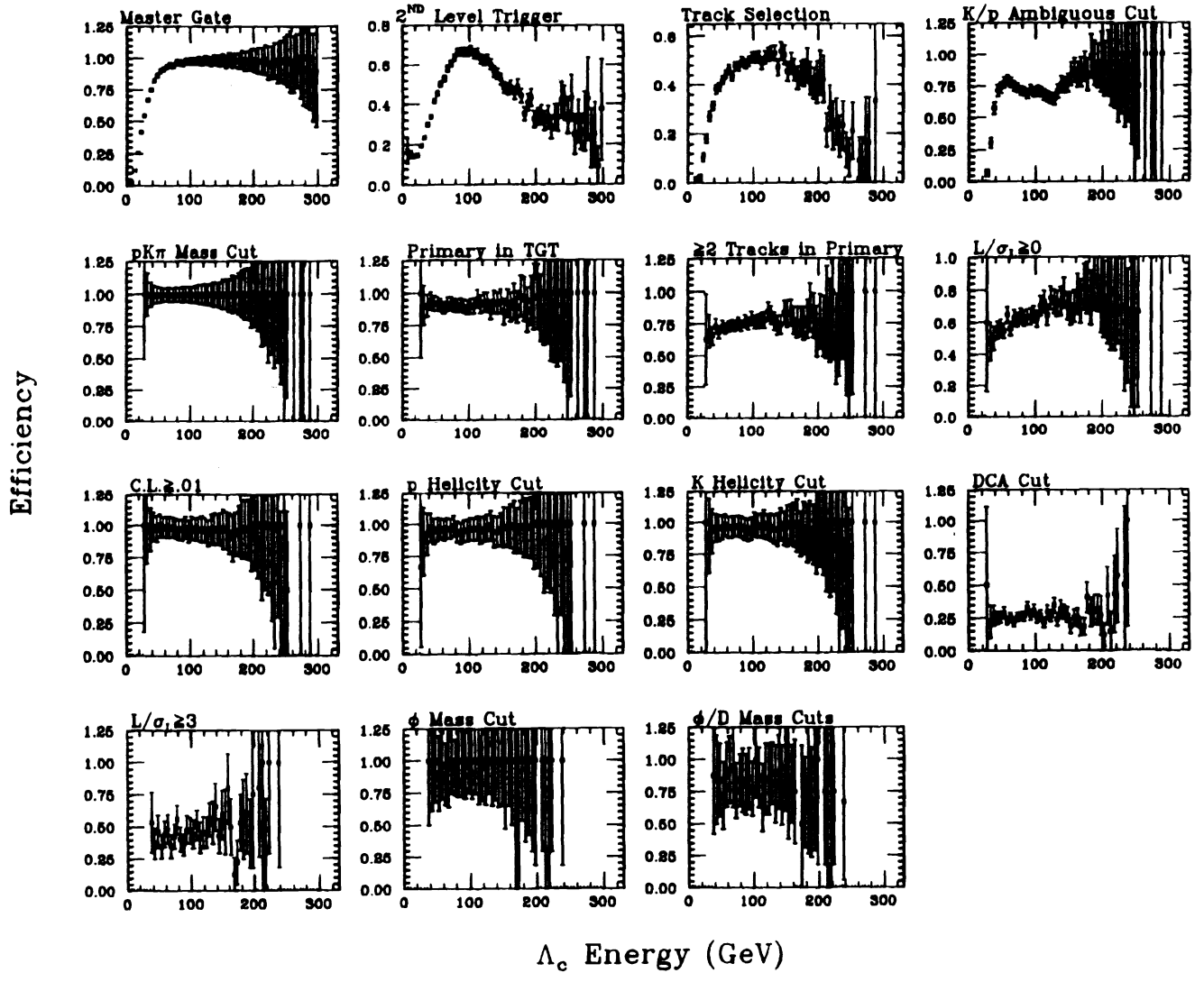

Figure 4.18: Efficiencies for successive cuts used in the $pK^-\pi^+$ analysis.

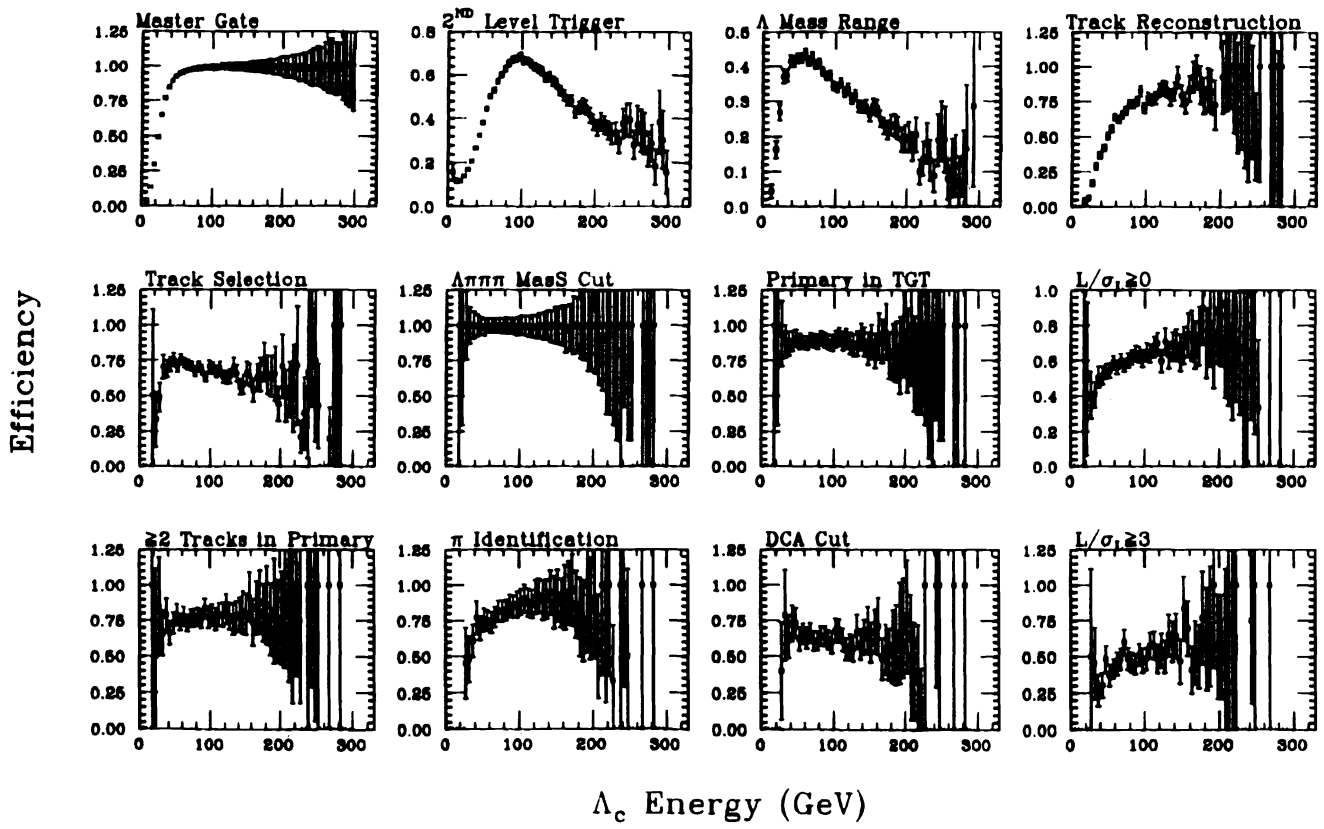

Figure 4.19: Efficiencies for successive cuts used in the $\Lambda\pi^+\pi^+\pi^-$ analysis.

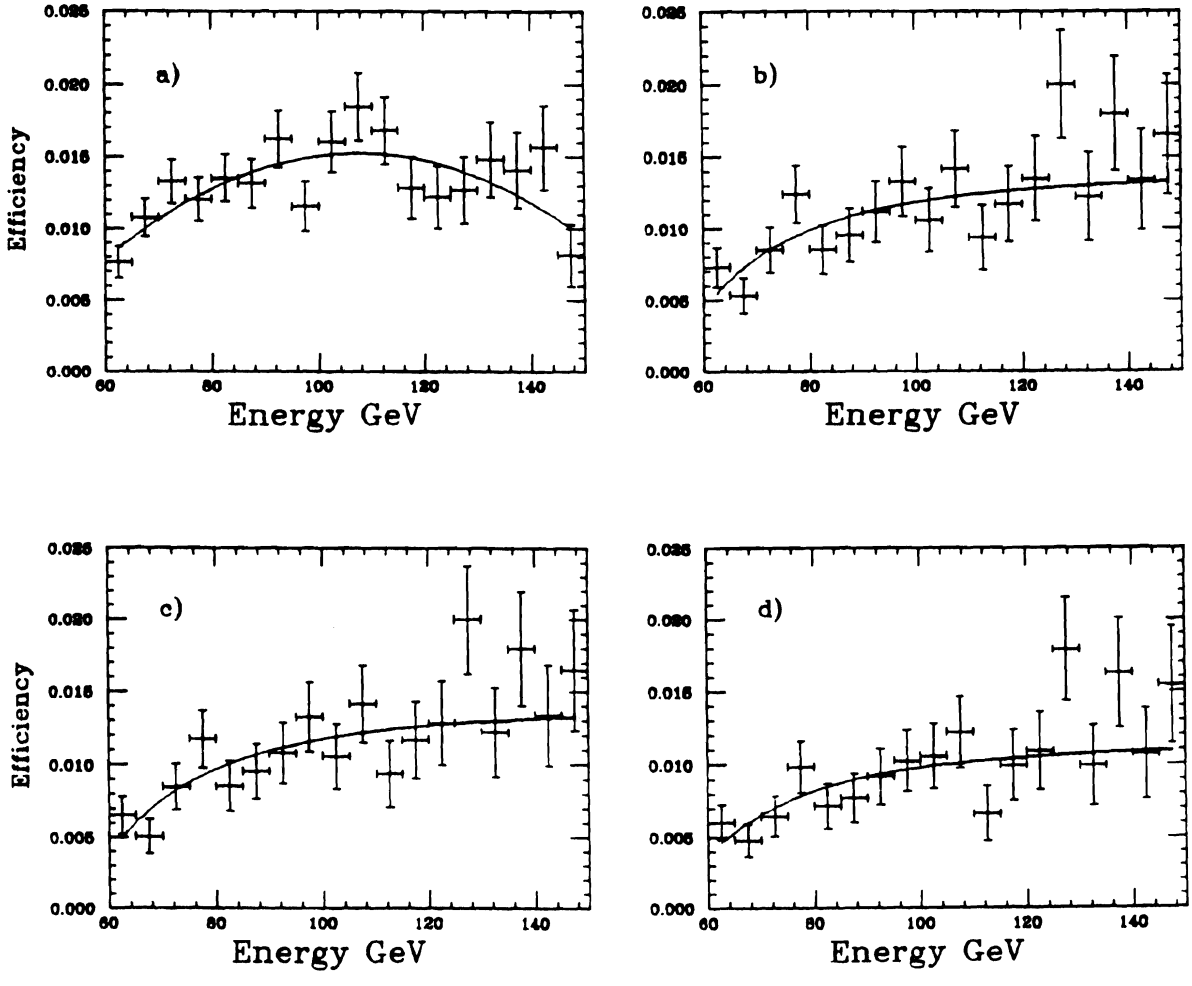

Figure 4.20: Monte Carlo efficiency distributions for final $\Lambda\pi^+\pi^+\pi^-$ and $pK^-\pi^+$ analysis cuts: a) $\Lambda\pi^+\pi^+\pi^-$, b) $pK^-\pi^+$, c)$pK^-\pi^+$ with ϕ mass cut, and d) $pK^-\pi^+$ with combined ϕ, D^+, and D_s^+ mass cuts.

TABLE 4.5
EFFICIENCY DISTRIBUTION FIT RESULTS FOR FINAL $pK^-\pi^+$ AND $\Lambda\pi^+\pi^+\pi^-$ ANALYSIS CUTS

	$pK^-\pi^+$			$\Lambda\pi^+\pi^+\pi^-$
	Standard Cuts	ϕ mass cut	ϕ/D mass cuts	Standard Cuts
χ^2	16.87	15.66	17.51	16.61
DOF	16	16	16	16
C.L.	.394	.477	.3537	.3430
Parameter				
A	.01390	.01400	.01148	.0224
B	−2054	−2183	−1683.	$.7006 \times 10^{-3}$
C				$-.3256 \times 10^{-5}$

of the E-687 spectrometer. Studies have been made to determine the validity of these assumptions. In most cases where the Monte Carlo samples were found to differ from the data, the Monte Carlo was modified so that it correctly simulated the data. There are however, processes that are either difficult to Monte Carlo properly or not well understood. In these cases *post hoc* corrections have been employed to match the Monte Carlo response to the data. For the results that will be presented there are several efficiencies of interest. These include corrections for Čerenkov identification of the tracks, linking, and the Λ strip. In addition loss of particles due to hadronic interactions in the target and spectrometer is not modeled in ROGUE.

Cerenkov Efficiencies

Differences in Čerenkov efficiencies between Monte Carlo and data can arise from noise in the Čerenkov counters, or from out of time tracks that produce additional light in the counters causing confusion in the identification of tracks. Neither of these processes is simulated in ROGUE. For Čerenkov identification of heavy particles (protons and kaons) these processes will tend to reduce the true efficiency for data relative to the Monte Carlo efficiency since these particles are identified by the absence of light in the Čerenkov system. The Monte Carlo Čerenkov efficiencies were checked against samples of events from topologically identified final states. For these studies the K^0_s's were used to tag pion tracks, Λ's

were used to tag proton tracks, and D's were used to tag kaon tracks. In all three cases, no Čerenkov cuts were applied in selecting the initial event samples.

For the comparison of pion identification, samples of K_s^0's from data and Monte Carlo were used [25]. The tracks were classified by their type, 3-chamber and 5-chamber, and by the Čerenkov identification for each track. For this study the Čerenkov identification categories considered were pion definite, ISTATP=2, and pion consistent, ISTATP=2,3,7,13,14,15. The efficiency is then given by the number of tracks for a given track type and Čerenkov category divided by the total number of tracks of that track type. The pion Čerenkov identification efficiencies for data and for Monte Carlo samples are given in Table 4.6. The results show good agreement between the efficiencies for data and Monte Carlo. No corrections were made to the Monte Carlo efficiencies for pion Čerenkov identification.

TABLE 4.6
PION ČERENKOV IDENTIFICATION EFFICIENCIES FOR DATA AND MONTE CARLO

Track Type	Čerenkov ID.	Efficiency	
		Data	Monte Carlo
3-chamber	π Consistent	0.90	0.90
	π Definite	0.78	0.79
5-chamber	π Consistent	0.94	0.95
	π Definite	0.80	0.82

The proton Čerenkov identification efficiency studies used samples of Track-Track and Stub-Stub vee candidates from data and Monte Carlo that had no Čerenkov cuts placed on the fast track of the vee, which was assumed to be the proton track. Track-Track vees provided the sample of 5-chamber tracks, while the 3-chamber tracks came from the Stub-Stub vee sample. The data sample was obtained from approximately 2% of the PASS 1 tapes which were reprocessed to acquire samples of Λ candidates without any Čerenkov cuts. The Monte Carlo study was performed using a sample of 100,000 $\gamma p \rightarrow \Lambda_c^+ \bar{c}\, meson + C.C.$, $\Lambda_c^+ \rightarrow \Lambda\pi^+\pi^+\pi^-$, $\Lambda \rightarrow p\pi^-$ events. The samples were divided according to vee type and ISTATP classification of the fast track. The resulting $p\pi^-$ mass distributions for both the data and the Monte Carlo samples are shown in Fig. 4.21. The mass distributions were fit with

double-Gaussian signals and polynomial backgrounds. The signals obtained from the fits are given in Table 4.7. The efficiency was defined as the number of candidates as determined by fit for a given vee type and Čerenkov classification divided by the number of candidates with no Čerenkov requirements for that vee type. The efficiency values for each track type are given in Table 4.8. The correction factor is given by the ratio of the data efficiency to the Monte Carlo efficiency for a given track type and ISTATP classification. No corrections to the Monte Carlo efficiencies were made for the proton identification.

TABLE 4.7
Λ YIELDS BY TRACK TYPE AND ČERENKOV IDENTIFICATION OF PROTON TRACK

Category	No Cuts	ISTATP=8	ISTATP=12	ISTATP=8,12
Track Data	2936 ± 118	1139 ± 38	1313 ± 48	2441 ± 68
Track MC	8623 ± 96	3180 ± 59	4725 ± 71	7442 ± 88
Stub Data	3478 ± 132	808 ± 43	2456 ± 80	3400 ± 110
Stub MC	5568 ± 79	1366 ± 39	3769 ± 64	5161 ± 74

TABLE 4.8
PROTON ČERENKOV EFFICIENCIES FOR MONTE CARLO AND DATA

Category	ISTATP=8	ISTATP=12	ISTATP=8,12
Track Data	0.388 ± .020	0.448 ± .023	0.832 ± 0.041
Track MC	0.369 ± .001	0.548 ± .010	0.863 ± 0.014
Correction factor	1.052 ± .059	0.817 ± .045	0.964 ± 0.050
Stub Data	0.232 ± .015	0.706 ± .046	0.978 ± 0.049
Stub MC	0.245 ± .001	0.677 ± .021	1.043 ± 0.076
Correction factor	0.947 ± .069	1.043 ± .076	1.055 ± 0.057

The kaon Čerenkov efficiency studies were made using a sample of $D \rightarrow K\pi$, $K\pi\pi$, $K\pi\pi\pi$ events that were obtained using a vertex based skim without Čerenkov cuts on the kaon track candidate [40]. The sample was reanalyzed requiring that the kaon candidate be identified by the Čerenkov system as kaon consistent, ISTATP=4,12,7 (P>60 GeV/c), and subdivided based on the track type of the kaon candidate. The efficiency for the

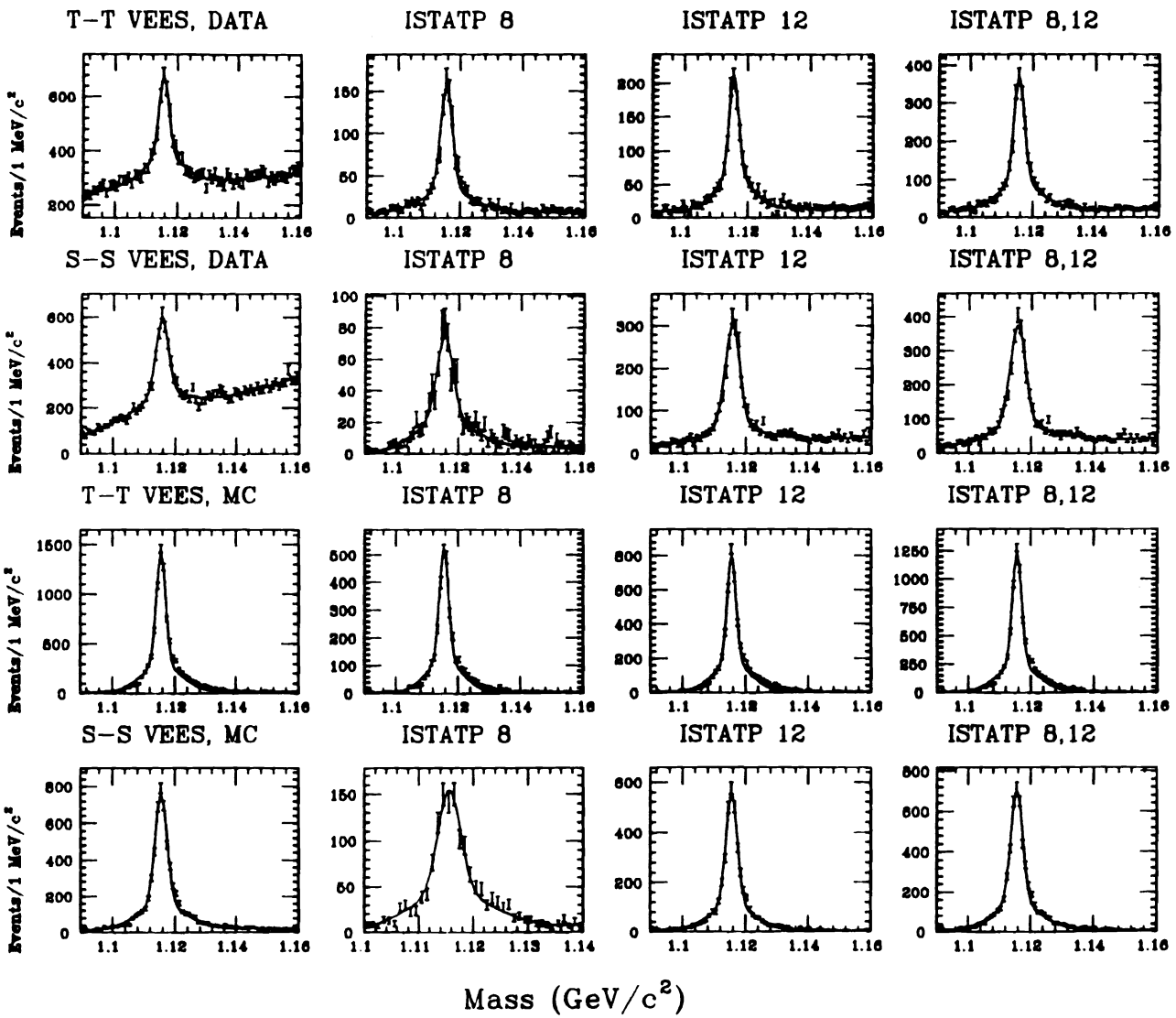

Figure 4.21: Λ distributions from data and Monte Carlo used to determine the proton Čerenkov efficiency.

kaon Čerenkov identification requirement was determined by the ratio of events with and without the Čerenkov requirement for the 5-chamber and 3-chamber kaon candidates. A similar study was performed on a sample of Monte Carlo $D \rightarrow K\pi$, $K\pi\pi\pi$ events to measure the Čerenkov efficiency for identifying kaon's in Monte Carlo. The results for the studies are summarized in Table 4.9. The correction factor to the efficiency is given by the ratio of the data efficiency to the Monte Carlo efficiency. Corrections for Čerenkov identification of both 3-chamber and 5-chamber kaons were made to the $pK^-\pi^+$ Monte Carlo efficiency.

TABLE 4.9
KAON ČERENKOV EFFICIENCIES FOR MONTE CARLO AND DATA

	3 Chamber	5 Chamber
Monte Carlo	$0.698 \pm .034$	$.843 \pm 0.024$
Data	$0.641 \pm .082$	$.670 \pm 0.052$
Correction	$0.918 \pm .126$	$.795 \pm 0.066$

4.3.3 Λ Strip Efficiency

The Λ strip is based largely on Čerenkov requirements, and may also exhibit differences in efficiencies between data and Monte Carlo. The categories of vees that are susceptible to these differences are the the SSDV's and the M1VEE's. The other vee categories were stripped only on the basis of the $p\pi^-$ invariant mass for the two track combination. The data and Monte Carlo samples were the same as those used for proton Čerenkov identification efficiency studies. The resulting $p\pi^-$ mass distributions before and after the Λ strip requirements (excluding the mass cut) are shown in Fig. 4.22. The distributions were fit with double Gaussian signals and polynomial backgrounds; the signals were integrated over the mass range $1.10\,GeV/c^2 \leq M(p\pi) \leq 1.14\,GeV/c^2$ to determine the yields. The resulting yields for each vee category are given in Table 4.10. The efficiencies were determined by the ratio of the number of events with and without the strip requirements as determined by the fits to the mass distributions, and are given in Table 4.11. The correction factor was determined by the ratio of the data efficiency to Monte Carlo efficiency. Corrections to the $\Lambda\pi^+\pi^+\pi^-$ Monte Carlo efficiency were made for these four categories of Λ's.

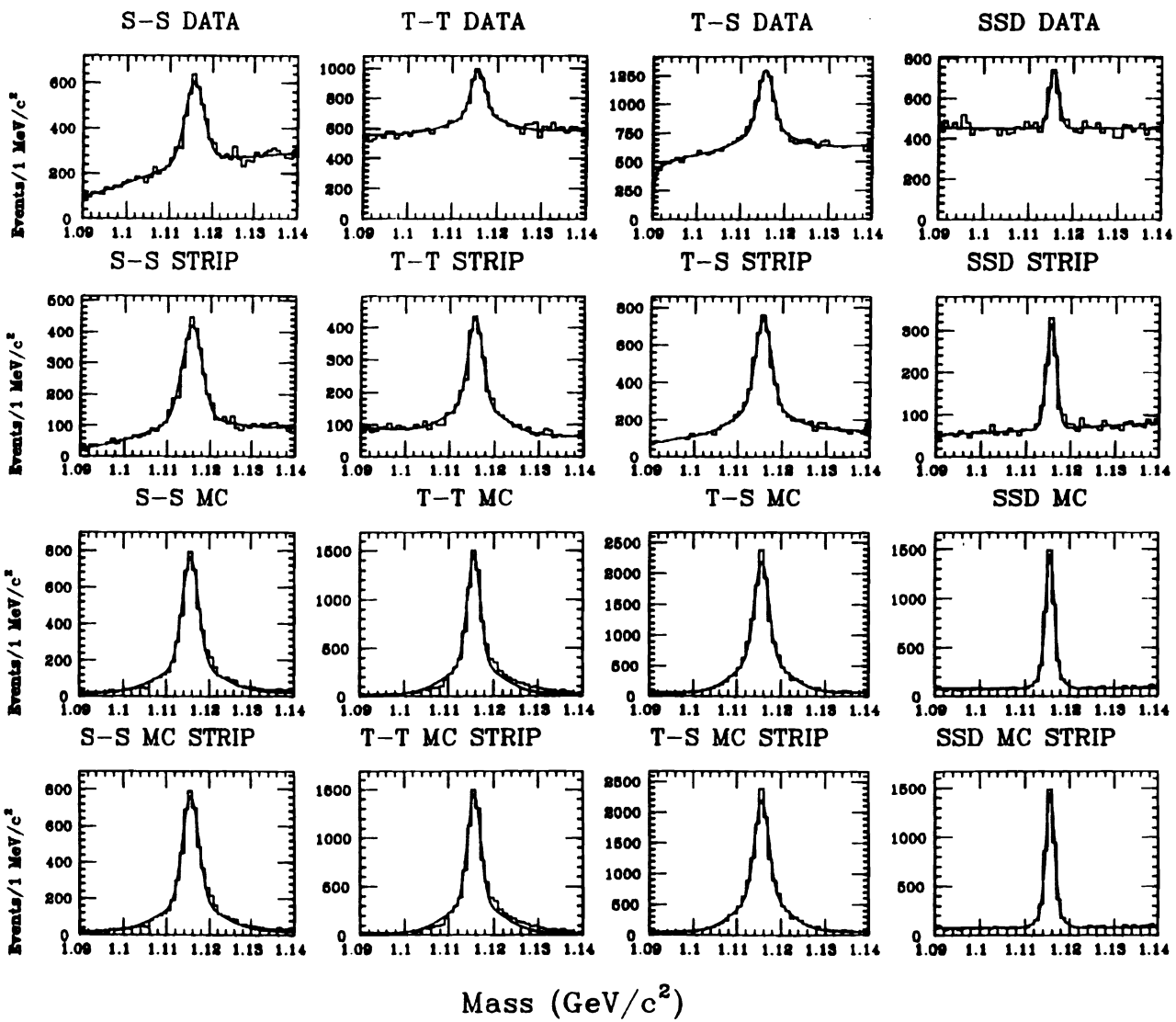

Figure 4.22: Λ distributions from data and Monte Carlo used to determine the Λ strip efficiency.

TABLE 4.10
LAMBDA STRIP YIELDS FOR SSDVEE'S AND M1VEE'S

Vee Type	Raw Data	Strip Data	Raw M.C.	Strip M.C.
SS vees	3781 ± 135	3118 ± 955	5427 ± 353	5050 ± 325
TS vees	4506 ± 171	4071 ± 123	14488 ± 298	14247 ± 282
TT vees	2775 ± 161	2330 ± 82	8764 ± 229	7952 ± 212
SSD vees	772 ± 46	710 ± 59	3834 ± 217	3595 ± 95

TABLE 4.11
LAMBDA STRIP EFFICIENCIES FOR SSDVEE'S AND M1VEE'S

Vee Type	Eff. Data	Eff. M.C.	Correction
SS vees	$0.82 \pm .04$	0.93 ± 0.08	0.89 ± 0.08
TS vees	$0.90 \pm .04$	0.98 ± 0.03	0.92 ± 0.05
TT vees	$0.84 \pm .08$	0.91 ± 0.03	0.93 ± 0.10
SSD vees	$0.92 \pm .09$	0.94 ± 0.06	0.98 ± 0.12

Linking Efficiency

The linking efficiencies for Monte Carlo and data were compared using the following procedure [40]. PWC tracks were pointed back to vertices found by the SSD vertex finding algorithm VERTIC and the normalized miss distance in the x plane was determined. Associating a PWC track with a VERTIC vertex insured that the track was neither spurious nor associated with long lived vee secondaries. The tracks were classified according to track type, and divided into momentum bins. The normalized miss distances were fit with Gaussian functions to determine the total number of tracks in each category. The efficiency was determined by the ratio of the linked tracks to total tracks for a given momentum bin as determined by the Gaussian fit. The resulting efficiency distributions were fit with the functional form [41]:

$$\epsilon(P) = A + \frac{B}{P} + \frac{C}{P^2} + \frac{D}{P^2} + \frac{E}{P^4}$$

The coefficients for the fits for each case are given in Table 4.12. The efficiency correction was determined by the ratio of the data efficiency to Monte Carlo efficiency and was applied

on a track by track basis. The correction factors as a function of momentum for 3-chamber and 5-chamber tracks are shown in Fig. 4.23. Linking efficiency corrections were made to both the $pK^-\pi^+$ and $\Lambda\pi^+\pi^+\pi^-$ Monte Carlo efficiencies.

TABLE 4.12
COEFFICIENTS FOR LINKING EFFICIENCY CORRECTIONS

	A	B	C	D	E
Stubs MC	0.980	0.026	0.053	-0.397	0.039
Stubs Data	0.875	1.545	-10.88	24.98	-19.89
Tracks MC	0.980	0.589	-12.78	109.00	-307.4
Tracks Data	0.977	0.696	-23.82	196.60	-521.7

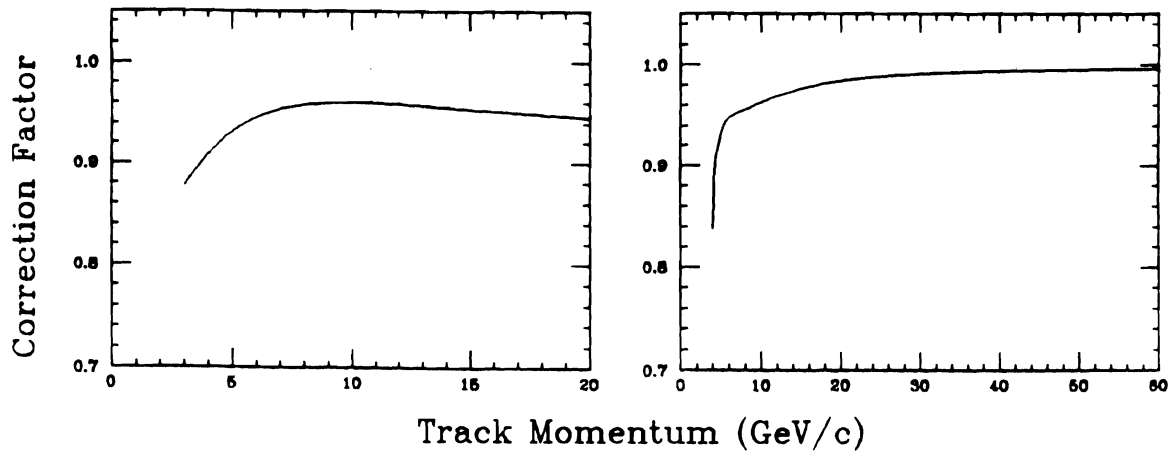

Figure 4.23: Linking efficiency corrections for 3-chamber and 5-chamber tracks as a function of the track momentum.

Hadronic Absorption

The term "hadronic absorption" will be used to refer to the processes in which particles interact strongly in the target or spectrometer in such a way that the system from which they originated can not be reconstructed or identified. Hadronic absorption of the decay particles in the target and spectrometer material is not modeled in ROGUE. In order to account for the probability of hadronic absorption of a secondary particle, a *post hoc*

correction was made to the Monte Carlo efficiency to correct for the probability that one of the decay particles interacted before traversing the spectrometer. The model used to determine the probability of absorption made no distinction for particle type, assumed that the absorption probability was independent of the particle momentum, and that tracks reaching P2 were reconstructable. The probability that the final state was absorbed is given by the form $1 - e^{-nf}$, where n is the number of tracks in the final state, and f is the fraction of absorption lengths between the decay vertex and the first plane of P2. For the decay modes with a Λ candidate in the final state, the multiplicity is n for the region between the charm candidate decay vertex and the Λ decay vertex, and $n+1$ for the region between the Λ decay vertex and the first plane of P2.

4.4 $\Lambda_c^+ \to \Lambda\pi^+\pi^+\pi^-$ to $\Lambda_c^+ \to pK^-\pi^+$ Branching Ratio Measurement

The final $\Lambda_c^+ \to \Lambda\pi^+\pi^+\pi^-$ to $\Lambda_c^+ \to pK^-\pi^+$ branching ratio measurement was made using the efficiency corrected yields for the $\Lambda\pi^+\pi^+\pi^-$ and $pK^-\pi^+$ decay modes. The final samples were restricted to the energy range $60\ GeV \leq E(\Lambda_c^+) \leq 150\ GeV$. The energy limits were determined by the $\Lambda\pi^+\pi^+\pi^-$ signal. The lower energy cut was necessary to extract the signal, while the upper limit is a result of the finite decay volume for which Λ's can be reconstructed in the E-687 spectrometer. For the $pK^-\pi^+$ decay mode three sets of cuts were used to generate efficiency corrected mass distributions: the standard cuts described in Sec. 4.1.1, the standard cuts plus the ϕ mass cut, and the standard cuts plus the combined ϕ, D^+, and D_s^+ mass cuts described in Sec. 4.1.2. The resulting mass distributions for the samples used in the branching ratio measurement are shown in Fig. 4.24. The distributions were fit with Gaussian signals and linear backgrounds; results are given in Table 4.13 . The efficiency for each candidate was determined on a event by event basis using the efficiency parametrizations described in Sec. 4.3.1 for both modes, and the different analysis cuts. For the $\Lambda\pi^+\pi^+\pi^-$ decay mode, *post hoc* corrections were made for linking and Λ strip efficiency differences, and for hadronic absorption. Linking, kaon Čerenkov identification, and hadronic absorption corrections were applied to the $pK^-\pi^+$ efficiency. A weighted mass distribution was generated for each mode using the inverse of the overall efficiency as the weighting factor. The resulting mass distributions are shown in Fig. 4.25. The

distributions were fit with Gaussian signals and linear backgrounds and integrated over the mass region including $\pm 3\sigma$ from the nominal Λ_c^+ mass of 2285 MeV/c^2 to determine the efficiency corrected yields. The results of the fits to the weighted mass distributions are given in Table 4.14. The relative branching ratio is then calculated as:

TABLE 4.13
FIT RESULTS OF Λ_c^+ MASS DISTRIBUTIONS USED FOR BRANCHING RATIO MEASUREMENT

	$pK\pi$			$\Lambda\pi\pi\pi$
Cuts	Standard	ϕ mass	ϕ/D	Standard
Mass(MeV/c^2)	2287 ± 4	2288 ± 4	2288 ± 5	2284 ± 3
σ(MeV/c^2)	18 ± 3	19 ± 3	$21pm2$	9.6 ± 2.8
Yield	141 ± 29	142 ± 28	123 ± 28	57 ± 17
S/N	0.33	0.36	0.38	0.25
Fit C.L.	0.14	0.18	0.07	0.09

TABLE 4.14
FIT RESULTS OF EFFICIENCY CORRECTED Λ_c^+ MASS DISTRIBUTIONS USED FOR BRANCHING RATIO MEASUREMENT

	$pK\pi$			$\Lambda\pi\pi\pi$
Cuts	Standard	ϕ mass	ϕ/D	Standard
Mass(MeV/c^2)	2287 ± 4	2288 ± 4	2286 ± 5	2285 ± 3
σ(MeV/c^2)	17 ± 3	18 ± 3	17 ± 3	8.8 ± 2.0
Yield	19956 ± 3957	21021 ± 3169	19113 ± 3124	7351 ± 1784
S/N	0.28	0.30	0.28	0.26
Fit C.L.	0.02	0.01	0.01	0.12

$$\frac{BR(\Lambda_c^+ \to \Lambda\pi^+\pi^+\pi^-)}{BR(\Lambda_c^+ \to pK^-\pi^+)} = \frac{N_c(\Lambda\pi^+\pi^+\pi^-)}{N_c(pK^-\pi^+)} \cdot \frac{1}{BR(\Lambda \to p\pi^-)}$$

where N_c is the efficiency corrected yield for the decay mode given in Table 4.14, and $BR(\Lambda \to p\pi^-) = 0.641$. The branching ratios for the three sets of cuts on the $pK^-\pi^+$ sample are given in Table 4.15. The different sets of cuts make no significant difference in

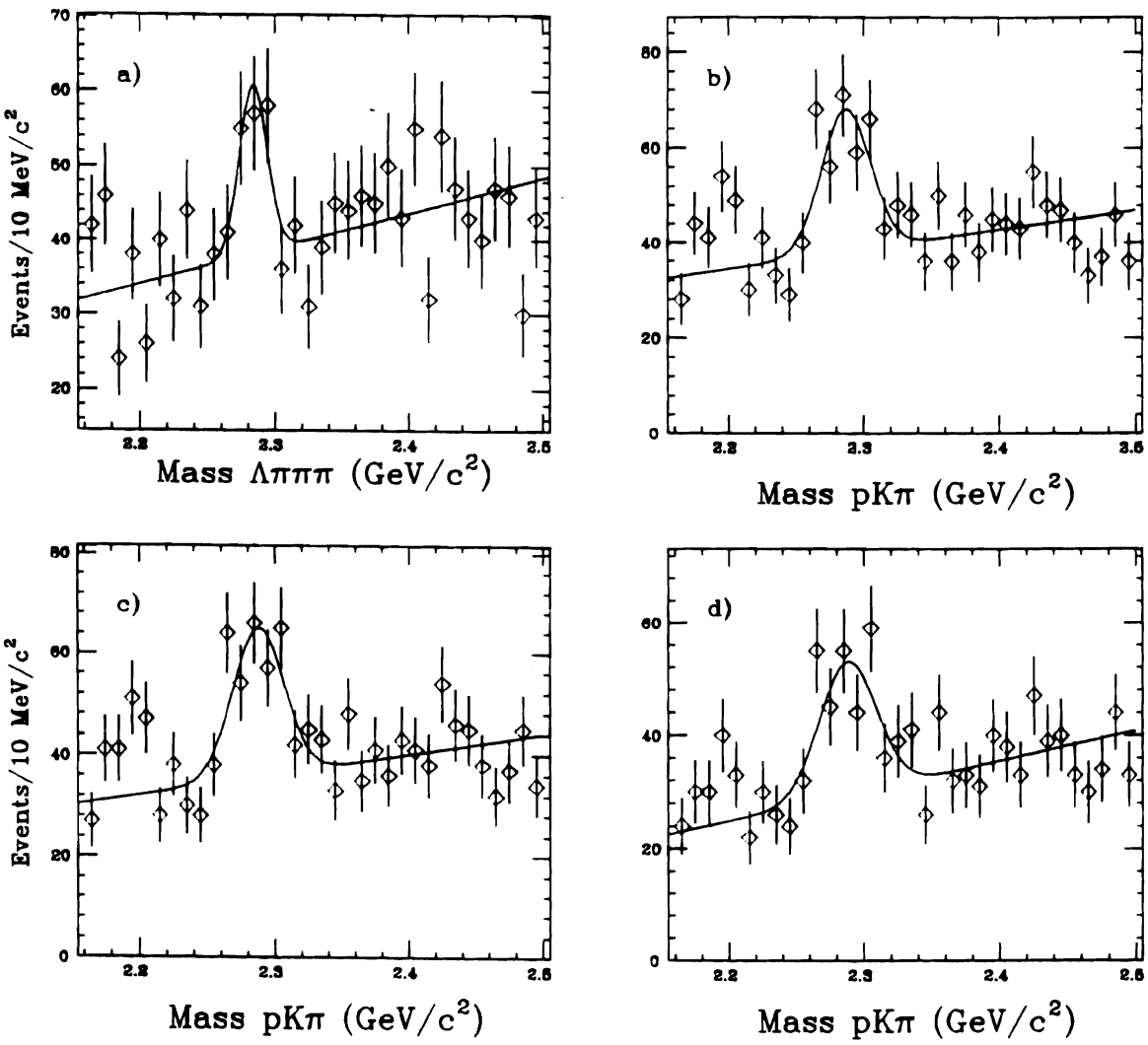

Figure 4.24: $\Lambda\pi^+\pi^+\pi^-$ and $pK^-\pi^+$ mass distributions used for branching ratio measurement: a) $\Lambda\pi^+\pi^+\pi^-$ mass distribution, b) $pK^-\pi^+$ mass distribution for standard analysis cuts, c) $pK^-\pi^+$ mass distribution for standard analysis cuts and ϕ mass cut, and d) $pK^-\pi^+$ mass distribution for standard analysis cuts and combined ϕ, D^+, and D_s^+ mass cuts.

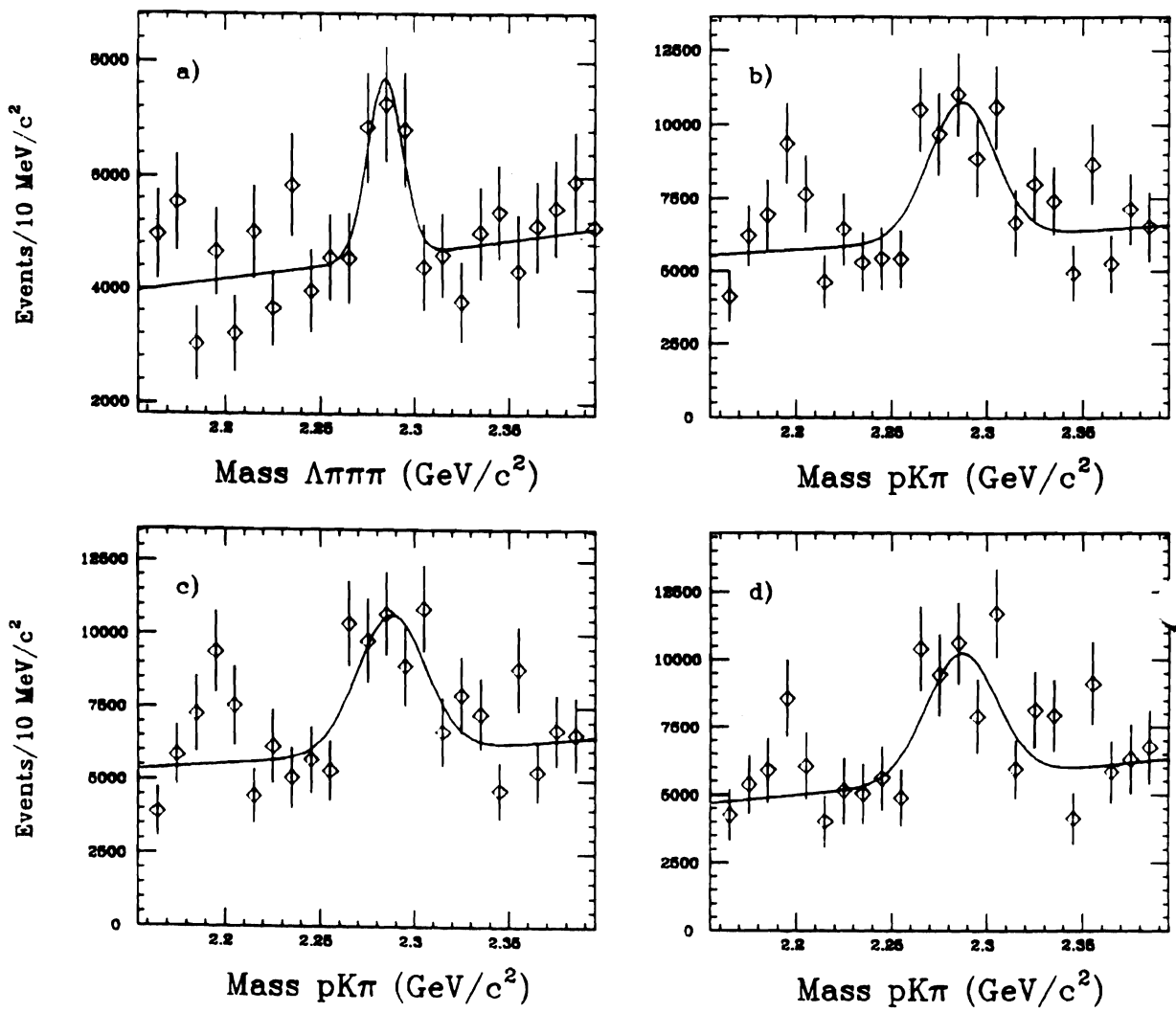

Figure 4.25: Efficiency corrected $\Lambda\pi^+\pi^+\pi^-$ and $pK^-\pi^+$ mass distributions used for the branching ratio measurements: a) $\Lambda\pi^+\pi^+\pi^-$ mass distribution, b) $pK^-\pi^+$ mass distribution for standard analysis cuts, c) $pK^-\pi^+$ mass distribution for standard analysis cuts and ϕ mass cut, and d) $pK^-\pi^+$ mass distribution for standard analysis cuts and combined ϕ, D^+, and D_s^+ mass cuts.

TABLE 4.15
$\Lambda\pi^+\pi^+\pi^-$ TO $pK^-\pi^+$ BRANCHING RATIOS FOR THE DIFFERENT $pK^-\pi^+$ ANALYSIS CUTS

Analysis cuts	Branching ratio
Standard	0.57 ± 0.18
ϕ mass	0.55 ± 0.16
ϕ, D^+, D_s^+ mass	0.60 ± 0.18

the final branching ratio. For the final result the efficiency corrected yield for the sample with the ϕ mass cut is chosen:

$$\frac{BR(\Lambda_c^+ \to \Lambda\pi^+\pi^+\pi^-)}{BR(\Lambda_c^+ \to pK^-\pi^+)} = 0.55 \pm 0.16 \pm 0.15$$

The systematic error has been estimated by varying the parametrization of the efficiency functions within reasonable limits to determine the changes in yields for the weighted mass distributions.

4.5 $\Lambda_c^+ \to p\overline{K^{*0}}$ to $\Lambda_c^+ \to pK^-\pi^+$ Branching Ratio Measurement

The $pK^-\pi^+$ sample was analyzed to determine the relative fraction of $p\overline{K^{*0}}$ events in the signal. For this measurement, the full $pK^-\pi^+$ sample for $L/\sigma_L \geq 3.5$ with the ϕ mass cut was used. The resulting $pK^-\pi^+$ signal is shown in Fig. 4.26. The distribution was fit with a Gaussian signal and linear background. The Gaussian had $M = 2284 \pm 2\ MeV/c^2$, $\sigma = 13.2 \pm 2.4\ MeV/c^2$, S/N=0.511, and C.L.=0.42. In order to determine the number of $p\overline{K^{*0}}$ events, a signal region of $2.255\ GeV/c^2 \leq M(pK^-\pi^+) \leq 2.315\ GeV/c^2$ was defined. The Λ_c^+ yield in the signal region was determined to be 151 ± 52 events by integrating the fit over the signal region. In order to estimate the $\overline{K^{*0}}$ background two sidebands were defined, a lower sideband, $2.170\ GeV/c^2 \leq M(pK^-\pi^+) \leq 2.230\ GeV/c^2$, and an upper sideband, $2.340\ GeV/c^2 \leq M(pK^-\pi^+) \leq 2.400\ GeV/c^2$. The widths of the sidebands were chosen to match the width of the signal region. The resulting $K^-\pi^+$ mass distributions for the signal region, lower and upper sidebands, and the combined sidebands are shown in Fig. 4.27. The mass distributions were fit with a Breit-Wigner signal constraining the mass to be 896 MeV/c^2 and the width to be 52 MeV/c^2, and a third order polynomial

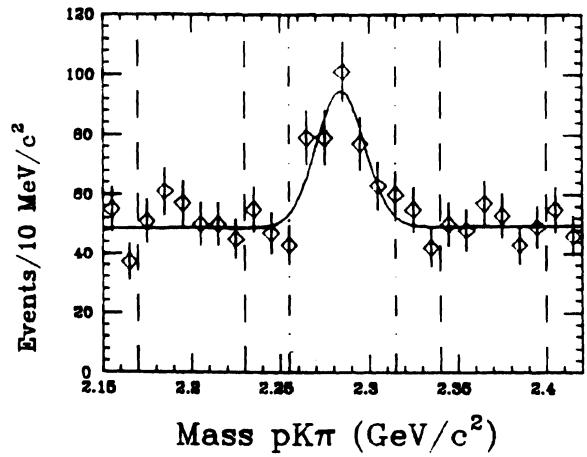

Figure 4.26: $pK^-\pi^+$ sample used for the $p\overline{K^{*0}}$ branching ratio measurement. Dashed lines indicate the low and high side band regions. Dot-dashed lines indicate the signal region.

background. The signal was integrated over the mass range 0.700 $GeV/c^2 \leq M(K^-\pi^+) \leq$ 1.200 GeV/c^2 to determine the $\overline{K^{*0}}$ yield. The results of the fits to the signal region, lower and upper sidebands, and combined sideband distributions are given in Table 4.16. In

TABLE 4.16
FIT RESULTS FOR $p\overline{K^{*0}}$ BRANCHING RATIO ANALYSIS

Mode	Yield	S/N	C.L.
K^{*0} Signal region	45 ± 12	0.49	0.13
K^{*0} Lower sideband	28 ± 12	0.39	0.02
K^{*0} Upper sideband	21 ± 10	0.33	0.92
K^{*0} Combined sideband	47 ± 12	0.42	0.87

order to determine the yield of $\overline{K^{*0}}$'s from $\Lambda_c^+ \to p\overline{K^{*0}}$ decays a sideband subtraction was performed. Subtracting the average of the lower and upper sideband yields, or using half the combined sideband yield, gave resulting signals of 21 ± 15 and 22 ± 14 events respectively. The relative branching fraction is then given by the relation:

$$\frac{BR(\Lambda_c^+ \to p\overline{K^{*0}})}{BR(\Lambda_c^+ \to pK^-\pi^+)} = \frac{N(\overline{K^{*0}})}{N(pK^-\pi^+)} \cdot \frac{\epsilon(pK^-\pi^+)}{\epsilon(p\overline{K^{*0}})} \cdot \frac{1}{BR(\overline{K^{*0}} \to K^-\pi^+)}$$

The efficiency for each of the final states was determined using ROGUE Monte Carlo events, 77,000 $\Lambda_c^+ \rightarrow pK^-\pi^+$, and 50,000 $\Lambda_c^+ \rightarrow p\overline{K^{*0}}$ events. The efficiency was determined independent of the final state energy, and no further *post hoc* corrections were applied to either state, since the observed final states are identical for both cases. The efficiencies were determined to be 0.0103 ± 0.0004 for the $p\overline{K^{*0}}$ mode and 0.0094 ± 0.0004 for the $pK^-\pi^+$ mode. The efficiency corrected relative branching fraction is then:

$$\frac{BR(\Lambda_c^+ \rightarrow p\overline{K^{*0}})}{BR(\Lambda_c^+ \rightarrow pK^-\pi^+)} = 0.20 \pm 0.12 \pm 0.10$$

using the combined sidebands to determine the background contribution, and $BR(\overline{K^{*0}} \rightarrow K^-\pi^+) = 0.66$. The systematic error was estimated by varying the fit parameters for the $\overline{K^{*0}}$ fits.

4.6 $\Lambda_c^+ \rightarrow \Delta^{++}K^-$ to $\Lambda_c^+ \rightarrow pK^-\pi^+$ Branching Ratio Measurement

A search for a Δ^{++} resonance component in the $pK^-\pi^+$ signal was made using the $pK^-\pi^+$ sample for $L/\sigma_L \geq 3.0$, with the ϕ mass cut and $E(pK^-\pi^+) \geq 60\ GeV$. The resulting mass distribution is shown in Fig. 4.28. The distribution was fit with a Gaussian signal and linear background. In order to determine the number of $\Lambda_c^+ \rightarrow \Delta^{++}K^-$ events, a signal region of $2.255\ GeV/c^2 \leq M(pK^-\pi^+) \leq 2.315\ GeV/c^2$ was defined. The Gaussian signal had $M = 2284 \pm 3\ MeV/c^2$, $\sigma = 15.0 \pm 2.9\ MeV/c^2$, S/N=0.41, and C.L.=0.60. The Λ_c^+ yield in this signal region was determined to be 116 ± 20 events by integrating the fit over the signal region mass range. The background was estimated from two sideband regions, a lower sideband, $2.170\ GeV/c^2 \leq M(pK^-\pi^+) \leq 2.230\ GeV/c^2$, and an upper sideband, $2.340\ GeV/c^2 \leq M(pK^-\pi^+) \leq 2.400\ GeV/c^2$. The $p\pi^+$ mass distributions for the three regions, and the combined sidebands are shown in Fig. 4.29. The distributions were each fit with a Breit-Wigner signal constraining the mass to be $1.232\ GeV/c^2$, and the width to be $140\ MeV/c^2$ and second order polynomial background. The Δ^{++} yield was determined by integrating the signal over the mass range $1.080\ GeV/c^2 \leq M(p\pi^+) \leq 1.1510\ GeV/c^2$ to determine the Δ^{++} yield. The mass and width were determined by a fit to Monte Carlo events. Results of the fits to the mass distributions are given in Table 4.17. A sideband subtraction was performed to determine the number of Δ^{++}'s from $\Lambda_c^+ \rightarrow \Delta^{++}K^-$ decays. Using the average of the lower and upper side band yields, and half the combined sideband

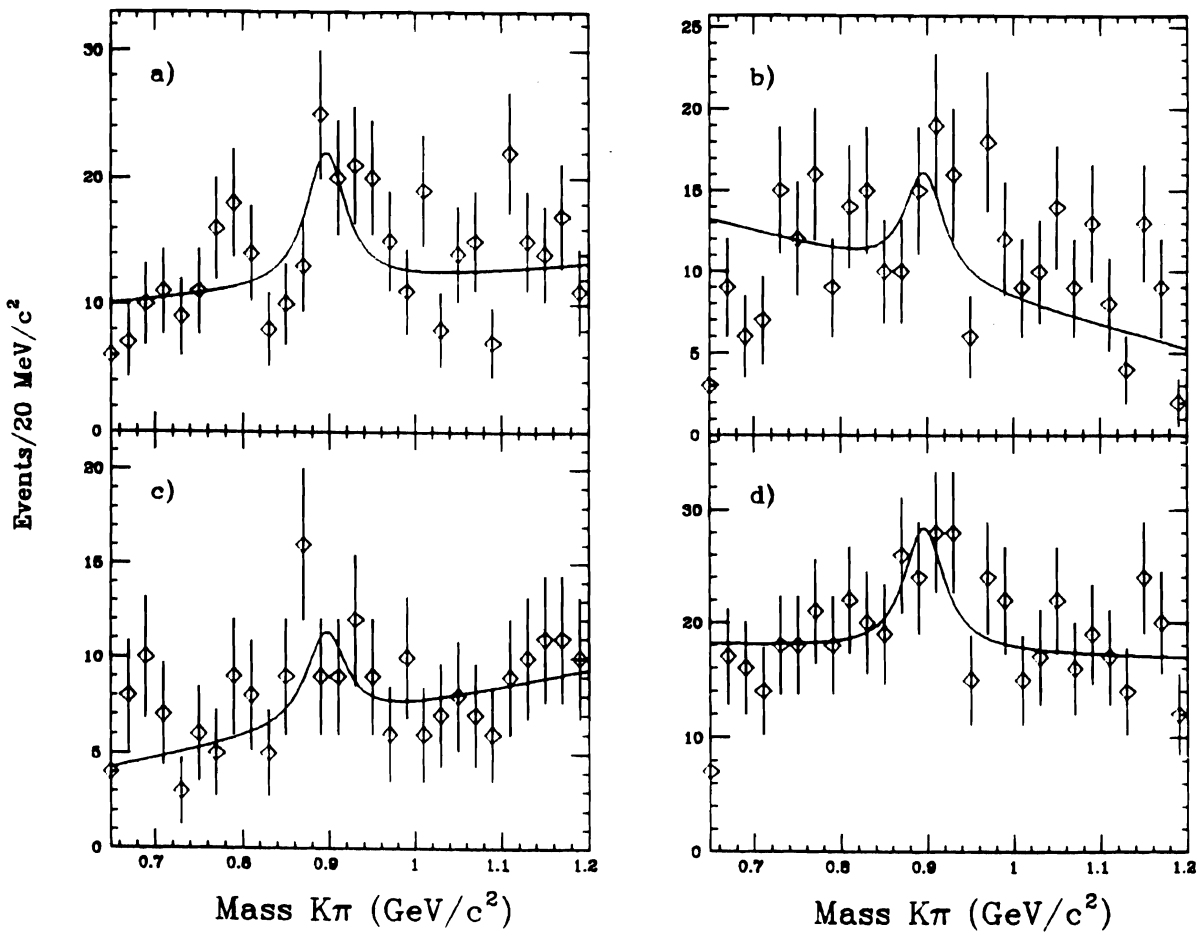

Figure 4.27: $\overline{K^{*0}}$ signals used for the $p\overline{K^{*0}}$ branching ratio measurement: a) From $pK^-\pi^+$ signal region, 2.255 $GeV/c^2 \leq M(pK^-\pi^+) \leq$ 2.315 GeV/c^2, b) Lower sideband region, 2.170 $GeV/c^2 \leq M(pK\pi) \leq$ 2.230 GeV/c^2, c) Upper sideband region, 2.340 $GeV/c^2 \leq M(pK\pi) \leq$ 2.400 GeV/c^2, and d) Combined lower and upper sideband regions.

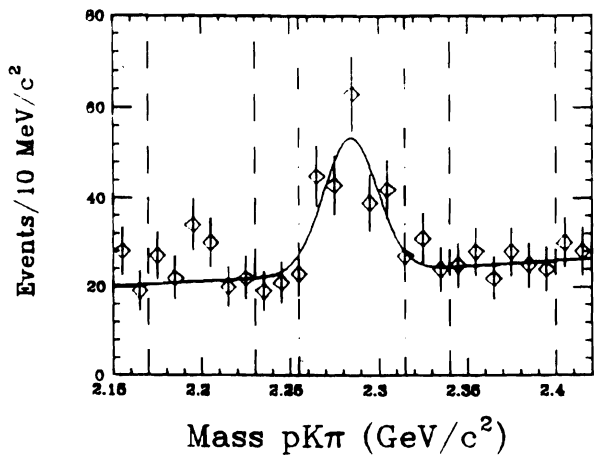

Figure 4.28: $pK^-\pi^+$ sample used for the $\Delta^{++}K^-$ branching ratio measurement. Dashed lines indicate the low and high side band regions. Dot-dashed lines indicate the signal region.

TABLE 4.17
FIT RESULTS FOR $\Delta^{++}K^-$ BRANCHING RATIO ANALYSIS

Mode	Yield	S/N	C.L.
Δ^{++} Signal region	55 ± 13	0.44	0.92
Δ^{++} Lower sideband	45 ± 11	0.45	0.85
Δ^{++} Upper sideband	5 ± 9	0.06	0.45
Δ^{++} Combined sideband	46 ± 15	0.27	0.74

yield, gave signals of 30 ± 15, and 31 ± 15 events respectively. The relative branching fraction is then given by:

$$\frac{BR(\Lambda_c^+ \to \Delta^{++}K^-)}{BR(\Lambda_c^+ \to pK^-\pi^+)} = \frac{N(\Delta^{++})}{N(pK^-\pi^+)} \cdot \frac{\epsilon(pK^-\pi^+)}{\epsilon(\Delta^{++}K^-)}$$

The efficiency for each of the final states was found using ROGUE Monte Carlo events, 77,000 $\Lambda_c^+ \to pK^-\pi^+$ events and 50,000 $\Lambda_c^+ \to \Delta^{++}K^-$ events. The efficiency was determined independent of the final state energy and with no further *post hoc* corrections made. The efficiencies were determined to be 0.0113 ± 0.0006 and 0.0129 ± 0.0008 for the$pK^-\pi^+$ and $\Delta^{++}K^-$ final states respectively. The efficiency corrected relative branching fraction

is then:

$$\frac{BR(\Lambda_c^+ \to \Delta^{++}K^-)}{BR(\Lambda_c^+ \to pK^-\pi^+)} = 0.24 \pm 0.12 \pm 0.10$$

using the background signal as determined by the fit to the combined sideband distribution. The systematic error was estimated by varying the parameters for the fits to the $p\pi^+$ mass distributions.

The Δ^{++} signal was studied in Monte Carlo using a sample of 50,000 $\Lambda_c^+ \to \Delta^{++}K^-$ events. A phase space background was generated using a sample of 77,000 $\Lambda_c^+ \to pK^-\pi^+$ Monte Carlo events. A sample of 50,000 $\Lambda_c^+ \to p\overline{K^{*0}}$ Monte Carlo events was used to generate $p\pi^+$ background from $p\overline{K^{*0}}$ events. The $p\pi^+$ mass distributions for each of the samples are shown in Fig. 4.30. Superimposed on each distribution is the $p\pi^+$ mass distribution for data events from the signal region. The Monte Carlo samples have been normalized to the number of events in the data sample. The $p\pi^+$ mass distributions for phase space and $p\overline{K^{*0}}$ distributions both show evidence of peaking above the Δ^{++} mass region. The $p\pi^+$ mass distribution for data shows an excess of events in the Δ^{++} mass region from what is expected for phase space, or $p\overline{K^{*0}}$ background. The $pK^-\pi^+$ nonresonant and $p\overline{K^{*0}}$ samples were combined weighting the $p\overline{K^{*0}}$ sample to be 10.4% of the signal with the remaining 89.6% decaying according to phase space. The resulting mass distribution is shown in Fig. 4.31 a) with the distribution for data superimposed on it. The distribution for data clearly peaks at a lower mass than the Monte Carlo distribution. Finally the three Monte Carlo samples were combined weighting the samples so that the $p\overline{K^{*0}}$ constituted 10.4% of the sample, $\Delta^{++}K^-$ 16.5% of the sample, and $pK^-\pi^+$ nonresonant the remaining 73.1% of the sample. The resulting $p\pi^+$ mass distribution is shown in Fig. 4.31 b). The distribution was fit with a Breit-Wigner signal and polynomial background. The fit resulted in a mass of $1231 \pm 13\ MeV/c^2$ and a width of $142 \pm 27\ MeV/c^2$ for the signal. The fitted width of $142 \pm 27\ MeV/c^2$ supports the choice of constraining the width to 140 MeV/c^2 for the fits to data.

4.7 Particle, Anti-Particle Asymmetry Studies

The ratios for the production of charm baryons and antibaryons were determined for the $pK^-\pi^+$ and $\Lambda\pi^+\pi^+\pi^-$ signals. The signals were selected requiring $L/\sigma_L \geq 3.0$ and

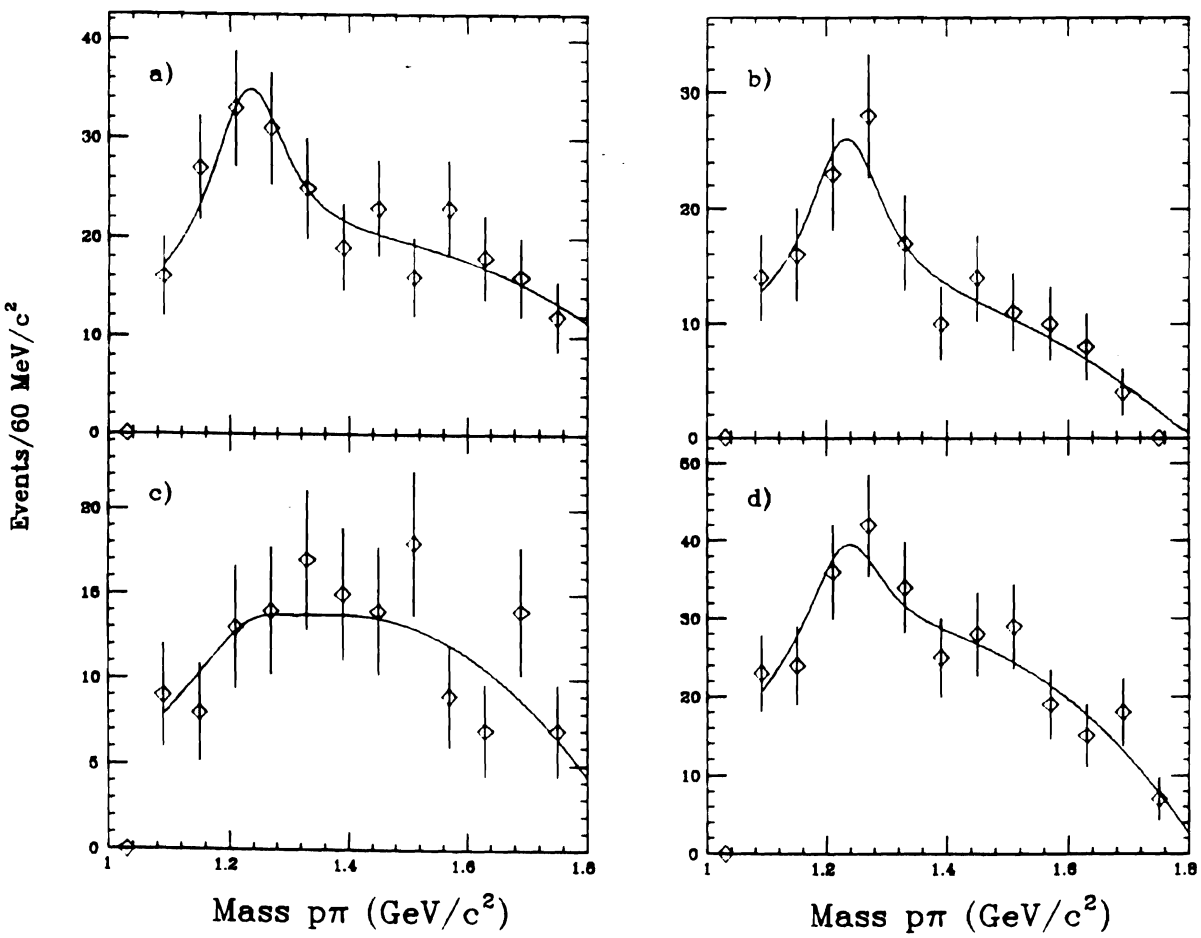

Figure 4.29: $p\pi^+$ mass distributions used for the $\Delta^{++}K^-$ branching ratio measurement: a) From $pK^-\pi^+$ signal region, 2.255 $GeV/c^2 \leq M(pK^-\pi^+) \leq$ 2.315 GeV/c^2, b) Lower sideband region, 2.170 $GeV/c^2 \leq M(pK\pi) \leq$ 2.230 GeV/c^2, c) Upper sideband region, 2.340 $GeV/c^2 \leq M(pK\pi) \leq$ 2.400 GeV/c^2, and d) Combined lower and upper sideband regions.

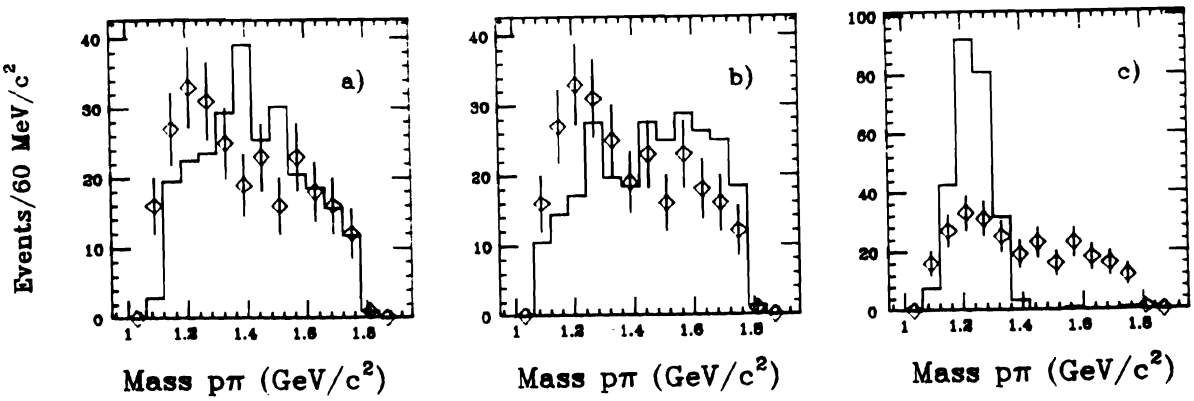

Figure 4.30: $p\pi^+$ mass distribution for Monte Carlo $\Lambda_c^+ \rightarrow pK^-\pi+$ nonresonant, $\Lambda_c^+ \rightarrow p\overline{K^{*0}}$, and $\Lambda_c^+ \rightarrow \Delta^{++}K^-$: a) $\Lambda_c^+ \rightarrow pK^-\pi+$ nonresonant, b) $\Lambda_c^+ \rightarrow p\overline{K^{*0}}$, and c) $\Lambda_c^+ \rightarrow \Delta^{++}K^-$. Solid histograms are Monte Carlo, data points are $p\pi^+$ mass distribution for signal region in data. The Monte Carlo sample has been normalized to the number of events in data.

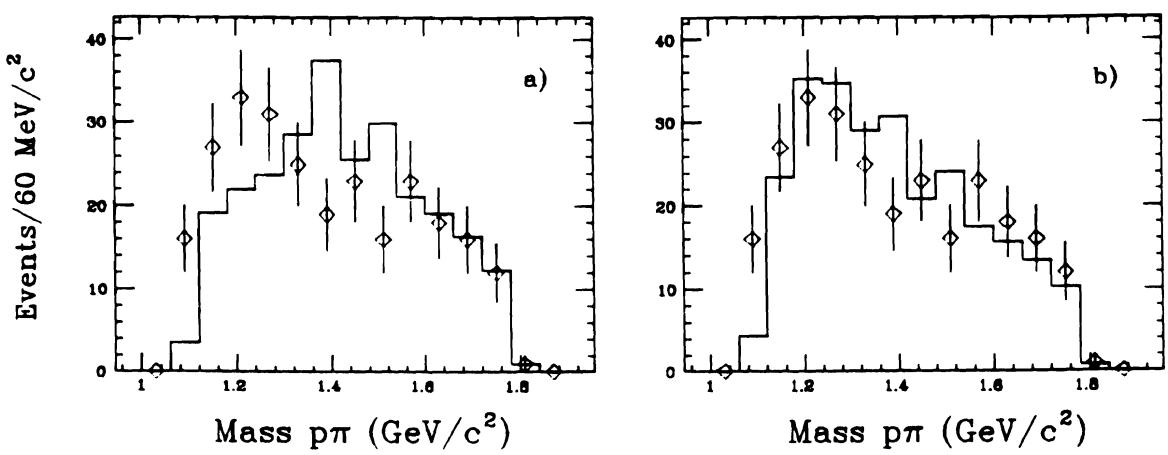

Figure 4.31: $p\pi^+$ mass distributions for Monte Carlo $\Lambda_c^+ \rightarrow pK^-\pi^+$ nonresonant, $p\overline{K^{*0}}$, and $\Lambda_c^+ \rightarrow pK^-\pi^+$ nonresonant, $p\overline{K^{*0}}$, and $\Delta^{++}K^-$: a) $pK^-\pi^+$ nonresonant, $p\overline{K^{*0}}$, and b) $pK^-\pi^+$ nonresonant, $p\overline{K^{*0}}$, $\Delta^{++}K^-$. Solid histograms are Monte Carlo, data points are $p\pi^+$ mass distribution for signal region in data. The Monte Carlo sample has been normalized to the number of events in data.

$E(\Lambda_c^+) \geq 60\ GeV$. In addition, the ϕ mass cut was used for the $pK^-\pi^+$ mode. The candidates were divided into particle and anti-particle samples. The resulting mass distributions are shown in Fig. 4.32. The distributions were fit with Gaussian signals plus linear backgrounds to determine the yields. The results of the fits are given in Table 4.18. The ratio of particle to anti-particle was measured to be 0.97 ± 0.70, and 0.99 ± 0.33 for the $\Lambda\pi^+\pi^+\pi^-$ and $pK^-\pi^+$ modes respectively. The $pK^-\pi^+$ signals show a 4σ mass difference between the particle and the anti-particle masses. The particle and anti-particle masses for the $\Lambda\pi^+\pi^+\pi^-$ mode however show no evidence of a mass difference. An analysis was run on the $pK^-\pi^+$ Monte Carlo sample and the Λ_c^+ and $\overline{\Lambda_c^+}$ masses were consistent within 1σ. The $pK^-\pi^+$ mass distributions were refit constraining the mass and width to the values obtained from fitting the Monte Carlo, 2285 MeV/c^2 and 9 MeV/c^2. The combined sample yielded 85 ± 15 events, while the fits to the Λ_c^+ and $\overline{\Lambda_c^+}$ distributions yielded 52 ± 14 and 36 ± 10 events respectively. The ratio of particle to anti-particle with the mass and width constrained is $1.44 \pm .56$ which is still consistent with the ratio as determined by unconstrained fits.

TABLE 4.18
FIT RESULTS FOR PARTICLE AND ANTI-PARTICLE MASS DISTRIBUTIONS

Mode	Mass (MeV/c^2)	Sigma (MeV/c^2)	Yield	S/N	C.L.
$\Lambda\pi^+\pi^+\pi^-$	2283 ± 4	9 ± 3	30 ± 16	0.14	0.39
$\overline{\Lambda}\pi^-\pi^-\pi^+$	2285 ± 6	12 ± 5	31 ± 15	0.19	0.33
$pK^-\pi^+$	2279 ± 3	13 ± 3	73 ± 17	0.37	0.59
$\bar{p}K^+\pi^-$	2296 ± 4	16 ± 3	74 ± 18	0.48	0.28

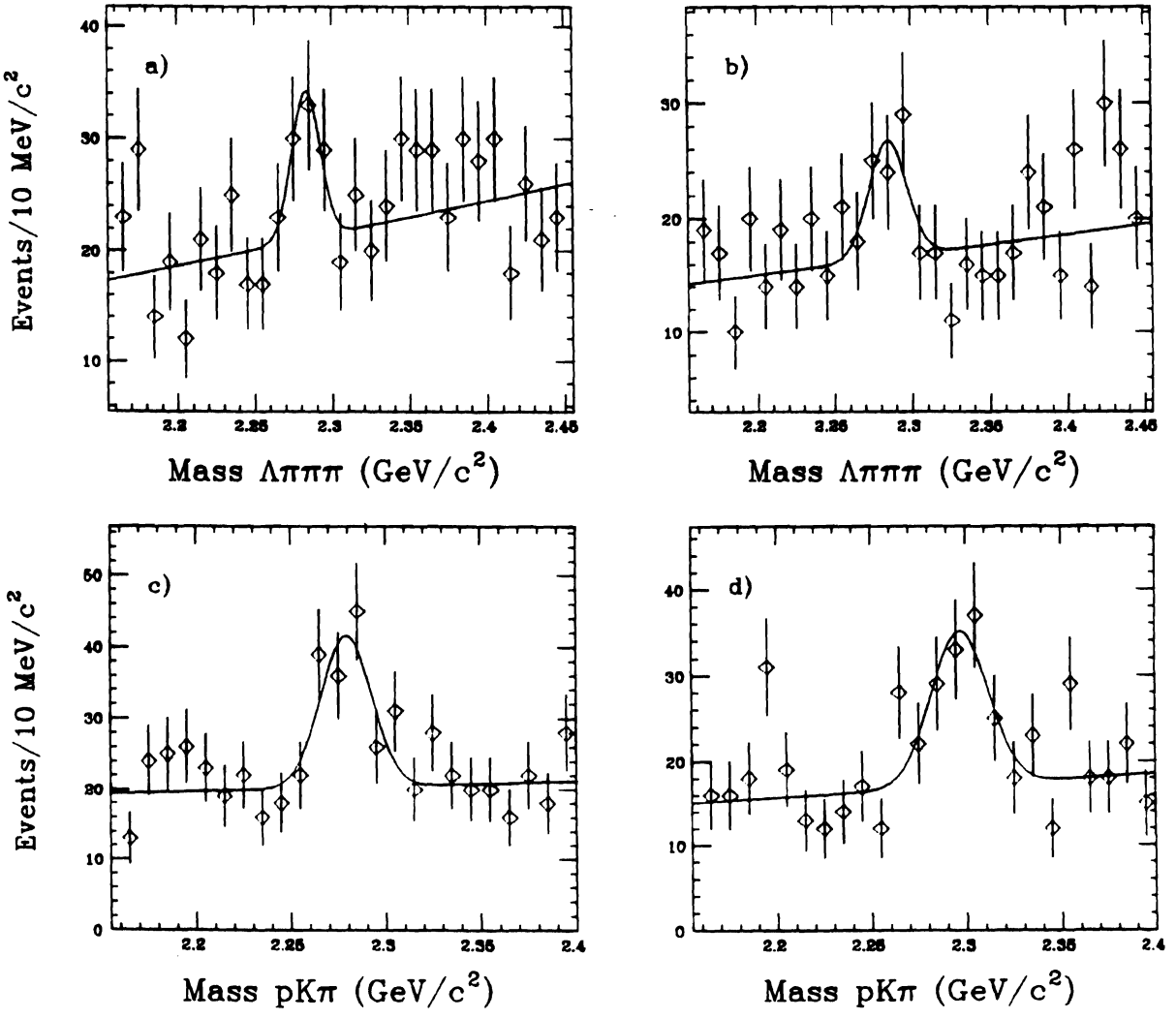

Figure 4.32: $\Lambda\pi^+\pi^+\pi^-$ and $pK^-\pi^+$ mass distributions shown separately for particles and anti-particles: a) $\Lambda\pi^+\pi^+\pi^-$, b) $\overline{\Lambda}\pi^-\pi^-\pi^+$, c) $pK^-\pi^+$, and d) $\bar{p}K^+\pi^-$

CHAPTER 5

CONCLUSIONS

The 1987-1988 data run of E-687 recorded a total of 60 million photon-nucleon interactions. Of these, 47 million were successfully reconstructed and determined to be hadronic in nature. Using this sample, the charm baryon Λ_c^+ was observed decaying into the $pK^-\pi^+$ and $\Lambda\pi^+\pi^+\pi^-$ channels. An analysis of these events was performed to measure the decay properties of the Λ_c^+.

5.1 Branching Ratio Summary

The $\Lambda\pi^+\pi^+\pi^-$ and $pK^-\pi^+$ samples were used to measure the relative branching ratio $BR(\Lambda_c^+ \rightarrow \Lambda\pi^+\pi^+\pi^-)/BR(\Lambda_c^+ \rightarrow pK^-\pi^+)$ using Λ_c^+ candidates with an energy in the range 60 $GeV \leq E(\Lambda_c^+) \leq 150$ GeV. Corrections for geometrical acceptance, and for reconstruction and analysis efficiencies were applied in an energy dependent manner to determine the yields for the two decay modes. After correction for $BR(\Lambda \rightarrow p\pi^-) = 0.641$, the relative branching ratio was found to be:

$$\frac{BR(\Lambda_c^+ \rightarrow \Lambda\pi^+\pi^+\pi^-)}{BR(\Lambda_c^+ \rightarrow pK^-\pi^+)} = 0.55 \pm 0.16 \pm 0.10$$

The $pK^-\pi^+$ sample was also analyzed to determine the relative branching fractions for the two 2-body resonance decays, $\Lambda_c^+ \rightarrow p\overline{K^{*0}}$ and $\Lambda_c^+ \rightarrow \Delta^{++}K^-$. Corrections for geometrical acceptance, and for reconstruction and analysis efficiencies were applied in a energy independent manner to determine the corrected yield for each of the decay modes. Using the corrected yields and $BR(\overline{K^{*0}} \rightarrow K^-\pi^+) = 0.66$, the relative branching fraction for the $p\overline{K^{*0}}$ mode was found to be:

$$\frac{BR(\Lambda_c^+ \rightarrow p\overline{K^{*0}})}{BR(\Lambda_c^+ \rightarrow pK^-\pi^+)} = 0.20 \pm 0.12 \pm 0.10$$

The relative branching fraction for the $\Delta^{++}K^-$ mode was found to be:

$$\frac{BR(\Lambda_c^+ \to \Delta^{++}K^-)}{BR(\Lambda_c^+ \to pK^-\pi^+)} = 0.24 \pm 0.12 \pm 0.10$$

5.1.1 Comparison with Other Experimental Results

In contrast to studies of charm mesons, results to date on Λ_c^+ branching ratio measurements are quite limited. Experimental measurements are limited to 6 experimental groups, including three e^+e^- colliding beam experiments, CLEO [42] running at CESR, ARGUS [43] running at DESY, and MARK2 [44] running at SLAC, a pp colliding beam experiment using the CERN ISR facility [45], and two fixed target experiments, the CERN NA32 [46] experiment using a 230 GeV/c pion beam on copper target, and the Fermilab E-691 [47] experiment using a photon beam with a mean energy of 145 GeV/c on a beryllium target. Results from these experiments are shown in Table 5.1. The results from this experiment agree with previous measurements within 1σ, although they tend to be consistently lower as shown in Table 5.1.

TABLE 5.1
MEASUREMENTS OF Λ_c^+ BRANCHING FRACTIONS RELATIVE TO THE $pK^-\pi^+$ DECAY MODE

Experiment	$\Lambda\pi^+\pi^+\pi^-$	pK^{*0}	$\Delta^{++}K^-$
CLEO	$0.65 \pm 0.11 \pm 0.12$	-	-
ARGUS	$0.61 \pm 0.16 \pm 0.04$	-	-
E-691	$0.82 \pm 0.29 \pm 0.27$	-	-
NA32	$0.94 \pm 0.41 \pm 0.13$	0.35 ± 0.11	-
ISR	-	0.28 ± 0.16	0.40 ± 0.17
MARK2	-	0.18 ± 0.10	0.17 ± 0.07
E-687	$0.55 \pm 0.16 \pm 0.15$	$0.20 \pm 0.12 \pm 0.10$	$0.24 \pm 0.12 \pm 0.10$

5.1.2 Comparison with Theory

As with the experimental measurements, theoretical predictions for the branching ratios of the charm baryons are also limited. Early theoretical efforts to predict the lifetime of the Λ_c^+ required a large contribution from the W-exchange diagram. These early predictions were

based on the large differences in the observed lifetimes for charm mesons and baryons. As experimental measurements of the charm particle lifetimes have improved, the need for this large contribution has diminished. The current measurements on the $p\overline{K^{*0}}$ and $\Delta^{++}K^-$ branching fractions support a small contribution from the W-exchange process.

5.2 Other Results

A search was made for the decays $\Lambda_c^+ \rightarrow \Lambda\pi^+$ and $\Lambda_c^+ \rightarrow \Lambda K^+K^-\pi^+$. No evidence for a signal was seen in either mode. The CLEO collaboration has recently measured the branching fraction $\Lambda_c^+ \rightarrow \Lambda\pi^+$ relative to the $\Lambda_c^+ \rightarrow pK^-\pi^+$ channel to be 0.17 ± 0.04 [42]. Based on the number of $\Lambda_c^+\pi^+\pi^+\pi^-$, a signal of 15 ± 7 events is expected for analysis cuts similar to the $\Lambda\pi^+\pi^+\pi^-$ analysis and assuming a similar efficiency for detecting the final state.

The $pK^-\pi^+$ and $\Lambda\pi^+\pi^+\pi^-$ samples for $E(\Lambda_c^+) \geq 60\ GeV$ were analyzed for asymmetric production of baryons with respect to anti-baryons. The ratio of particle to antiparticle was measured to be 0.97 ± 0.70 and 0.99 ± 0.33 for the $\Lambda\pi^+\pi^+\pi^-$ and $pK^-\pi^+$ modes respectively; this is quite consistent with symmetric charm baryon/antibaryon production for baryon energies greater than 60 GeV.

5.3 Prospects for the Future

Two fixed target experiments, E-687 and E-791, are currently running at FNAL with the goal of reconstructing over 100,000 charm decays each. The E-687 experiment has already recorded approximately 300 million events with additional time in the near future. This large data set with an improved spectrometer should provide a sample of several thousand Λ_c^+ candidates which will provide better measurements of the Λ_c^+ branching ratios. As experimental measurements improve and new decay channels of the Λ_c^+ are seen, it is hoped that theoretical intrest will be renewed in the area of charm baryon lifetimes and branching ratios.

APPENDIX A

MONTE CARLO

The Monte Carlo program used to measure the geometrical acceptances, reconstruction efficiencies, and analysis cut efficiencies was the E-687 Monte Carlo package ROGUE developed at the University of Illinois. The package consisted of two parts; the event generator GENERIC, and the detector simulation ROGUE. The output of ROGUE was a "faketape" Monte Carlo data tape that was identical in structure to real data tapes. This feature allowed the "faketape" to be processed by the same analysis routines that analyzed the data with no modifications to the routines. Several additional blocks containing detailed information about the generation of the event were appended to each event to allow for detailed studies.

A.1 GENERIC

Event generation was performed by GENERIC. This portion of the Monte Carlo program simulated the secondary electron beam interaction in the radiator, the resulting photon beam, the interaction of the photon bean in the experimental target, the production of charm particles, and the decay of unstable particles produced. The energy spectrum and beam profile for the initial electron beam was given by the experimentally measured spectrum of the beam taken during low intensity running of the Wide-Band electron beam [48] with magnets off. Simulation of the event started with the showering of the electrons in the radiator. The shower was produced according to a full bremsstrahlung spectrum that included a Bethe-Heitler knee. The produced photon(s) were then traced to the experimental target.

Interacting photons in the experimental target produced charm according to the photon-

gluon fusion cross-section given in Sec. 1.3. In addition, each of the photons was tested for pair conversion to account for attenuation of the photon beam. For events with multiple photons from multiple bremsstrahlung of the incident electron, only one of the photons was allowed to generate a charm-anticharm quark pair. The additional photons from multiple bremsstrahlung were allowed to produce electron-positron pairs in the target. The charm quark hadronization could either be specified at runtime or allowed to go to 20% charm baryon and 80% charm meson. The $P_\perp$ and x_f distributions for the charm particles were chosen according to the results from Fermilab experiment E691 [49]. In order to produce additional tracks from the primary vertex, the backward going quarks in the target nucleon produced jets according to the Feynman-Field fragmentation prescription.

The charmed hadrons were forced to decay according to the decay rates published by the Particle Data Group. Optionally, the decay chain could be either completely or partially specified. Unspecified portions of the decay chain were allowed to occur according to branching ratios given by the Particle Data group [39]. The produced particles generally decayed according to phase space; however, the appropriate matrix elements were used for semi-leptonic and resonance decays.

A.2 ROGUE

The simulation of the E-687 spectrometer was performed by ROGUE. Each particle generated by GENERIC was traced through the spectrometer until it decayed, failed to pass through an aperture, or exited the spectrometer. The charged particles were traced though the magnetic fields of the analysis magnets using a TURTLE tracing procedure. At specified points, the deflection of the particle was determined from the momentum of the particle and the strength of the magnetic field that it experienced at that location. As the particle passed through the different detectors, the detector response to the particle was simulated. For the Microstrip system, the amount of charge deposited in a strip was given by a Landau distribution which was determine by a fit to data. Charge sharing between strips was determined by the location of the hit and a simple geometrical model [31]. Noise was simulated by adding spurious hits consistent with a Gaussian noise distribution to the final list of hits to be digitized. For the PWC system the wire number of the hit was determined

and recorded. Adjacencies were added based on the measured adjacency rate for the given plane, which was typically 4 – 6%. Finally, hits were removed from the list of PWC hits in order to simulate the measured efficiency of the chamber system, typically 80 – 90%. As charged tracks were traced through the Čerenkov counters, they were checked for the emission of Čerenkov photons, which were traced to the photomultiplier tubes. The OH and H×V counters were simulated with efficiencies determined from experimental measurements of the counter efficiencies. The trigger counters, TR1 and TR2, were simulated assuming 100% efficiency for the counters. Muon counters and calorimetry were not simulated in ROGUE.

The Master Gate trigger was simulated requiring hits in both of the trigger counters, TR1 and TR2, and satisfaction of the 2-body requirement using the H×V and OH counters. The second level trigger buslines used to form the second level energy trigger were also simulated in ROGUE. Recoil electrons were traced through the sweeper magnets using a sudden-bend approximation, the RESH counter response was simulated, and the buslines were set if the energy deposition in the RESH counter satisfied the RESH trigger requirements. The HC energy response was simulated by summing the energies of all of the hadrons striking the front of the HC (excluding the central opening). The hadronic energy busline was set if the total hadronic energy was above the energy threshold, typically 35 GeV. The efficiency as a function of energy for satisfying the hadronic energy busline was determined from experimental measurements. The chamber multiplicity busline was set if there was at least one hit in P0X outside of the central pair region after removal of chamber hits due to chamber inefficiencies. The second level energy trigger requirement was satisfied if the Master Gate, RESH busline, HC energy busline, and chamber multiplicity busline requirements were all satisfied.

In order to account for changes during the run in chamber efficiencies, energy trigger thresholds and efficiencies, target configurations, and targeting efficiencies, the run was divided into 8 run periods, ranging in length of 2 days to 2 weeks. Efficiencies and target configurations were determined for each of these periods. ROGUE allowed the selection of one or more of these periods. For cases where more then one run period was simulated the number of events for each period was based on the relative luminosity for the running periods. In this manner, a complete simulation of the data run could be done, properly in

terms of changes in luminosity and running conditions.

BIBLIOGRAPHY

[1] M. Gell-Mann, Phys. Lett. **8**, 214 (1964).

[2] D.J. Gross and F. Wilczek, Phys. Rev. Lett. **30**, 1343 (1973).

[3] S.L. Glashow, J. Iliopoulos, and L. Maiani, Phys. Rev. **D2**, 1285 (1970).

[4] J.E. Augustin, et al., Phys. Rev. Lett. **33**, 1406 (1974).

[5] J.J. Aubert, et al., Phys. Rev. Lett. **33**, 1404 (1974).

[6] S.W. Herb, et al., Phys. Rev. Lett. **39**, 252 (1977).

[7] W.R. Innes, et al. Phys. Rev. Lett. **39**, 1240 (1977).

[8] J.J. Sakurai, "Advanced Quantum Mechanics", Addison-Wesley Publishing Co, 1982.

[9] S. Weinberg, Rev. Mod. Phys. **46**, 255 (1974).

[10] M. Banner, et al., Phys. Lett. **122B**, 476 (1983).

[11] Bagnaia, et al., Phys. Lett. **129B**, 130 (1983).

[12] N. Cabibbo, Phys. Rev. Lett. **10**, 531 (1963).

[13] M. Kobayashi and T. Maskawa, Prog. Theor. Phys. **49**, 652 (1973).

[14] R.J. Morrison and M.S. Witherell, "D-Mesons" preprint USCB-HEP-89-01 (1989).

[15] R. Rückl, Habilitationsschrift submitted to the University of Munich (1983).

[16] V. Barger, J.P. Leveille, and P.M. Stevenson, Phys. Rev. Lett. **44**, 226 (1980).

[17] T. Okazaki, Phys. Rev. **D30**, 677 (1984).

[18] H. Cheng, Z. Phys. **C29**, 127 (1985).

[19] B. Guberina, R. Rückl, and J. Trampetic, Z. Phys. **C33**, 297 (1986).

[20] V. Gupta and K.V.L. Sarma, Int. Jour. of Mod. Phys. **A5**, 879 (1990).

[21] L.M. Jones and H.W. Wyld, Phys. Rev. **D17**, 759 (1977).

[22] J. Butler, "High Energy Photoproduction", Particles and Fields Proceedings, 3rd Mexican School, Cuernavace, Mexico, 1988.

[23] R.K. Ellis and P. Nason, Nucl. Phys. **B312**, 551 (1989).

[24] J. Butler et al., "Design for a New Wide-Band Neutral Beam for the Tevatron." FERMILAB Note TM-963, 1980.

[25] P.L. Frabetti, et al., "Description and Performance of the Fermilab E687 Spectrometer" FERMILAB-PUB-90-258-E, 1990. Submitted To *Nucl. Instr. and Meth.*

[26] L. Moroni and D. Pedrini, "All You Always Wanted To Know About Microrico But Were Afraid To Ask" E687 internal note, 1988.

[27] J. Cumalat, "A Study of the Microstrip System and Algorithm." E687 internal memo, 1988.

[28] J.R. Wilson, "Early Charm Results from E687" Proceedings of the APS Division of Particles and Fields General Meeting, January 1990.

[29] S. Culy, "LINKARB" E687 internal memo, 1988.

[30] J.E. Wiss, "Calculations Related to Fitting and Linking" E687 internal Memo, 1988.

[31] M. Giammarchi, et al., Nucl. Instr. and Meth. **A251**, 40 (1986).

[32] J.E. Wiss and R. Culbertson, "DVERT" E687 internal memo, 1989.

[33] J.R. Wilson and J.E. Wiss, "Generalized Vee Fitting" E687 internal memo, 1989.

[34] C.W. Bogart, "DownV - Reconstruction Vee Analysis Program" E687 internal memo, 1988.

[35] J.E. Wiss, et al., "Cerenkov Group Report" E687 internal memo, 1988.

[36] S. Park, Ph.D. thesis, Northwestern University, 1990 (unpublished).

[37] S. Bianco, et al., " Energy Calibration and Electron Identification in the OE and IE_{pf}" E687 internal memo, 1989.

[38] S. Bianco, et al., " Charge Particles Energy Deposition in IE_{pf}" E687 internal memo, 1988.

[39] Particle Data Group, "Review of Particle Properties" Phys. Lett. **B239** (1990).

[40] G.R. Jaross, Ph.D. thesis, University of Illinois, 1990 (unpublished).

[41] G.R Jaross, "Preliminary $K\pi\pi\pi/K\pi$ Branching Ratio" E687 internal memo, 1990.

[42] P. Avery, et al., "Inclusive Production of the Charmed Baryon Λ_c from e^+e^- Annihilations at $\sqrt{s} = 10.55$ GeV" preprint CLNS 90/992 (1990).

[43] H. Albrecht, et al., Phys. Lett. **B207**, 109 (1988).

[44] J. Weis, "Proceedings of the IVth International Conference on Baryon Resonances, University of Toronto, 14-16 July, 1980", N. Isgur ed., p512.

[45] M. Basile, et al., Nuovo Cimento **62A**, 14 (1981).

[46] S. Barlag, et al., Z. Phys. **C48**, 29 (1990).

[47] J.C. Anjos, et al., Phys. Rev. **D41**, 801 (1990).

[48] K.L. Lingel and J.E. Wiss, "Improvements to CHAT/GENERIC/ROGUE For the Purpose of Measuring Cross Sections" E687 internal memo, 1989.

[49] K.L. Lingel, Ph.D. thesis, University of Illinios, 1990 (unpublished).